Aerodynamic loads and flow structures on a simultaneously rotating and pitching flat plate

by

Muhammad Shahan Qamar

A thesis submitted to the Graduate Faculty of
Auburn University
in partial fulfillment of the
requirements for the Degree of
Master of Science

Auburn, Alabama
December 9, 2023

Keywords: separated flows, vortex flows, wakes/jets

Approved by

Vrishank Raghav, Chair, Associate Professor, Ginn Faculty Achievement Fellow of Aerospace
Engineering
Brian Thurow, Department Chair, W. Allen and Martha Reed Professor of Aerospace
Engineering
Anwar Ahmed, Professor of Aerospace Engineering

Abstract

Unsteady flow separation and leading-edge vortices (LEV) profoundly impact the aero-dynamics of insect wings, helicopter rotor blades, and similar systems. The dynamics of such systems depend on wing pitch rate and pivot location. This study employs direct force measurement and particle image velocimetry to analyze a rotating and pitching flat plate that pitches from $0°$ to $90°$. The effects of changing reduced pitch rates ($K = 0.02$, 0.03, 0.05, 0.075, 0.1, 0.2), five non-dimensional pitch pivot locations ($x_p/c = 0$, 0.25, 0.50, 0.75, 1) and two Reynolds numbers ($Re = 5,000$ and $10,000$) on the aerodynamic lift (C_L), drag (C_D) and moment (C_M) coefficients, as well as on the LEV system are investigated. The results show that the combined effect of K and x_p/c governs the resultant aerodynamic response of the rotating and pitching flat plate. Increasing K at $x_p/c = 0$ results in highest $C_{L_{max}}$, $C_{D_{max}}$ and $C_{M_{max}}$ across all cases. The increase in the respective coefficients starts to decrease for the aft pivot locations and eventually becomes nonexistent at $x_p/c = 1$. A higher K results in a delayed pitch angle for LEV formation and an increase in LEV strength. Moving x_p/c towards the trailing edge also delays the pitch angle for LEV formation, but results in a decrease in LEV strength. Based on the induced camber effect of pitching motion, the study introduces a new trailing edge velocity-based scaling analysis that found to collapse the C_L and C_D trends for all K and x_p/c cases. Furthermore, the study discusses a noteworthy phenomenon – the dynamic convective time shift. Across various x_p/c values, a successful temporal shift leads to the convergence of time histories of C_L and C_D evolution at a same non-dimensional effective convective time (t^*_{eff}). Lastly, changing Reynolds number from $Re = 5,000$ to $10,000$ reveals a noticeable decrease in C_L and C_D, which is accompanied by a lower vorticity growth rate at $Re = 10,000$.

Acknowledgments

Table of Contents

List of Figures

List of Tables

Chapter 1

Introduction

1.1 Motivation

The evolution of flapping wing flight over 150 million years has fascinated people for centuries. In recent decades, scientists have been exploring insects and birds like hummingbirds, dragonflies, bees, and fruit flies [1, 2, 3, 4, 5, 6], adding a contemporary touch to this age-old narrative. The flight of biological insects inspires the designs of micro air vehicles (MAVs) that make use of a combination of rotating, pitching, or plunging motions to enhance its aerodynamic performance. Various vehicle design concepts such as rotary wing, fixed wing, and flapping wing have been proposed for MAVs [7, 8, 9, 10, 11, 12, 13]. For small wings, fixed wing vehicles face the fundamental limits of flight control and lift generation and flapping wings provide rapid maneuvers, high lift, and thrust at a small scale [14]. Flapping wing flight has been extensively studied and several reviews have been provided by Sane [15], Lehmann and Dickinson [16], and Shyy et al.[17]. The single most important aerodynamic phenomenon that is largely responsible for the success of flapping flight at low Reynolds numbers has been shown to be the leading edge vortex (LEV) [18, 19]. Figure 1.1 shows the kinematics and prominent features in insect flight. Research is still ongoing to unfold the exact intricacies involved in flapping flight due to the mechanical and aerodynamic complexities [20] involved in nature's optimized locomotive.

The development of LEVs can also be observed in various other disciplines as well. For example, large scale vortical structures are produced during time-dependent large amplitude pitching motion of helicopters due to unsteady flow separation, which are associated with the phenomenon of dynamic stall [21]. The reports of Ekaterinaris and Platzer [22] confirmed
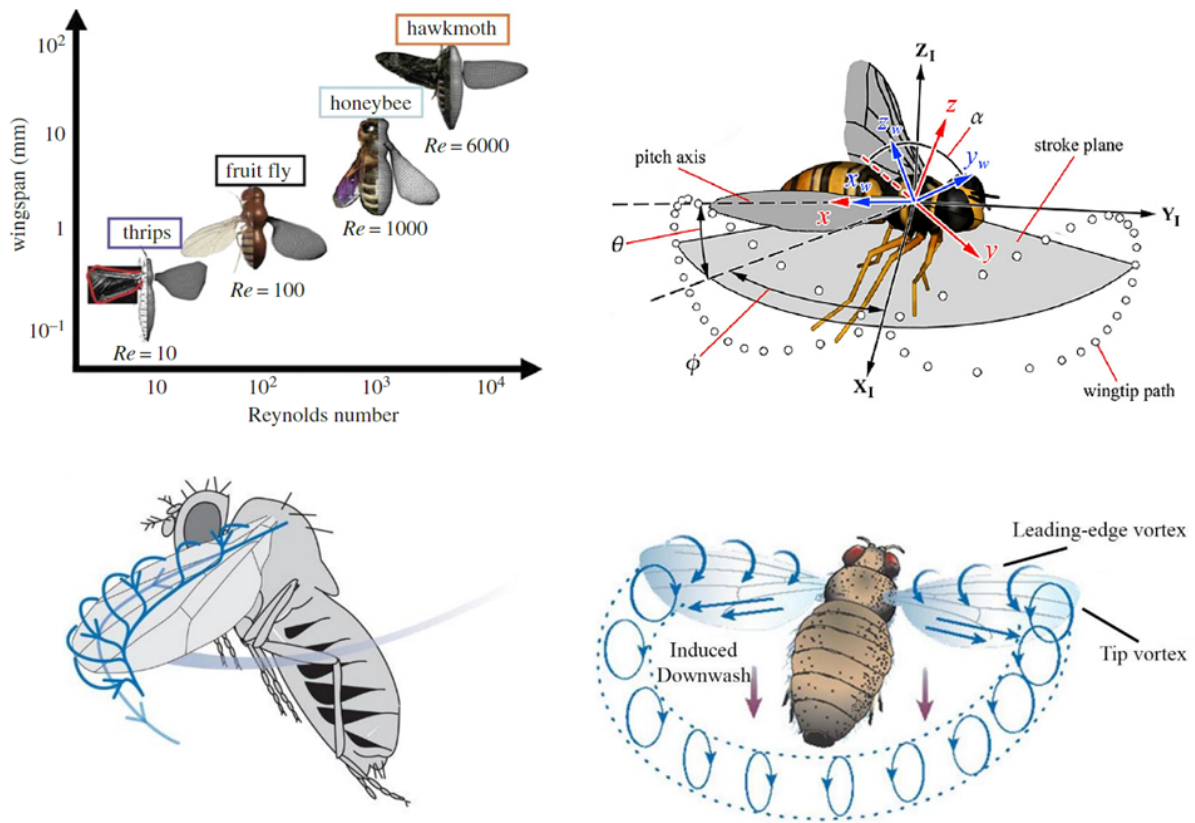
Figure 1.1: Kinematics and prominent features in insect flight (Adapted from Hao et al. 2016)

that the dynamic stall phenomenon was initially observed in turbines and rotating wing applications. Such unsteady maneuvers generate distinct flow structures and aerodynamic loads which have been a specific area of interest in the recent past. Researchers are keenly interested in understanding and mitigating dynamic stall as it can affect the stability and control of helicopters. Dynamic stall process is influenced by various parameters like the free stream conditions, geometric parameters of the airfoils and pitch rate. Additionally, the pivot location is also a parameter worth considering, which plays an important role in the unsteady response of the pitching airfoil as it affects the generation and evolution of important flow structures in pitching motion such as LEV and wake vortex [23]. Nowadays, researchers adopt a decomposition strategy to simplify the complex kinematics of flapping wing and helicopter flight into basic canonical motions of translation, rotation, and pitch. This approach enables a systematic

investigation of motion combinations, facilitating the understanding of LEV physics and laying the groundwork for future studies involving complex wing kinematics.

1.2 Background

1.2.1 Studies on translating and pitching wing

In the field of fluid dynamics, the pitch rate is normally defined in terms of non-dimensional reduced pitch rate (K), which is the ratio of the pitching velocity to the translational velocity. It is mathematically represented as $K = \dot{\alpha}c/2U_\infty$. Figure 1.2 shows the schematic representation of reduced pitch rate in terms of pitching speed $\dot{\alpha}$ and translational velocity U_∞. In case of translating and pitching flat plates or airfoils, a lot of research has been conducted for investigating the aerodynamic forces and flow structures. For example, Granlund et al. [24] did experiments on translating pitching flat plates. They performed direct force measurements by changing pitch rates and pivot locations and concluded that higher pitch rates give rise to higher aerodynamic forces. Yu and Bernal [23] conducted experiments on a finite wing in which they varied the reduced pitch rates (K). They noted that the increase in the coefficient of lift (C_L) was directly proportional to values of K greater than 0.065. Recently, Yu et al. [25] conducted a comprehensive investigation of unsteady lift, drag, and moment coefficients for a thin pitching airfoil. Their results indicated that for reduced pitch rates lower than 0.03, the unsteady aerodynamics is limited to a stall delay effect. For higher pitch rates, the unsteady response is dominated by a buildup of the circulation, which increases with the pitch rate and ultimately results in higher aerodynamic forces. They also proposed a Wagner function based new time-dependent model to capture the trends of normal force and moment coefficients. The numerical investigation performed by Visbal et al. [26] for unsteady laminar flow past a pitching NACA 0015 airfoil focused mostly on the development of flow structures. They concluded that, for a given pitch axis location, increasing the pitch rate caused the dynamic stall vortex to form at a higher incidence. Pradeep et al. [27] did an investigation on cycle to cycle variations of pitching cycle for NACA 0012 airfoil using immersed boundary framework. At low frequencies, they observed that the pitching cycles evolved in distinct patterns whereas for higher

pitching frequencies, LEVs from different cycles merged and evolved to form a vortex cluster which significantly altered the aerodynamic forces. All these studies show that higher pitch rates result in increased aerodynamic forces, displaying a linear relationship with the lift coefficient. The pitch rate influences unsteady aerodynamics, circulation buildup, dynamic stall vortex formation, and leading-edge vortex merging, leading to notable changes in aerodynamic forces.
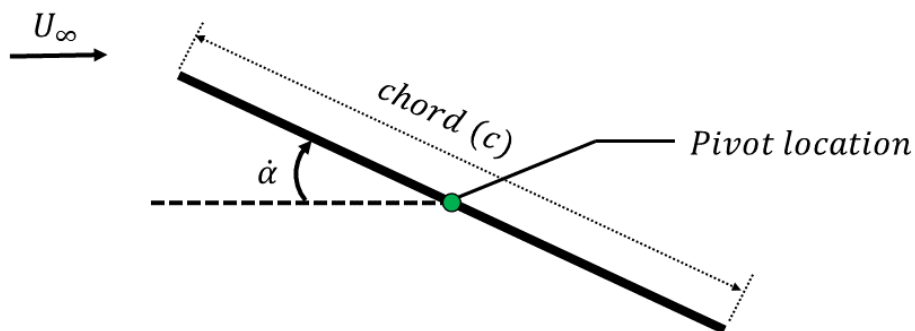
Figure 1.2: Schematic representation of reduced pitch rate (K)

The pitch pivot location also plays an important role in the unsteady response of the pitching airfoils and this parameter is mostly investigated along with the reduced pitch rate. In literature, pivot location is defined in terms of non-dimensional pitch pivot location (x_p/c) as the ratio of the distance of the pivot axis from the leading-edge to the chord length (c). If the pivot location is at the leading edge, then $x_p/c = 0$ and if we start moving towards the trailing edge, we can define other pivot locations in terms of their location along the chord. Figure 1.3 shows the schematic representation of non-dimensional pitch pivot locations at different locations along the chord. Most researchers related the influence of pivot location on the aerodynamic forces by co-relating with the development of aerodynamic flow structures. Experiments by Yu and Bernal [23] concluded that the effect of the pivot location caused a delay of time due to free stream convection from the leading edge to the pivot location and thus the force data for the pivot location other than the leading edge (LE) could be shifted by the time delay. Various other researchers [26, 25, 26, 27] also made similar observations that pitch pivot location affected the LEV evolution and caused a delay in the evolution of the lift and

4

drag forces. They established that the impact of LEV was found to increase with the absolute distance between the pivot axis and the 3/4-chord location. Therefore, for a given pitch rate, the downstream displacement of the pivot axis resulted in a delay in the formation of the dynamic stall vortex and in a reduction in the aerodynamic forces of the airfoil. Li et al. [28] found that the leading-edge vortex grows earlier and the lift coefficient increases with the forward movement of the pivot location during the upstroke motion, which shows an opposite trend during the downstroke motion. Such a trend stems from the phase lag in the flow evolution for different cases. They concluded that the effective angle of attack is the dominant factor of pivot effect for most time of a period. Therefore, we can say that the pitch pivot location in pitching airfoils significantly impacts unsteady response, aerodynamic forces, and leading-edge vortex evolution, emphasizing the need for optimization to enhance aerodynamic performance and efficiency of pitching wings.
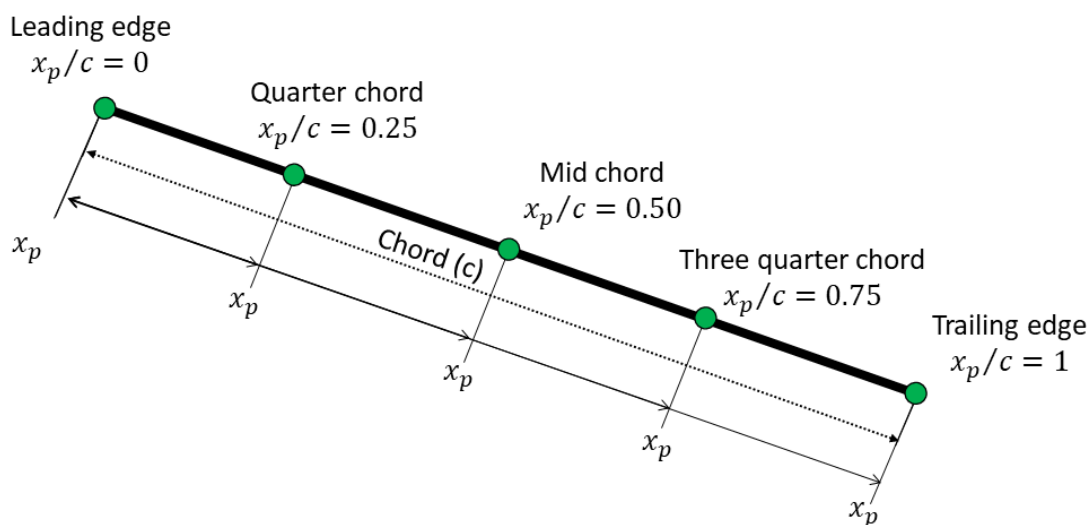
Figure 1.3: Schematic representation of non-dimensional pitch pivot location (x_p/c)

Reynolds number also affects the flow evolution and resulting aerodynamics forces on a pitching airfoil. It is the ratio of the inertial forces to the viscous forces in the flow field. The impact of varying Reynolds number on the leading edge vortex dynamics of pitching flat plate was investigated by Widmann and Tropea [29] . It was found that Reynolds number was responsible for the transition of leading-edge vortex separation from the feeding shear layer on the airfoil surface. Ramesh et al. [30] introduced a leading edge suction parameter (LESP)

5

to predict the initiation of LEV on the surface of wing. They postulated that LEV formation initiates at a critical value of LESP for a given airfoil shape and Reynolds numbers. Therefore, for a given Reynold number, the critical value of LESP may be calibrated and it can be used to predict the LEV formation for various other motion kinematics. Various other researchers [31, 32, 33, 34, 35, 36, 37, 38, 34] have explored the influence of Reynolds number on force generation and leading-edge vortex (LEV) development. For example, Garmann and Visbal [34] studied the effect of Reynolds number (Re = 5,000 − 40,000) on a flat plate and showed that the aerodynamic loading and flow structure exhibited relative insensitivity to changes in Reynolds number. Most of the studies [31, 32, 39, 37, 38, 34] have shown insensitivity to changing Reynolds number. In contrast, some other investigations [33, 35, 36] showed that increasing Reynolds number led to higher aerodynamic loads and noticeable changes in flow structures. To conclude, Reynolds number is an important parameter which influences leading-edge vortex initiation and separation and may or may not influence the aerodynamic loading on the surface of wing.

1.2.2 Studies on rotating and pitching wing

The combined pitch up and rotation maneuver yields more resemblance to the perching motion of a bird [40, 41, 42, 38] and is more applicable to the rotorcraft and turbine aerodynamics [21, 22]. The combination of rotation and pitch remains relatively underexplored in the literature, with limited studies dedicated to investigating the flow characteristics and aerodynamic forces. Percin and Oudheusden [43] compared two motion kinematics: pitching while revolving and surging with a fixed angle of attack. They found that the pitching wing generated higher forces during the buildup phase due to increased magnitude and growth rate of the leading-edge vortex (LEV) circulation, favorable LEV position and trajectory, and generation of bound circulation. In contrast, the revolving-surging wing had negligible force generation during the acceleration phase. Ozen and Rockwell [44] compared the flow structure on the rotating plate and the equivalent of a purely translating plate and revealed that the vorticity level in the distributed layer from the leading-edge of translating plate is significantly lower than the vorticity magnitude of the concentration formed at the leading-edge of the rotating plate. Bross and

Rockwell [45] discussed the presence of distinctive vortical structures for revolving pitching wings in comparison with translating–pitching and pure revolving wing cases. They showed that the vortex system involving the LEV and the TV preserves its coherence in the case of the revolving–pitching wing, while it is degraded in the case of a pure revolving wing. It is also revealed that compared to the translating–pitching wing case, in which the LEV moves away from the leading-edge region relatively quickly, a more stable vortex structure is present in the revolving–pitching motion. Manar et al. [46] analyzed forces and leading edge vortex characteristics on a flat plate for different wing kinematics. Based on integrated leading edge normal velocity, a novel time scale was introduced which effectively captured the trends for pitching and surging cases. Furthermore, the rotational motion demonstrated extended leading edge vortex stabilization as compared to translating cases. Based on these previous studies, it can be said that the combined pitch and rotational maneuver generates higher forces in the buildup phase through increased circulation and favorable LEV trajectory. It also exhibits a more stable vortex structure and enhanced LEV circulation compared to pure revolving or translating-pitching motions. However, the scope of these studies was limited to only one aspect of flow field and was inconsistent in establishing a broader relationship between the effect of reduced pitch rate, pitch pivot location and Reynolds number on the flow field and aerodynamic loads of simultaneously pitching and rotation maneuvers.

1.2.3   Quasi-steady estimation of aerodynamic forces

A quasi-steady model [47] can also be used to estimate the evolution of unsteady forces for the given kinematics. In this model, the instantaneous force F_i is composed of three main contributions:

$$F_i = F_{revolution} + F_{inertial} + F_{pitching} \tag{1.1}$$

Here, $F_{revolution}$ is the force component as a result of the circulatory force due to rotational motion of the wing. The circulatory force includes the bound circulation at a constant pitch angle and an additional component due to LEV circulation which would differ for different

pitch rates and pitch pivot locations. $F_{inertial}$ is the force due to inertia of the added mass of the fluid acting normal to the wing surface. As the body accelerates or decelerates, it induces a change in the fluid flow around it. The fluid in turn exerts an equal and opposite force on the body that manifests itself in terms of $F_{inertial}$. Lastly, $F_{pitching}$ is the force due to pitch up motion of the wing. The pitching motion results in varying local velocities in the chord wise direction which in turn generates a varying effective angle of attack distribution along the chord. For leading-edge (LE) pivot, the wing motion creates an upwash along the chord just downstream the leading edge. This upwash produces an upward induced angle of attack and the wing sees a higher α_{eff} than α_{geo}. Higher α_{eff} leads to increased fluid momentum being exerted on the pressure side of the plate, resulting in a net upward force and consequently generating additional lift for the leading edge pivot case. The magnitude of upwash is also dependent on the pitch rate ($v_{upwash} = r\dot{\alpha}$). A higher reduced pitch rate would result in a higher upwash and greater α_{eff}, subsequently, resulting in higher lift force. For mid-chord (MC) pivot, it creates both an upwash and downwash on either side of the pivot location and they cancel out each other. Therefore, we don't expect a significant contribution of $F_{pitching}$ for mid chord pivot location. For trailing-edge (TE) pivot, the pitching motion is inducing a downwash along the chord that reduces α_{eff}. Therefore, $F_{pitching}$ contributes negatively towards lift for TE pivot location and the magnitude of downwash also increases with K. The combined effect of $F_i = F_{revolution} + F_{inertial} + F_{pitching}$ gives the resultant aerodynamic force on the surface of wing.

1.3   Scope of current investigation

In reviewing prior research, most of the studies were focused on the translating and pitching wing cases. The prevailing literature often confined its investigations to isolated aspects of pitching motion, where the investigations primarily involved the systematic variation of a single parameter. The resultant conclusions, although valuable, tended to provide generalized insights into the impact of individual parameters on the flow field and aerodynamic loads. However, in practical applications, the relevance of rotation and pitch maneuvers becomes more significant, particularly in contexts of insect wings, helicopter rotor blades, and turbines. Therefore, there is

a gap in the previous literature as only a limited number of studies have focused on the rotating and pitching wings due to the challenges associated with the experimental setup and simulations. Furthermore, the interdependency relation of various parameters is yet to be explored. For example, what would happen if we investigate the effect of changing reduced pitch rate at different pivot locations or at different Reynolds numbers and then make conclusions based on those results.

This investigation aims to fill the gap in the previous literature by providing direct insight into aerodynamic phenomena, flow structures, and the resultant loads on a simultaneously rotating and pitching flat plate. The study employs aerodynamic loads measurement and particle image velocimetry (PIV) technique in a rotating frame of reference which enables us to capture instantaneous time resolved flow field information. It systematically investigates the effects of the reduced pitch rates ($K = 0.02, 0.03, 0.05, 0.075, 0.1, 0.2$), five non-dimensional pitch pivot locations ($x_p/c = 0, 0.25, 0.50, 0.75, 1$) and two Reynolds numbers ($Re = 5,000$ and $10,000$) on the aerodynamic lift (C_L), drag (C_D) and moment (C_M) coefficients, as well as on the LEV system. Furthermore, based on the induced camber effect of pitching motion, the study discusses a scaling analysis which successfully collapses the C_L and C_D force data for all K and x_p/c cases considered. Lastly, in contrast to the previous studies on pitch pivot location based convective time scaling, a dynamic convective time shift analysis has been discussed. This approach is based on the induced flow at the leading edge of the plate and has been found to offer a better collapse of C_L and C_D trends for all pitch pivot locations at the same non-dimensional convective time.

Chapter 2

Methodology

2.1   Experimental setup

The experiments were performed using a hydrodynamic hover rotor facility with the wing ro-
tated at a constant angular velocity. The facility comprised of a $1.2\ m$ x $1.2\ m$ x $1.2\ m$ acrylic
tank, as shown in figure 2.1. The arrangement was constructed such that the rotation motor
was positioned on a three-tier bearing mount assembly above the tank, while the camera was
mounted co-axially below the tank independently. The rotation motor, a NEMA 34 stepper
motor, was linked to the rotation shaft by belt and timing pulleys. The three-tier bearing mount
assembly was intended to decrease vibrations and maintain the straightness of the rotation shaft
by having multiple points of contact between the frame and the shaft. A mirror holder assem-
bly, specifically designed to secure a mirror, was attached at the opposite end of the shaft. The
mirror holder assembly also housed a servo motor to control the pitch motion and a load cell to
measure aerodynamic loads. Such an arrangement eliminated any fluid dynamic interference
resulting from the load cell and servo motor. For the study, a $0.12\ m$ x $0.09\ m$ elliptical glass
first surface mirror with $\lambda/4$ flatness was attached to the mirror holder assembly at $45°$ incli-
nation to observe the flow field in the rotating frame of reference (FoR). Imaging of the flow
field was captured using a high-speed camera mounted beneath the tank. More details of the
experimental setup can be found in [48].

The wing model was pitched about different pitch pivot locations by a waterproof servo
motor that was placed inside the mirror holder assembly. The servo motor had an operating
voltage range of $8.4 - 12.6\ volts$ and was capable of no load pitching speeds of $13\ rad/s$
and the maximum torque range was $3.24 - 4.9\ Nm$. A gear mechanism was meticulously
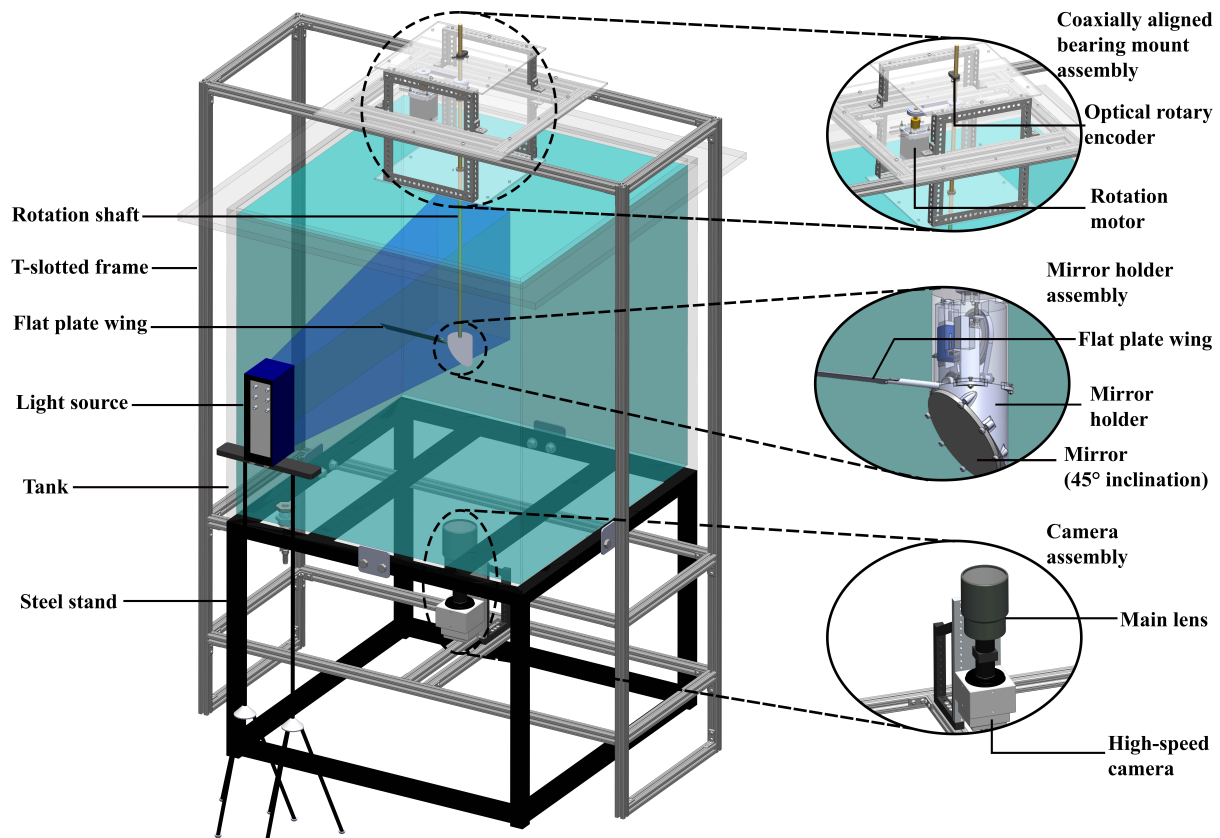
Figure 2.1: CAD representation of the hydrodynamic hover rotor facility

designed to connect the servo motor to the flat plate. In this configuration, the smaller gear was affixed to a hollow shaft, which also housed the load cell. The load cell was further connected to the flat plate via a connecting rod. To ensure a precise and coaxial pitching motion while preventing lateral displacement or sagging issues, two bearings with distinct spacing were used to secure the hollow shaft. This entire assembly was firmly housed within a precisely machined aluminum block. This block, in turn, was connected to the mirror holder assembly through mounting brackets and screws. Figure 2.2 provides a visual representation of the complete setup within the mirror holder assembly.

2.1.1 Wing geometry and experimental test matrix

A rectangular flat plate with a chord $c = 0.0254\ m$ and span $s = 6c$ was used for experiments. Using a rectangular wing offered benefits of simpler wing geometry, comparison with theoretical models, and control over specific parameters of interest. The wing model was positioned
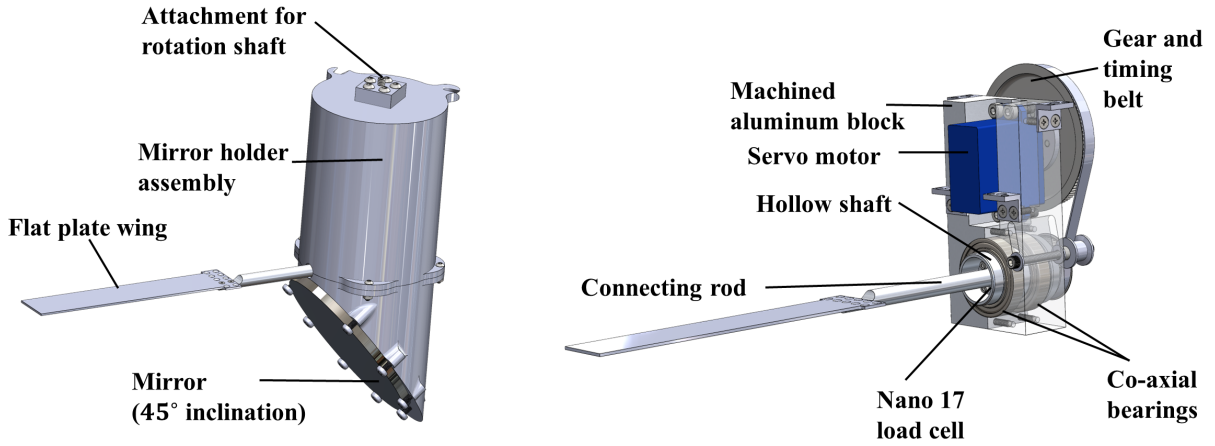
Figure 2.2: CAD representation of the pitching mechanism

approximately $5c$ distance from the water surface, $7c$ distance from the bottom wall, and $5c$ (wing tip to wall) distance from the side wall to eliminate any wall or free-surface interference effects [49]. The distance between the root chord and the rotation axis was $0.102\ m$, and the radius of gyration was at a distance of $0.082\ m$ from the root, resulting in a Rossby number of 7.2, which is the ratio of inertial forces to the coriolis effects. The distance from the center of rotation to the tip of the wing model was taken as the reference position for defining the tip velocity ($U_{tip} = \Omega R$), where Ω is the rotational speed in rad/s and R is the distance from the centre of rotation to the wing tip. Time was non-dimensionalized and measured in units of convective time (t^*) such the $t^* = tU_{tip}/c$. The Reynolds number for these experiments was defined based on the tip velocity of the wing, $Re_{tip} = \Omega Rc/\nu$. To investigate the influence of Reyonlds number (Re), the rotational speed Ω was increased to achieve Re of 5,000 and 10,000. In defining the Reynolds number, the choice of tip velocity as the reference was made somewhat arbitrarily. This choice was not driven by a specific focus on tip effects but rather by a pragmatic consideration of experimental convenience and adherence to established conventions in the field. The reduced pitch rate K was defined as the ratio of pitch velocity to rotational velocity. In these experiments, rotational velocity was based on the wing tip velocity and the expression for K was given as $K = \dot{\alpha}c/2U_{tip}$ where $\dot{\alpha}$ is the pitch rate in rad/s. The reduced pitch rates considered for these experiments were $K = 0.02, 0.03, 0.05, 0.075, 0.1$
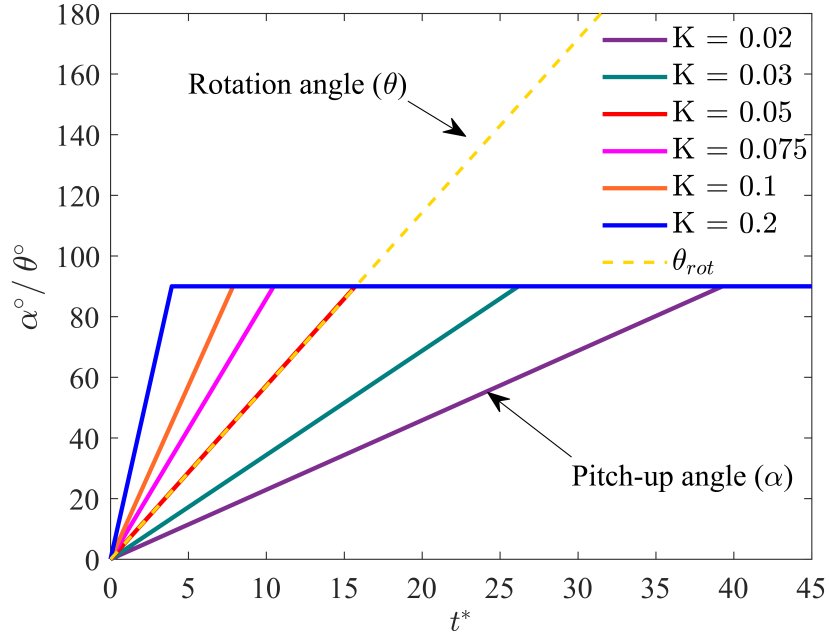
Figure 2.3: Comparison of rotation and pitching speed for different reduced pitch rates K

and 0.2. Furthermore, five non-dimensional pitch pivot locations ($x_p/c = 0$, 0.25, 0.5, 0.75, 1) were defined as the ratio of the distance of the pivot location from the leading edge and the chord length; where $x_p/c = 0$ represents the leading edge and $x_p/c = 1$ represents the trailing edge pivot location. The wing was pitched from $\alpha = 0°$ to $\alpha = 90°$. The complete experimental test matrix has been given in table 2.1 resulting into 60 test cases in total. Furthermore, the comparison of different reduced pitch rates (K) with the rotation speed (Ω) have been shown in figure 2.3 where the dotted line represents the wing rotation speed.

Re_{tip}	x_p/c	K
		0.02
	0	
		0.03
	0.25	
5,000		0.05
	0.50	
10,000		0.075
	0.75	
		0.1
	1	
		0.2

Table 2.1: Experimental test matrix

2.1.2 Motion control of servo motor

The motion profile of servo motor for pitch control was programmed with a custom built Lab-VIEW code. The pitch motion of the plate was tracked by images captured by a high speed image acquisition camera to compare the commanded and measured kinematics. Investigations involving the unsteady aerodynamic response of an airfoil during pitch ramp motion usually involve an airfoil pitching from a low to high pitch angles. Ideally, the pitch motion should have a constant velocity throughout the pitching cycle. However, practical experiments face limitations due to the finite acceleration and deceleration imposed by the driving system. The impact of smoothing out the pitch ramp motion has been studied before by various researchers [50, 24, 51]. It has been concluded that the dynamics of the unsteady stall process remains relatively unaffected by the acceleration and deceleration profile. The initial acceleration briefly affects the aerodynamic loads and pressure distribution during acceleration, after which these depend primarily on the pitch angle for a given pitch rate. This allows us to select convenient acceleration profiles for experiments and simulations without significantly impacting unsteady stall dynamics. For the present investigation, the hyperbolic-cosine function, originally based on the work of Eldredge et al. [32] and modified by Granlund et al. [24] was used to match the acceleration profile of the pitching servo motion across various pitch rates.

$$\alpha(t) = \frac{2\alpha_{\max}(1-\sigma)}{\pi^2} \ln \left[\frac{\cosh\left(\frac{\pi^2 K}{4\alpha_{\max}(1-\sigma)}(t^* - t_1^*)\right)}{\cosh\left(\frac{\pi^2 K}{4\alpha_{\max}(1-\sigma)}(t^* - t_1^* - \frac{\alpha_{\max}}{K})\right)} \right] + \frac{\alpha_{\max}}{2} \tag{2.1}$$

This function is based on various parameters such as the maximum pitch angle (α_{max}), non-dimensional time (t^*), the starting point of the sharp ramp corner (t_1^*), the ideal constant-pitch-rate period (α_{max}/K), and a smoothing parameter (σ). Acceleration and pitch speed calibration of the servo motor was carried out by varying the smoothing parameter σ to match the measured profile. The complete details of the calibration methodology are given in the Appendix A. A comparison of the measured pitch ramp motion with the revised hyperbolic-cosine function at $Re = 5,000$ for reduced pitch rate $K = 0.2$, $\alpha_{max} = 90°$ and $x_p/c = 0.5$ is shown in figure 2.4.
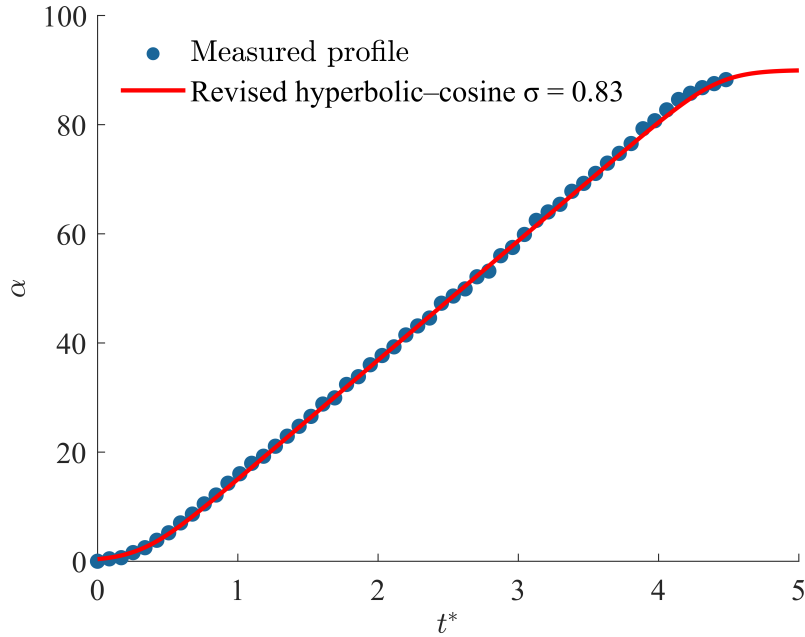
Figure 2.4: Comparison of the measured acceleration - deceleration pitch ramp motion with the revised hyperbolic-cosine function for $K = 0.2$, $\alpha_{max} = 90°$ and $x_p/c = 0$

2.2 Aerodynamic loads measurement

Six force and moment components were measured using a water-submergible ATI Nano 17 / IP 68 force sensor with a resolution of $1/320$ N for forces and $1/64$ Nmm for torque about three axis. Aerodynamic loads data were acquired at a frequency of 5 kHz using a custom built LabVIEW code that synchronized wing motion with aerodynamic loads data acquisition. Five sets of experiments were performed for each case and then ensemble averaged to get the final force and moment values. Static tests were conducted to measure forces when the wing was not rotating, and the data were averaged and subtracted from the averaged loads data to remove the residual strain of the load cell. The load cell was mounted inside the mirror holder in such as way that its x-axis and y-axis were aligned with the direction of normal and axial directions of the rotating wing, respectively. The averaged data were filtered using a low-pass fourth order Butterworth filter. The cutoff frequency for each case was set at 10 times the pitching frequency to obtain the desired aerodynamic loads and remove electrical noise and frame vibrations. MATLAB filtfilt command was used to prevent any time shift of data within the passband. Figure 2.5 depicts the instantaneous single run normal and axial

15

forces, superimposed with five run ensemble averaged data then the final data after the filtering process for $K = 0.2$ and leading edge pivot location case. It can be seen from the figure that the magnitude of axial force is much lower than the normal force.
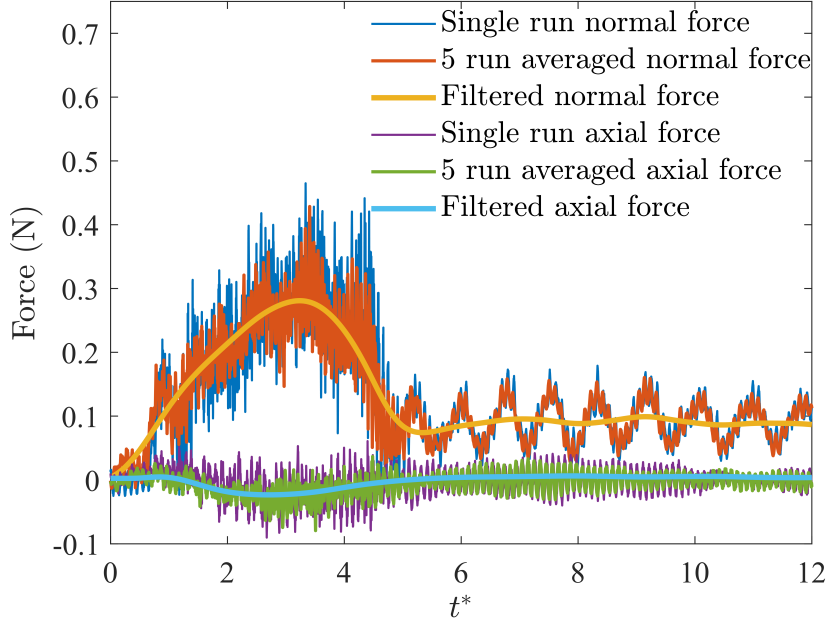
Figure 2.5: Comparison of instantaneous and five run averaged measured normal and axial forces with the filtered data

2.3 Particle image velocimetry (PIV) in rotating frame of reference

The present study investigates the time-resolved flow field over a rotating and pitching wing at the radius of the gyration plane using particle image velocimetry (PIV) in the rotating frame of reference (FoR). To visualize the flow field in the rotating frame, a mirror is mounted on the bottom inclined surface of the mirror holder. The mirror is positioned at the hub so that it simultaneously rotates along with the wing. The imaging is done by using a stationary high-speed camera which is mounted co-axially with the mirror, while a volumetric light source is used to illuminate the flow field. The flow field evolving over the wing is reflected onto the mirror as the wing rotates, which is then captured by the co-axially mounted camera. This method allows for the continuous study of the time-resolved flow field over a rotating wing.

PIV in rotating FoR operates in a similar manner to conventional PIV in that the tracer particles are introduced in the flow field and a camera records images of particles illuminated by a pulsed light source. The displacement between the corresponding particles in consecutive images can then be found. These displacements are then used to compute the velocity field. The imaging system used in this study consists of a Nikon $200\ mm$ main lens mounted on the Phantom VEO 4K 990L high-speed camera which is co-axial with the mirror. The camera has the ability to capture images at $938\ fps$ at 4096 x 2304 pixels (9.4 megapixels). The illumination of the flow field is achieved with a LaVision Flashlight–300 LED, which has a warm white color with an intensity peak in blue light ($445\ nm$). To visualize the flow field, PMMA rhodamine fluorescent particles were used. The particles have a diameter range of $63-75\ \mu m$ and absorb wavelengths in the range of $430-565\ nm$ and emit light at a wavelength of $590-625\ nm$. A $52\ mm$ Tiffen Orange 21 filter was inserted into the main lens to filter out reflections from the light source. The schematic for the PIV setup has been shown in figure 2.6. To account for the rotating field of view in the camera's FoR, a rotational calibration methodology was developed. In order to optimize the quality of raw image data for subsequent PIV cross-correlation, a series of pre-processing filters were applied using ImageJ software. Each step in pre-processing serves a specific purpose in enhancing the image quality and ensuring good signal-to-noise ratio. The details of pre-processing steps and their specific threshold values are given in table 2.2. The initial step involves background subtraction, where a rolling ball algorithm with a radius of 50 pixels is applied to eliminate uneven illumination, ensuring a more uniform background. Subsequently, mean intensity subtraction is employed to mitigate variations in overall brightness, enhancing contrast for improved clarity. Gaussian Blur is then applied to smoothen the image and reduce noise through convolution with a Gaussian kernel. The unsharp mask operation enhances edges and fine details by subtracting a blurred version of the image. Lastly, the variance operation computes the local variance of pixel intensities within a 2 pixel radius. Figure 2.7 shows the comparison of a raw image acquired at the radius of gyration plane with the filtered image after pre-processing steps for $x_p/c = 0$ and $K = 0.2$.
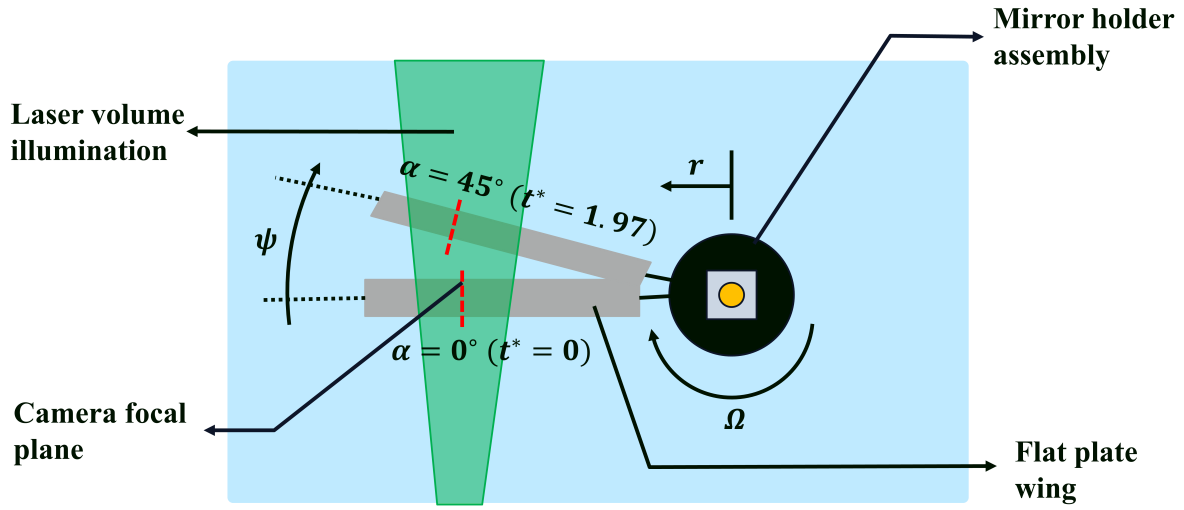
Figure 2.6: Schematic (not to scale) of PIV setup with red dotted line showing the spanwise location of image acquisition

2.3.1 Rotational calibration methodology

In the experimental setup, as a stationary camera was used to capture images of the wing through a rotating mirror, resulting in a continuous rotation effect about the central axis. Therefore, a rotational calibration method was developed to mitigate the effect of the rotating field of view. Furthermore, mere rotation of the images from one azimuth angle did not give good results because the image distortion was also fixed relative to the sensor.

The procedure for rotational calibration starts with image acquisition of a patterned calibration board at a specified plane that coincides with the spanwise location of actual PIV images. It involves conducting discrete calibrations at various azimuth angles. To establish image-to-object mapping, a 3rd-order polynomial fit is used to correlate the imaged board pattern with its known physical positions. The coordinate system of the calibration plate undergoes rotation to align with the rotation of the wing. Consequently, each calibration point's location is defined with respect to ψ (azimuth angle). In other words, for a specific dot in figure 2.8 (a), denoted as (x, y, z), its equivalent in figure 2.8 (b) becomes (x', y', z'). This adjustment enables

Step #	Operation	Value
1	Background subtraction	Rolling ball radius = 50 pixels
2	Mean intensity subtraction	7
3	Gaussian Blur	Sigma (radius) = 2
4	Unsharp mask	Radius (sigma) = 1 pixel Mask weight = 0.8
5	Variance	Radius = 2 pixel

Table 2.2: Image pre-processing filters

(a)   (b)
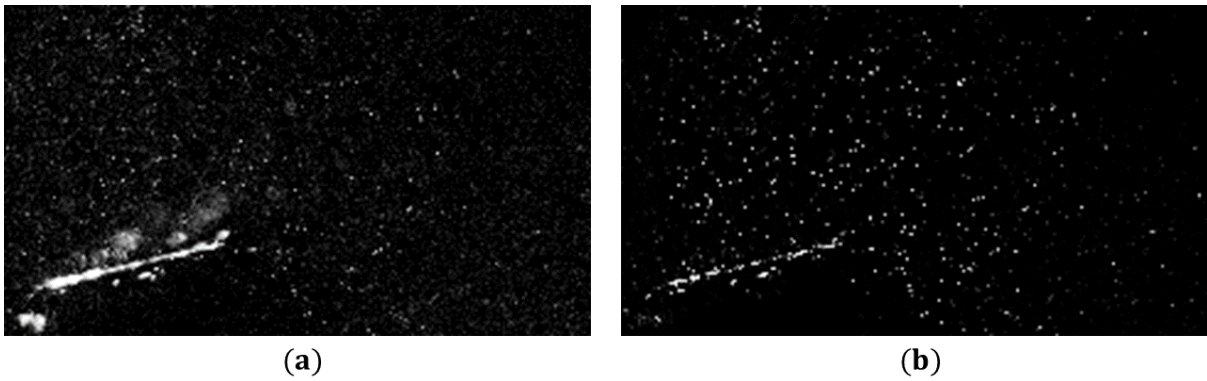
Figure 2.7: Comparison of raw image (a) with the filtered image (b) after pre-processing in ImageJ

the calibration polynomial to effectively map a point in object space at a given azimuth angle, ψ, to image space. The application of the rotational volumetric calibration method to the rotated dot card in figure 2.8 (b) produces figure 2.8 (c), wherein the calibration plate's axes align with those in figure 2.8 (a). For the current experimental setup, calibration images were taken from recorded data at approximately every $10°$ in azimuth angle, covering a total range of $120°$. The resulting mapping function, generated from rotational calibration, was then applied to the raw images resulting in the calibrated images in which the wing rotation effect about the central axis had been removed and the wing appeared stationary. It created a visual impression that the camera was also rotating along with the wing. This adjustment significantly streamlines the analysis of cross-correlated vector fields. More details on this calibration methodology can be found in the paper by Gururaj et al. [48].

19
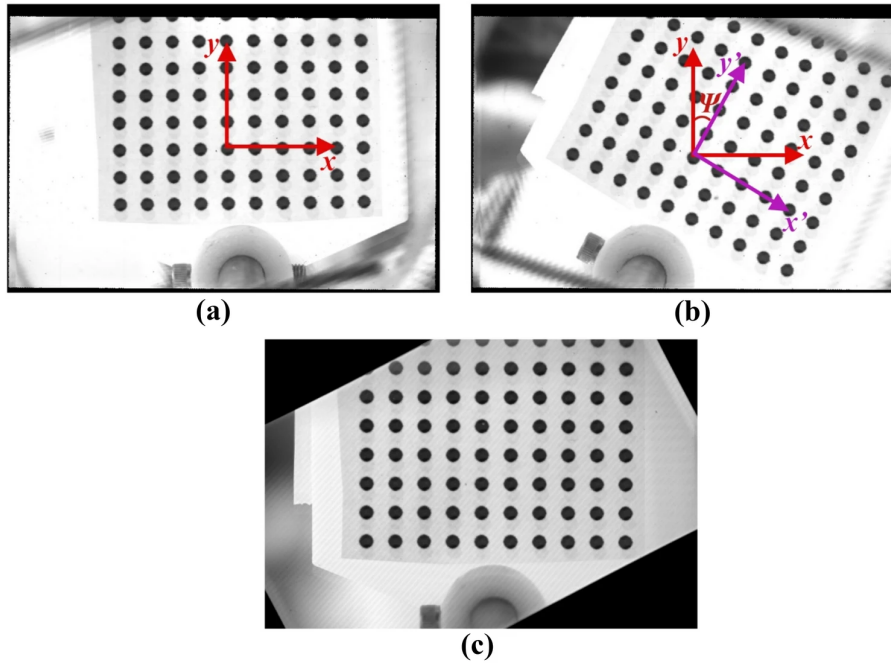
Figure 2.8: Coordinate axes in image (a) used as a reference in applying rotational calibration to a rotated dot card (b) to obtain the resulting calibrated image (c)

2.3.2 PIV image cross-correlation

Image cross-correlation was performed in MATLAB PIV Lab application using the PIV algorithm based on the FFT window deformation. Square interrogation windows were employed four times with varying sizes of 96, 64, 48 and 36 pixels and corresponding step sizes of 32, 32, 24 and 12 pixels respectively. Auto-correlation was disabled, and high correlation robustness settings were selected. The velocity field was refined in post processing through the application of a standard deviation filter (threshold: 8) to eliminate outliers and vectors with high uncertainty, while a local median filter (threshold: 3) provided additional smoothing. The measurement uncertainties associated with PIV data are usually due to random error and bias error. Random error depends on the particle image diameter, interrogation window size, and flow conditions, and it increases with smaller window sizes [52]. The final window size of 36 x 36 pixels was selected to maintain a balance between the spatial resolution and random error. Bias error, primarily associated with peak locking tendency for displacements to favor integer pixel values was found to be significantly less than the random noise error. Knowing the time between the successive images, the calibration of the velocity field was carried out by dot card

20

images (refer figure 2.8) of known displacement. PIV velocity field data in far field was also compared to the theoretical value of free stream velocity at the spanwise location where the images were captured. The measurement uncertainity was found to be with in 5%. Furthermore, the PIV correlation coefficient value was found to be varying between 0.88 - 0.92 which also supported the robustness of cross correlated vector field. The cross-correlated data were exported and then spatial and temporal vector smoothing, with both spatial and temporal kernels of 3, was applied in a separate MATLAB algorithm. Finally, the post processed velocity data were loaded into Tecplot software for visualization of the flow field over the wing surface. Figure 2.9 shows a visual representation of PIV data acquired at radius of gyration plane for $K = 0.2$ and $x_p/c = 0.50$ case.
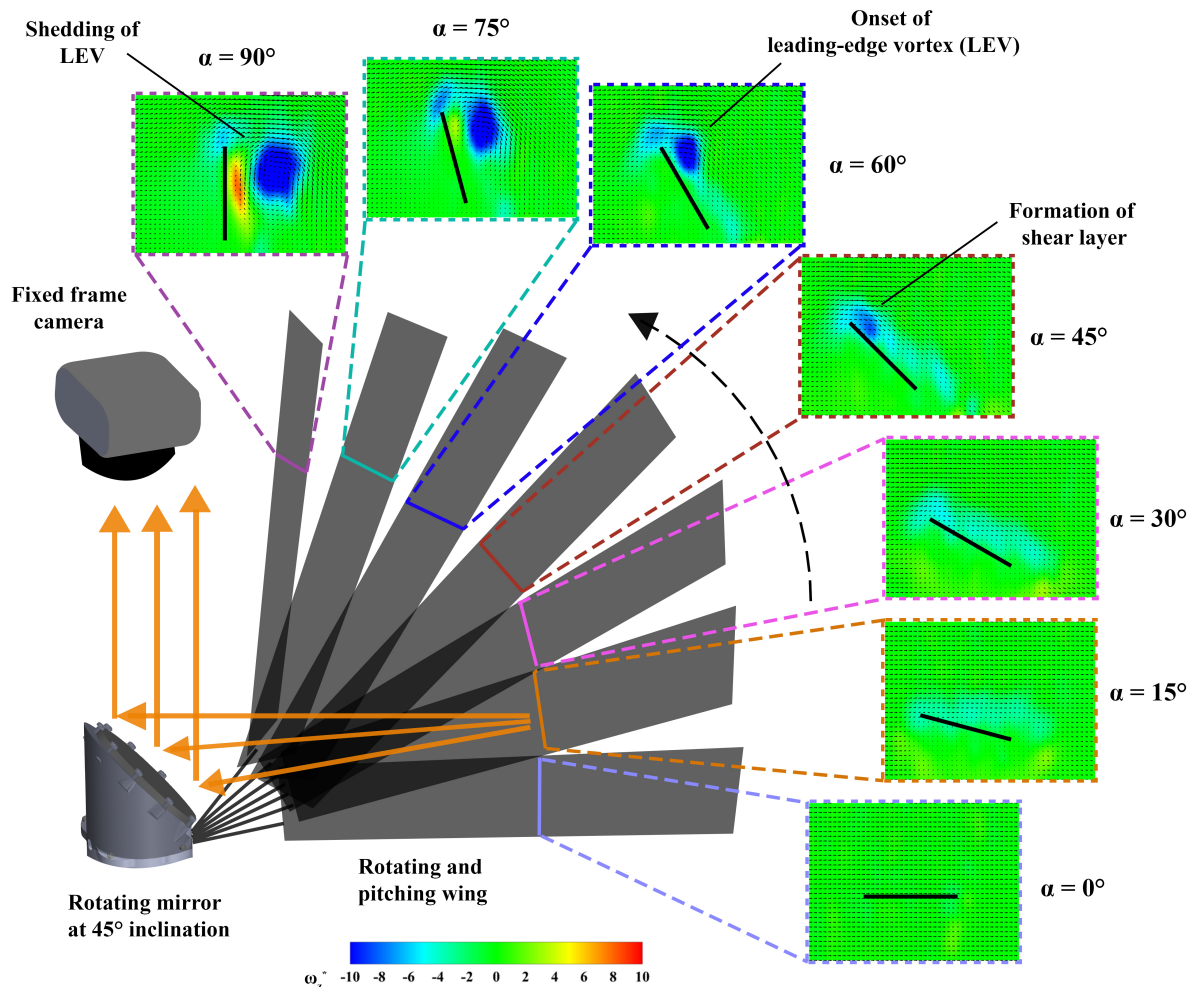
Figure 2.9: Representation (not to scale) of PIV data acquired at radius of gyration plane for $K = 0.2$ and $x_p/c = 0.50$

2.4 Data analysis

2.4.1 Aerodynamic loads data analysis

The load cell was mounted inside the mirror holder, so that its x-axis was aligned with the normal direction and the y-axis with the axial direction of the rotating wing. In addition to dynamic fluid loads, this set-up was designed such that the weight of the connecting rod and the flat plate was also measured by the load cell. During the pitching motion from $0 - 90°$, the wing's weight also shifted from one axis to the other. To accurately isolate fluid dynamic loads from the overall weight of the load cell, the weight of the flat plate and connecting rod was meticulously measured inside water. The net measured forces in both the x and y axes of the load cell were subsequently tared by using trigonometric cosine and sine functions. This adjustment accounted for the weight shifting of the load cell / connecting rod and the fluid dynamic loads were successfully isolated from the net loads measured by the load cell.

As the pitch angle (α) was known throughout the pitching motion, the aerodynamic loads data in the normal and axial directions were converted into lift and drag by applying coordinate transformation equations (see equation 2.2). Subsequently, the lift and drag were normalized to obtain the lift "C_L" and drag "C_D" coefficients respectively (see equation 2.3), where L is the lift force and D is the drag force, ρ is the density of fluid, Ω is the steady state angular velocity, R is the distance of the tip from the axis of rotation, b is the wingspan and c is the wing chord. Likewise, the moment coefficient "C_M" was determined by dividing the pitching moment M by the product of dynamic pressure, reference area, and chord length (see equation 2.4). Figure 2.10 (a) shows the schematic of the aerodynamic forces and pitching moment experienced by the flat plate. The resultant aerodynamic force R is a combination of a normal and axial forces as measured directly by the load cell. Furthermore, Figure 2.10 (b) shows the measured normal and axial forces and their associated lift and drag components when plotted against the non-dimensional convective time for $K = 0.1$ and $x_p/c = 0$. It can be seen that neither the maximum value of normal force nor its corresponding non-dimensional convective time aligns with the maximum value of lift or drag.
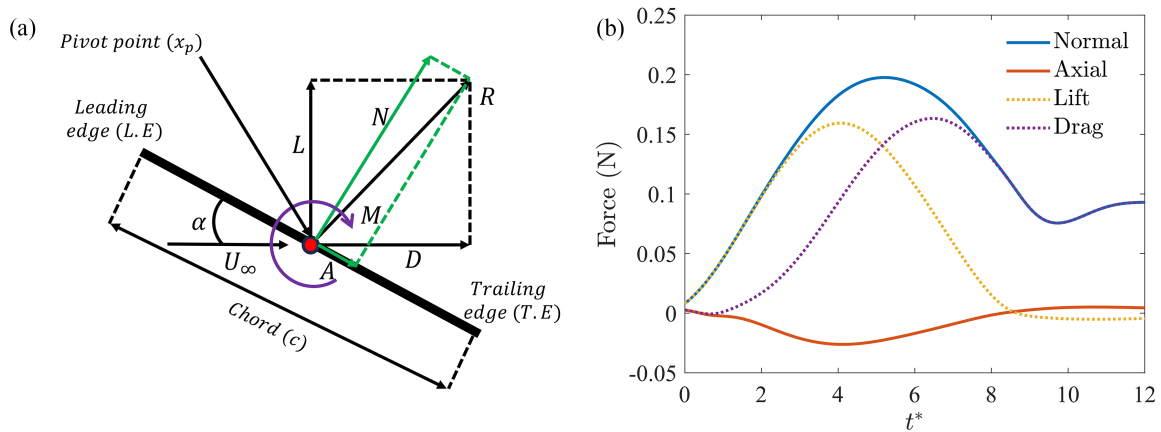
Figure 2.10: Aerodynamic forces and pitching moment on the flat plate (a), Measured normal and axial forces and their associated lift and drag components plotted against the non-dimensional convective time for $K = 0.1$ and $x_p/c = 0$ (b)

$$L = N \cos \alpha - A \sin \alpha \qquad\qquad D = N \sin \alpha + A \cos \alpha \qquad (2.2)$$

$$C_L = \frac{L}{\frac{1}{2}\rho(\Omega R)^2 bc} \qquad\qquad C_D = \frac{D}{\frac{1}{2}\rho(\Omega R)^2 bc} \qquad (2.3)$$

$$C_M = \frac{M}{\frac{1}{2}\rho(\Omega R)^2 bc^2} \qquad (2.4)$$

2.4.2 PIV data analysis

In order to quantitatively investigate the development and progression of the leading-edge vortex in the context of simultaneously pitching and rotating flat plate, the vortex identification methodology proposed by Graftieaux et al. [53] was employed. The criteria involves the calculation of two scalar fields, Γ_1 and Γ_2, which are used to identify the regions dominated by rotation and represent the vortex core. The scalar field Γ_1 is calculated by considering only the topology of the velocity field, and not its magnitude. The magnitude of Γ_1 is bounded by one and is calculated on 2D velocity planes in the chordwise direction, where z is the unit normal vector of the plane. The vortex center is identified as a local maximum of the Γ_1 field. In our investigation, we computed Γ_1 at the radius of gyration plane and established a threshold value

of $\Gamma_1 \geq 0.8$ to pinpoint the regions where Γ_1 attains its peak spatial value, thereby signifying vortex centers.

$$\Gamma_1(P) = \frac{1}{N} \sum_M \frac{[\mathbf{R}_{PM} \wedge (\mathbf{U}_M)] \cdot \mathbf{z}}{\|\mathbf{R}_{PM}\| \cdot \|\mathbf{U}_M\|} = \frac{1}{N} \sum_M sin(\theta_M) \qquad (2.5)$$

Once the vortex center is identified, the Γ_2 criterion is used to determine the vortex core size. The previously defined scalar field of Γ_1 is modified to take into account the local advection velocity U_P around P. Regions where $|\Gamma_2| > 2/\pi$ are locally dominated by rotation and represent a vortex core. The LEV circulation was determined by integrating the vorticity in the core of the vortex detected by the Γ_2 criterion as proposed by Graftieaux et al. [53].

$$\Gamma_2(P) = \frac{1}{N} \sum_M \frac{[\mathbf{R}_{PM} \wedge (\mathbf{U}_M - \mathbf{U}_P)] \cdot \mathbf{z}}{\|\mathbf{R}_{PM}\| \cdot \|\mathbf{U}_M - \mathbf{U}_P\|} \qquad (2.6)$$

The Γ_2 criterion generates the cutoff boundary for vortex core such that when the LEV is attached to the plate, the contour encompasses segments of the adjacent shear layer near the leading edge, which results in augmented strength of the computed LEV circulation. As soon as LEV detaches from the attached shear layer, there is a slight reduction in circulation. The observed decrease is actually an artifact of added circulation from the high value of vorticity in the vicinity of the leading edge during the pitching motion, which is no longer captured by the Γ_2 contour. The circulation of the leading-edge vortex (LEV) is determined by integrating the vorticity (ω_z) inside the vortex core, which is identified using the Graftieaux criteria. The spanwise vorticity (ω_z) and circulation (Γ_z) data for the 2D slices are then non-dimensioanalized by the tip velocity (U_{tip}) and chord length (c) of the rotating wing.

$$\omega_z^* = \frac{\omega_z c}{U_{tip}} \qquad \qquad \Gamma_z^* = \frac{\Gamma_z}{U_{tip} c} \qquad (2.7)$$

Chapter 3

Results and discussions

3.1 Effect of reduced pitch rate

3.1.1 Aerodynamic loads analysis

As discussed in section 2.4.1, the resultant aerodynamic force is perpendicular to the plate's surface, with lift and drag acting as projections along their respective directions. The influence of the reduced pitch rate K on the lift and drag coefficients during pitch motion from $0°$ to $90°$ is depicted in figure 3.1 and 3.2 respectively. The results are shown for all the pivot locations starting from $x_p/c = 0$ till $x_p/c = 1$. Considering only the mid-chord pivot location ($x_p/c = 0.50$), two prominent effects of K on the lift coefficient are observed: both the maximum lift coefficient and the corresponding pitch angle for max lift gradually increase with higher K values. For the lowest pitch rates ($K = 0.02 - 0.03$), the primary effect of pitch motion is limited to a delay in the onset of stall. However, for higher reduced pitch rates, $K \geq 0.05$, the influence of unsteady effects become more prominent, leading to a noticeable bump in the lift coefficient as K increases. Both the peak lift value and the pitch angle at which peak lift occurs exhibit a consistent increase as the reduced pitch rate K increases. At even higher pitch rates, the peak lift coefficient continues to increase, but the pitch angle for peak lift reaches a saturation value at approximately $\alpha \approx 42°$. The maximum lift coefficient and the corresponding pitch angle show gradual increases but appear to reach a saturation point at $K = 0.2$, for which $C_{L_{max}} \approx 1.86$ (at $\alpha \approx 41.8°$).

Similarly, at $x_p/c = 0.50$, as the reduced pitch rate increases, there is a consistent increase in the drag coefficient, as illustrated in figure 3.2(c). When $K \leq 0.03$, the drag coefficient closely follows the steady theoretical results for a finite wing as given by Glauert [54, 55].
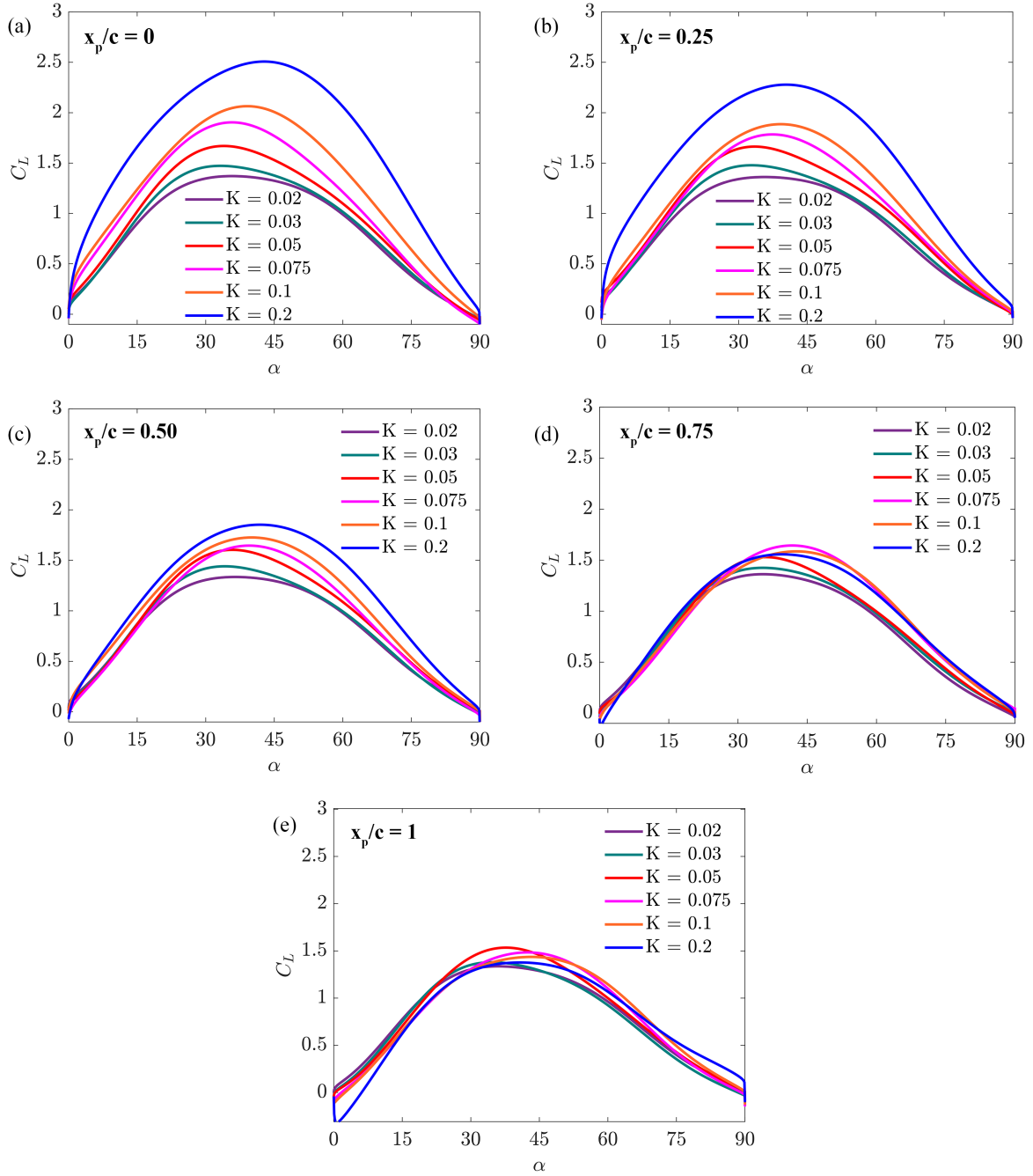
Figure 3.1: Lift coefficients comparing reduced pitch rates $K = 0.02, 0.03, 0.05, 0.075, 0.1, 0.2$ at a constant pitch pivot location $x_p/c = 0$ (a), $x_p/c = 0.25$ (b), $x_p/c = 0.50$ (c), $x_p/c = 0.75$ (d) and $x_p/c = 1$ (e)

However, for higher reduced pitch rates ($K \geq 0.05$), the drag coefficient deviates from the theoretical steady-state behavior, and a noticeable increase in drag coefficient becomes evident for $K \geq 0.075$. Specifically, at $K = 0.2$, the maximum drag coefficient ($C_{D_{max}} \approx 2.4$) occurs at a pitch angle of $\alpha \approx 65°$, exceeding the maximum drag coefficient for $K = 0.02$ by approximately two times.

Now, if we consider the pivot location as $x_p/c = 0$ or 1, we start observing unique trends with respect to variation with K. We can see from figures 3.1 and 3.2 that increasing K for a constant pitch pivot location does not necessarily leads to an increase in both lift and drag coefficients. The rise in lift or drag is coupled with pitch pivot location as well. For example, the respective rise in C_L and C_D by increasing reduced pitch rate K from 0.02 to 0.2 is highest for $x_p/c = 0$ as shown in figure 3.1(a) and 3.2(a) respectively. The difference between different curves starts decreasing for $x_p/c = 0.50$. However, when we move towards the trailing edge pivot location, we do not observe an increase C_L and C_D for all K cases and all the curves fall on top of one another (refer figure 3.1(e) and 3.2(e)). This means that a statement based solely on reduced pitch rate does not offer definitive prediction of aerodynamic loads. But the combined effect of reduced pitch rate and pivot location gives the resultant aerodynamic loads experienced by the wing.

The effect of reduced pitch rate on the moment coefficient of a pitching wing is of paramount importance for optimizing aerodynamic performance, aircraft stability and structural integrity. The effect of changing reduced pitch rate from $K = 0.02$–0.2 on the moment coefficient (C_M) is depicted in figure 3.3, while holding the pitch pivot location fixed at $x_p/c = 0$. As the pitch angle increases, C_M exhibits a consistent increase in negative direction across all the reduced pitch rates considered. Moreover, C_M slope increases progressively when varying K from 0.02 to 0.2. The most pronounced effect is observed at the highest reduced pitch rate ($K = 0.2$) considered in this study, where unsteady aerodynamic effects become more pronounced. This is manifested by an overshoot in C_M at high pitch angles, with $C_{M_{max}}$ reaching -1.83, more than two times the maximum C_M observed at $K = 0.02$ ($C_M = -0.85$). Furthermore, it is noteworthy that all pitch rates exhibit a drop in C_M after reaching $C_{M_{max}}$, ultimately converging to a value of approximately -0.75 as the wing approaches $90°$ pitch angle. The pitch angle for
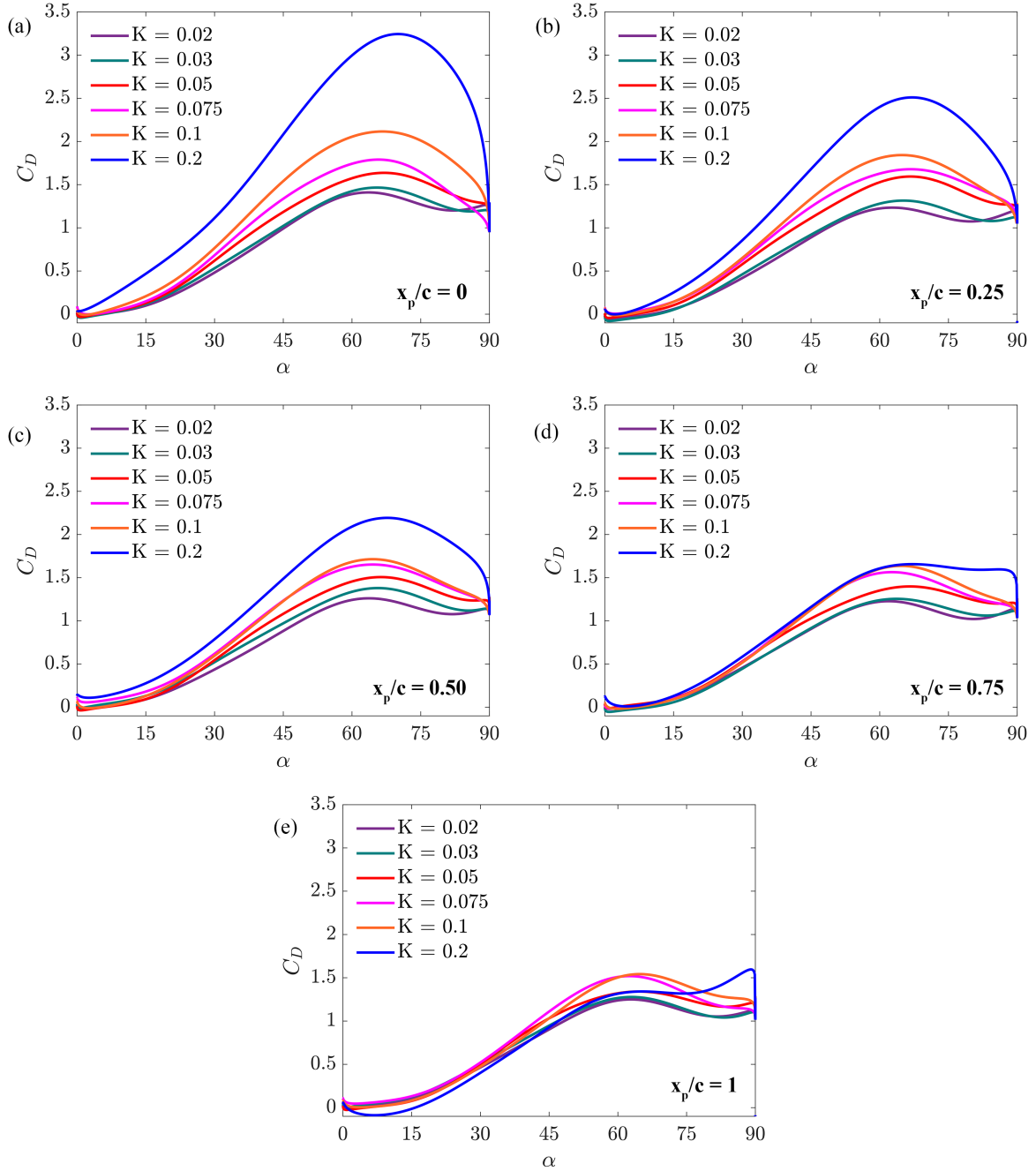
Figure 3.2: Drag coefficients comparing reduced pitch rates $K = 0.02, 0.03, 0.05, 0.075, 0.1, 0.2$ at a constant pitch pivot location $x_p/c = 0$ (a), $x_p/c = 0.25$ (b), $x_p/c = 0.50$ (c), $x_p/c = 0.75$ (d) and $x_p/c = 1$ (e)

28
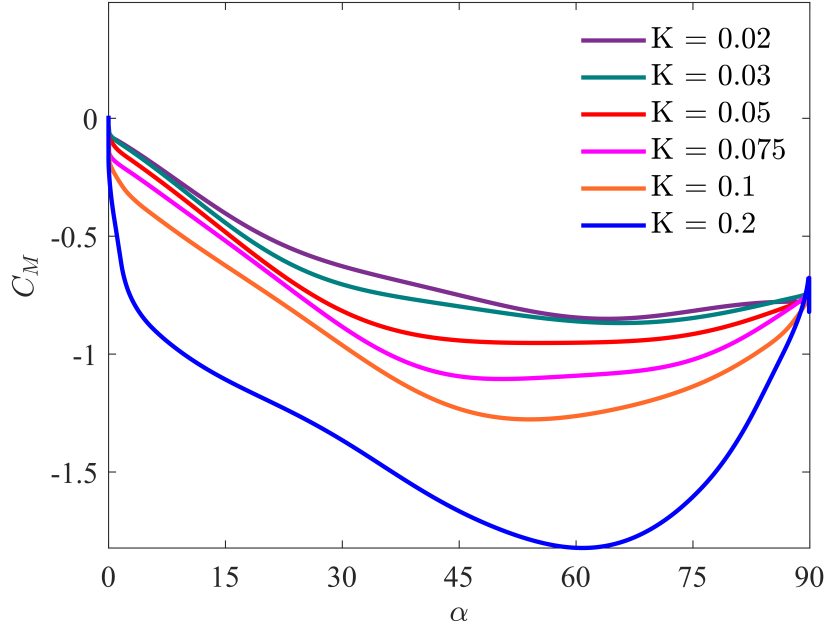
Figure 3.3: Moment coefficients comparing reduced pitch rates $K = 0.02, 0.03, 0.05, 0.075, 0.1, 0.2$ at a constant pitch pivot location $x_p/c = 0$

$C_{M_{max}}$ also increases with increasing K. These trends in C_M show resemblance to the trends in normal force coefficient (C_N), the magnitude of which is strongly influenced by the LEV formed on the wing's suction side.

3.1.2 Flow field analysis

According to previous studies [24, 56, 57, 26, 58, 59, 60], the increase in lift and drag for pitching wing is predominantly related to the development of LEV on the leeward side of the wing. Various researchers [30, 61, 62, 63], have investigated the flow characteristics prior to LEV formation. The dynamics start with the attached flow condition which is followed by flow reversal at the plate leading edge. After that, LEV starts forming and ultimately, the growth and feeding of LEV continues till it detaches from the shear layer. Throughout the flow evolution, a region of low pressure forms underneath the LEV [64]. This region grows both in magnitude and size as the LEV develops and then diminishes as the vortex detaches from the wing, resulting in a drop in lift [65]. The growth of LEV circulation is primarily governed by the convective fluxes of vorticity into the LEV. The main contributor to this growth is the vorticity in the shear layer, while the secondary vorticity in the boundary layer beneath the

vortex slows it growth by vorticity annihilation [66]. To conclude, the dynamics of LEV play a pivotal role in determining the aerodynamic loads acting on the pitching wing.

Figure 3.4 shows the vorticity plots for varying reduced pitch rates ($K = 0.05 - 0.2$) at a constant pitch pivot location ($x_p/c = 0.50$) and pitch angles of $30°$, $45°$, $60°$ and $75°$. At $K = 0.05$, a small leading-edge vortex forms and separates from the shear layer. Notably, at $45°$, two distinct small-scale LEVs appear on the wing's suction side. However, at $60°$ and $75°$, numerous small-scale vortices shed from the leading edge and lack a coherent vortex structure. For $K = 0.075$, the LEV is attached to the shear layer and evolving at $30°$. At $45°$, LEV grows into a compact structure with increased vorticity magnitude. Progressing to $60°$ and $75°$, we can see that the first LEV has convected downstream and just like $K = 0.05$ case, we again start seeing small scale streak of vortices being shed from the leading edge of the flat plate.

For $K = 0.1$, at a pitch angle of $30°$, only the formation of a shear layer at the leading edge of the flat plate is observed. Moving forward to $45°$, the shear layer vorticity rolls up into a coherent and compact LEV. Even at $60°$, the LEV still remains attached to the shear layer and progressively grows in size. The vorticity within the shear layer plays a crucial role in feeding vorticity inside the LEV. At pitch angle of $75°$, the LEV can be seen being separated from the shear layer, becoming less coherent and convecting downstream. Additionally, a distinctive positive-sign secondary vorticity near the surface of flat plate can be clearly seen at pitch angle of $75°$, which is produced due to the induced flow of the leading-edge vortex on the flat plate. This secondary vorticity eventually disrupts the flow of vorticity being feed from the shear layer into the LEV and leads to the separation of LEV from its attached shear layer.

For $K = 0.2$, we can clearly see that the formation of shear layer and roll-up into LEV has been delayed to higher pitch angles. At $60°$, a coherent leading edge vortex has been formed at the leading edge. At $75°$, LEV is still attached to the shear layer and growing in size. Therefore, the transition from low to high reduced pitch rates leads to significant differences in the flow evolution. A higher reduced pitch rate causes a delay in separation at the leading edge which subsequently results in a delay in the pitch angle for the shear layer and LEV formation. Higher pitch rates also lead to more vorticity being fed into the LEV that eventually becomes more compact and grows in size. This means that the reduced pitch rate is an important parameter
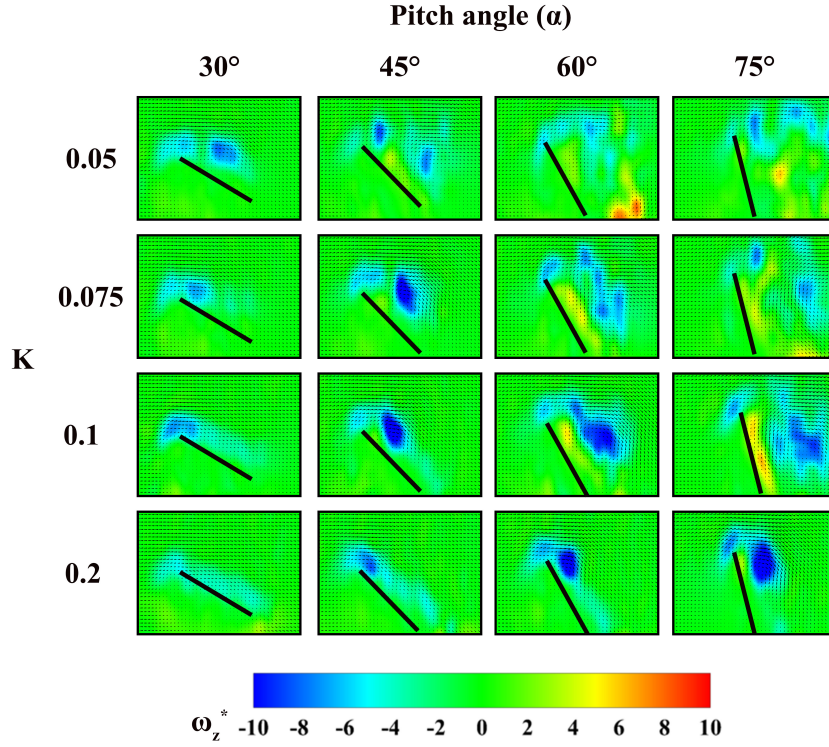
Figure 3.4: Vorticity plots comparing reduced pitch rates $K = 0.05, 0.075, 0.1, 0.2$ at pitch angles of $30°$, $45°$, $60°$ and $75°$, while keeping the pitch pivot location fixed at $x_p/c = 0.50$

which significantly affects various flow features like the formation and roll up of shear layer into LEV, amount of vorticity being fed into LEV, attainment of peak vorticity and eventually the shedding of LEV from the attached shear layer.

In figure 3.4, qualitative evolution of flow field was investigated by changing K from 0.05 to 0.2 at $x_p/c = 0.50$. To gain quantitative knowledge regarding the dynamics of LEV under same conditions, the non dimensional circulation (Γ_z^*) growth of LEV at the radius of gyration plane of flat plate is plotted in figure 3.5. The threshold values of Γ_1 and Γ_2 are set such that the criteria will detect the vortex core only when the rotationally dominant region is strong enough to resemble a vortex and it is in the field of view. The Γ_2 criterion also include portions of the adjacent shear layer near the leading edge, contributing to an increase in the strength of the computed LEV circulation. The temporary detachment of LEV from the shear layer leads to a momentary reduction in circulation. However, vorticity from the shear layer continues to contribute to the LEV until it reaches maximum circulation, fully detaches, and convects downstream.

Similar to Figure 3.4, separation occurs at an earlier pitch angle for the $K = 0.05$ case, leading to the detection of a vortex around $15°$ pitch angle. The vortex circulation exhibits fluctuating patterns across the graph without a clear trend. However, Γ_z^* does not exceed beyond -1. The observed circulation fluctuations stem from small-scale vortices being shed from the leading edge of the flat plate, with their strength continuously varying. For $K = 0.075$, the LEV is detected at around $30°$ pitch angle, indicating a delayed separation at the leading edge. Moreover, the peak LEV circulation is slightly higher compared to the $K = 0.05$ case. As the pitch angle increases to higher values, fluctuation in Γ_z^* start showing up due to small-scale streaks of vortices being shed from LE.

$K = 0.1$ case shows more distinctive characteristics. Firstly, LEV formation is delayed to higher α. Furthermore, Γ_z^* continues to increase until it reaches its maximum circulation at $\alpha = 75°$. Afterwards, the LEV completely detaches from the attached shear layer and we start seeing a decreasing trend in LEV circulation. As already seen in figure 3.4, LEV is more compact and larger in size for the $K = 0.1$ case; we also observe the same trend here such that $\Gamma_{z_{max}}^*$ is much higher for $K = 0.1$ than $K = 0.05$ and 0.075. For $K = 0.2$, the LEV forms at a notably higher pitch angle of $60°$. As the pitch angle increases, the vortex circulation shows an increasing trend but we do not capture the peak LEV circulation. However, considering earlier trends, $\Gamma_{z_{max}}^*$ for $K = 0.2$ is anticipated to exceed that of $K = 0.1$ due to higher pitching speed assosiated with it.

3.2 Effect of pitch pivot location

3.2.1 Aerodynamic loads analysis

The previous discussion focused on changing the reduced pitch rate while maintaining a constant pitch pivot location at the mid-chord of the plate. The influence of pitch rate on aerodynamic loads production is also significantly affected by the choice of pitch pivot location. The influence of different pivot axis positions ($x_p/c = 0, 0.25, 0.50, 0.75, 1.0$) on the lift and drag coefficients is depicted in figure 3.6 and 3.7 respectively, covering the range of reduced pitch rates from $K = 0.02 - 0.2$. For the lowest reduced pitch rate ($K = 0.02$) considered
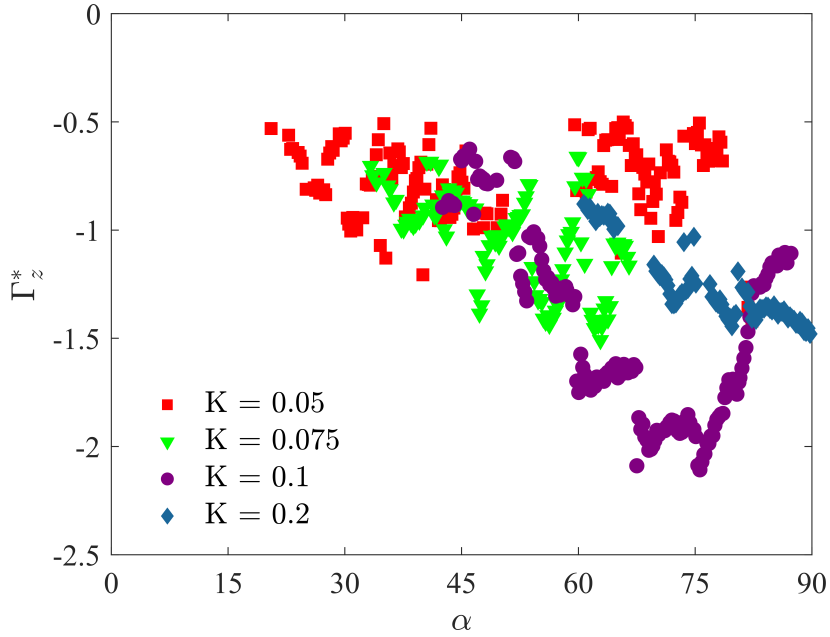
Figure 3.5: LEV circulation comparing reduced pitch rates $K = 0.05, 0.075, 0.1, 0.2$ at a constant pitch pivot location $x_p/c = 0.50$

in this study, the lift and drag coefficients show insignificant variations across different pivot locations. As the reduced pitch rate increase to $K = 0.2$, the dynamic lift and drag curves reveal more noticeable effects associated with the pitch pivot location. In particular, a consistent decrease in the lift coefficient (C_L) is observed as the pivot point moves towards the trailing edge. Furthermore, the slope of the lift coefficient (C_L) at lower pitch angles diminishes as the pivot point (x_p/c) changes from the leading edge towards the trailing edge. Furthermore, the maximum lift coefficient (C_L) reduces from 2.6 when $x_p/c = 0$ to 1.3 when $x_p/c = 1$. In the intermediate range ($0.05 \leq K \leq 0.1$), two distinct characteristics can be observed with respect to the variation in C_L as the pivot point is taken further aft. There is a decrease in C_L for aft pivot locations and the difference between the peaks becomes greater with higher K. Furthermore, the pitch angle corresponding to peak-lift increases for aft pivot locations but saturates at approximately $44°$. We can say that the pitching motion positively affects the generation of lift force for leading edge pivot location but for the trailing edge pivot location; the effect is negative and opposes the aerodynamic lift force.

The evolution of the drag coefficient also changes significantly for different pivot locations at $K = 0.2$ as compared to $K = 0.02$. For low reduced pitch rates ($K = 0.02$–0.03), the C_D

33
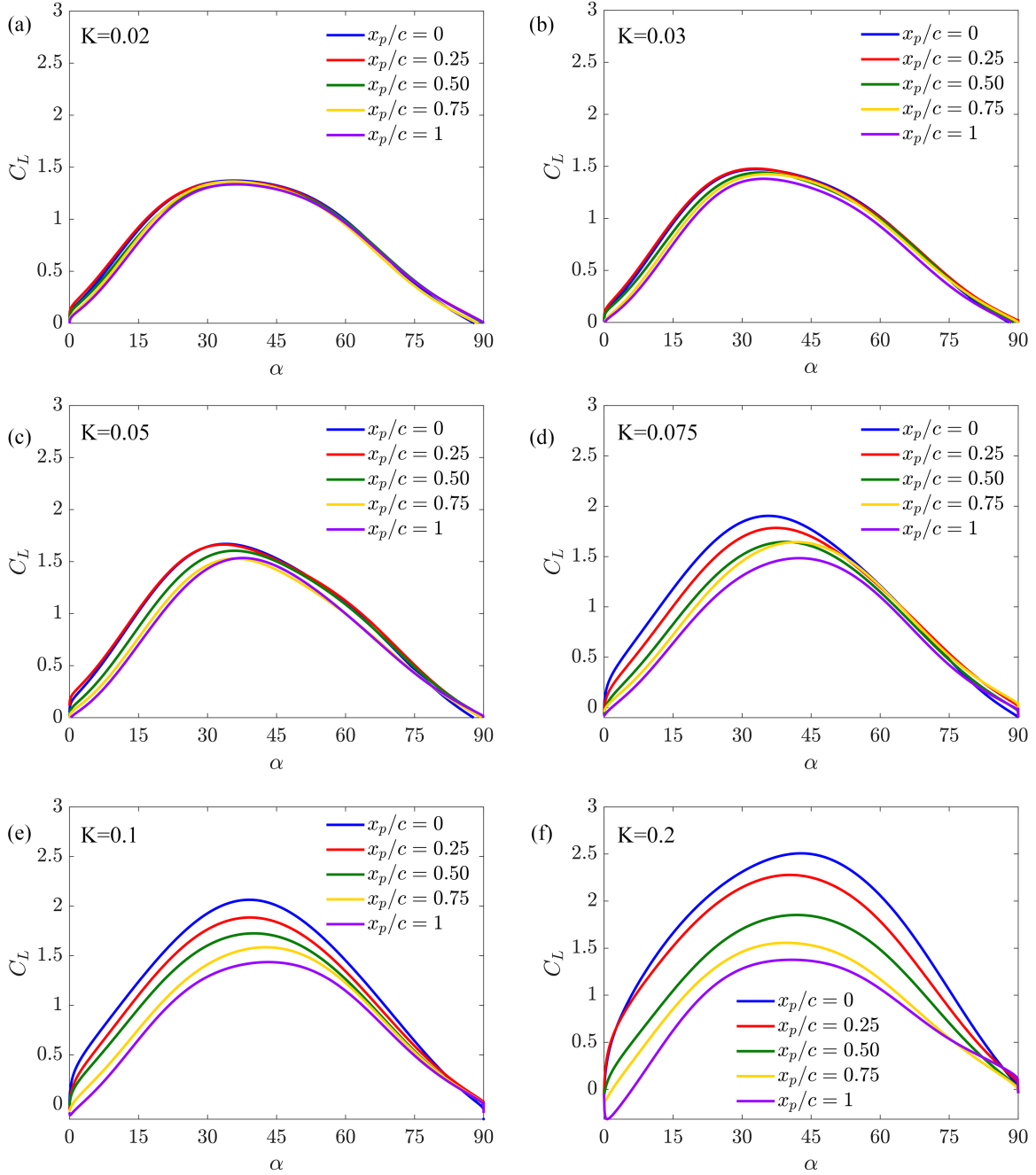
Figure 3.6: Lift coefficients comparing pivot locations $x_p/c = 0$, 0.25, 0.50, 0.75, 1 at a constant reduced pitch rate $K = 0.02$ (a), 0.03 (b), 0.05 (c), 0.075 (d), 0.1 (e) and 0.2 (f)

curves for different pivot locations follow the same trend. At reduced pitch rate $K = 0.05$, we observe a slight variation with respect to changing pivot locations. The pivot location effect starts to become dominant as we move towards higher reduced pitch rates ($K \geq 0.075$). At $K = 0.2$, we can clearly see a bump at higher pitch angles for leading edge pivot case, which shows a gradual decrease as we move towards the trailing edge pivot location. The maximum C_D is observed for $K = 0.2$ case and is found to be 3.3 at $x_p/c = 0$ and drops to the lowest value of 1.3 for $x_p/c = 1$ for same pitch angle α.

We can also examine the impact of acceleration and non-circulatory forces during transient motion. This force component accounts for the additional fluid inertia that arises when the wing undergoes acceleration. At low pitch angles (α), this motion mainly affects lift, while as the pitch angle (α) approaches $90°$, it predominantly starts influencing drag. For $x_p/c = 0$, the pitch acceleration at low pitch angle produces a finite non-circulatory force that shows up as a positive lift increment as seen in figure 3.6 (e,f), whereas the pitch deceleration at high pitch angle manifests itself as a decrement of drag as seen in figure 3.7 (e,f). In addition, the magnitude of the force spike continues to increase for higher reduced pitch rates K due to an increase in acceleration magnitude for higher K.

Unsteady airfoil theory [67] also compliment these results. For mid-chord pivot location ($x_p/c = 0.50$), the non-circulatory spike is zero, while for trailing edge pivot location ($x_p/c = 1$) it is negative. The non-circulatory contribution to lift at the start of pitch and drag at the end of pitch motion can be expressed in terms of kinematic expressions as given by [68]:

$$C_{L_{\text{non-circ}}} = \frac{\pi c^2}{4U_\infty^2} \left(1 - \frac{2x_p}{c}\right) \ddot{\alpha} \tag{3.1}$$

$$C_{D_{\text{non-circ}}} = \sin(\alpha_{\text{max}}) \frac{\pi c^2}{4U_\infty^2} \left(1 - \frac{2x_p}{c}\right) \ddot{\alpha} \tag{3.2}$$

The trend reversal for trailing edge pitch pivot location ($x_p/c = 1$) can also be seen in figures 3.6 (e,f) and 3.7 (e,f). There is a negative spike in C_L at low α for $x_p/c = 1$ and subsequently a positive spike in C_D at $\alpha \approx 90°$. The symmetry of added mass forces between lift during the pitch-starting transient and drag during the pitch-stopping transient can be attributed to the directional change of the non-circulatory force in the plate's normal direction, which
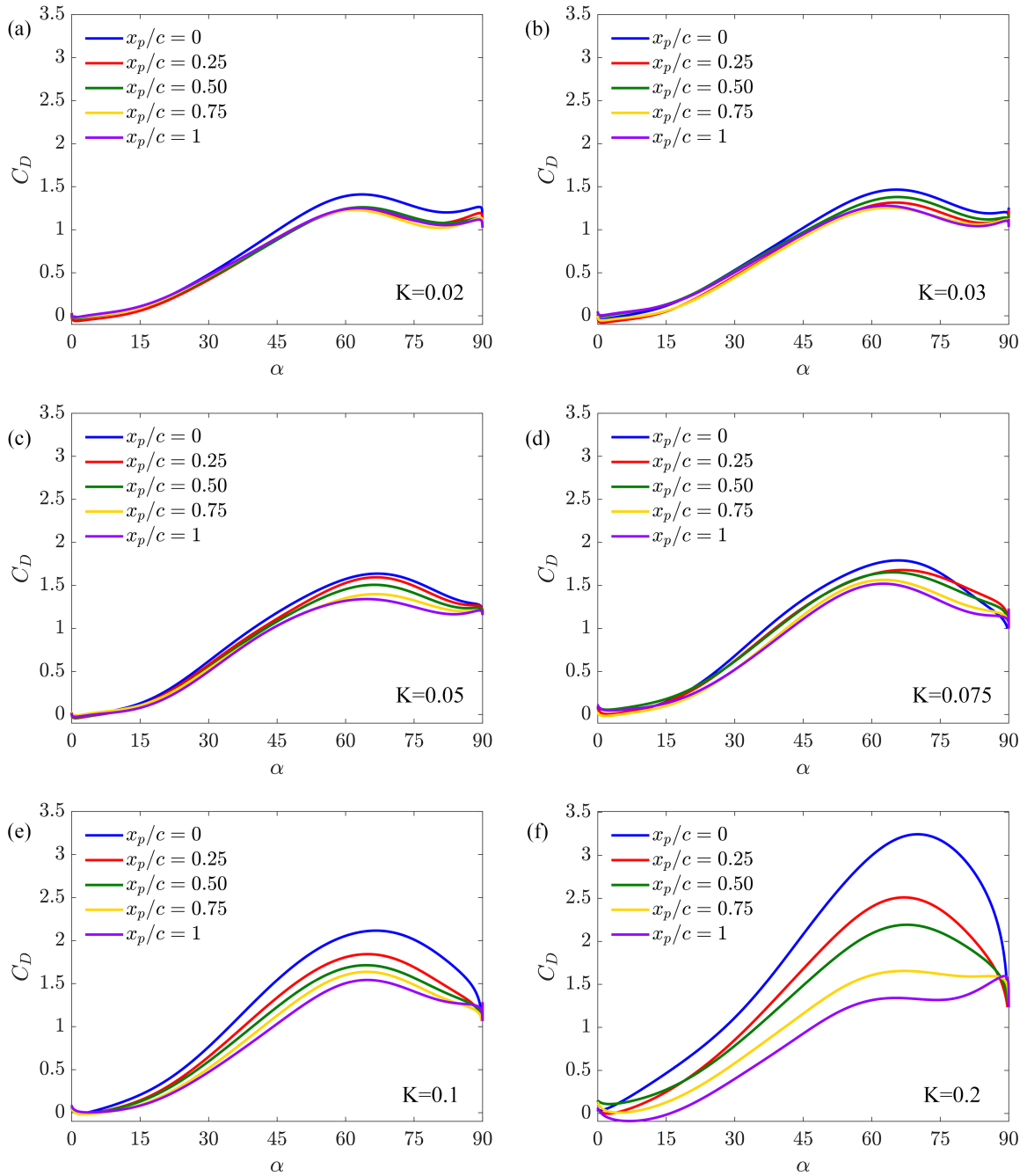
Figure 3.7: Drag coefficients comparing pivot locations $x_p/c = 0$, 0.25, 0.50, 0.75, 1 at a constant reduced pitch rate $K = 0.02$ (a), 0.03 (b), 0.05 (c), 0.075 (d), 0.1 (e) and 0.2 (f)

depends on the pitch pivot location during the pitching motion. During the initial acceleration of the wing at $x_p/c = 0$, the added mass force is experienced by the wing in the direction of wing suction side which results in a positive force spike in lift and the magnitude of spike increases with higher K due to increase in pitch acceleration ($\ddot{\alpha}$). Whereas during the cessation of motion at $90°$, deceleration is experienced by the wing, which results in an added mass force being exerted on the wing pressure side and subsequently results in a negative spike in drag. The trends become opposite for $x_p/c = 1$ due to change in direction of pitching motion. Now, the initial acceleration causes an added mass force on the wing pressure side which manifests itself as a negative force spike in lift. During final deceleration of the wing, a similar force is experienced by the wing, but this time, it acts on the wing suction side which results in a positive spike in drag. A study conducted by Yu and Bernal [23] also confirmed the formation of a starting vortex and stopping vortex during the initial and final transients for the wing respectively. Therefore, the combined effect of both the added mass force and circulatory force due to starting and stopping vortices manifests itself as spikes in the lift and drag coefficients for different pivot locations.

If we carefully analyze the rotation and pitching speeds for different cases, we find that for low reduced pitch rates ($K = 0.02$ and 0.03), pitching speed is less than the rotation speed and the effect of pitch induced fluid upwash or downwash for different pivot locations is minimal due to slow pitching speed. Also, since the constant pitch speed is achieved instantaneously, there would be a negligible added mass effect. Hence, as a crude approximation, we can neglect the $F_{inertial}$ and $F_{pitching}$ for these low reduced pitch rates and unsteady effects will be minimal. In that case, any force production will be due to circulatory effects due to wing rotation at that specific pitch angle. The resultant effect of pitching motion will be limited to stall delay and it would be approximately uniform across all the pivot locations. Therefore, we observe the same trend for all pitch pivot locations at $K = 0.02$ and 0.03. Therefore, we can define two regimes for reduced pitch rate K: Low reduced pitch rate regime ($K < 0.05$), where the primary effect of reduced pitch rate is the delay of stall pitch angle, as depicted in figures 3.6 and 3.7. Other would be high pitch rate regime ($K \geq 0.05$); when pitching speed becomes equal or higher than the rotation speed, the unsteady effects due to reduced pitch rate 'K' and pitch pivot location

Figure 3.8: Trends of maximum lift coefficients (a), and associated pitch angles (b) with changing reduced pitch rates for different pivot locations $x_p/c = 0, 0.25, 0.50, 0.75, 1$

'x_p/c' starts becoming dominant and has a significant contribution on the net aerodynamic loads.

A summary of the effects of pivot axis over a range of reduced pitch rates on the lift and drag coefficients is presented in figure 3.8 and 3.9. The trends for maximum lift coefficients with increasing K are reported in figure 3.8(a). For $K \leq 0.075$, figure 3.8(a) shows that $C_{L_{max}}$ increases almost linearly with K for all pivot point locations, except for the trailing edge pitch pivot location ($x_p/c = 1$) which shows a slight decrease at $K = 0.075$. For $K > 0.075$, $C_{L_{max}}$ keeps increasing almost linearly with K for $x_p/c = 0 \rightarrow 0.50$, but the rate of increase of $C_{L_{max}}$ with K decreases for aft pivot locations which ultimately results in a lower $C_{L_{max}}$ at $K = 0.2$ for $x_p/c = 0.50$ as compared to $x_p/c = 0$. For $x_p/c = 0.75$; $C_{L_{max}}$ seems to saturate beyond $K = 0.075$ and remains almost constant. However, C_L peak saturation of $x_p/c = 1$ is reached at $K = 0.05$; beyond which increase in pitch rate starts effecting negatively on the max lift coefficient ($C_{L_{max}}$). Therefore, we can conclude that in high reduced pitch rate regime ($K \geq 0.05$), increasing reduced pitch rate K contributes positively to the lift and is also proportional to the distance of pitch pivot location to the three-quarter chord point. If the pivot location is itself at $x_p/c = 0.75$, then $C_{L_{max}}$ will be insensitive to changing reduced pitch rate K, as shown in figure 3.8(a). This result is also consistent with the Theodorsen function as discussed in [47, 69].

Pitch angles at which the maximum lift coefficients are attained are plotted in figure 3.8(b). Due to filtering applied to the aerodynamic loads data and smooth stall behaviour of the flat plate, an exact evaluation of the pitch angle associated with $C_{L_{max}}$ is difficult at the lowest reduced pitch rates ($K = 0.02, 0.03$). For $K = 0.02$, $C_{L_{max}}$ is almost reached at approximately $25°$ and saturates afterwards until we observe a decreasing slope at approximately $50°$. In the intermediate region ($25 - 50°$); we see a marginal increase in C_L from 1.35 to 1.4, which shifts the pitch angle for $C_{L_{max}}$ to $36°$ degree for $K = 0.02$. In case of $K = 0.03$, the unsteady effect is more pronounced and $C_{L_{max}}$ is higher than $K = 0.02$ and we see a more prominent peak at approximately $34°$ and beyond that we start seeing a decreasing slope. As already reported in the previous studies [24, 70], the low reduced pitch rate regime is limited to delay in stall angle of attack. For high reduced pitch rate regime ($K \geq 0.05$); we see an overall increasing trend of $\alpha_{C_{L_{max}}}$ for all pitch rates and pivot locations. If we consider the isolated effect pitch pivot location, we observe a gradual reduction of $C_{L_{max}}$ when the pivot point moves from the leading edge to the trailing edge, but it is associated with a gradual increase of the associated pitch angle for peak C_L as shown in figure 3.8(b). Furthermore, consistent with the previous studies [24], a saturation of the pitch angle associated with the peak lift coefficient at approximately $42°$ is also observed. According to past literature [71, 23], higher K values are associated with pronounced unsteady effects and results in changes in flow field characteristics such as the formation of LEV that significantly affect aerodynamic loads. Furthermore, LEV formation time is also delayed with increasing pitch rate and pitch pivot location [24]. The delay in LEV formation time might be associated with a decrease in $\alpha_{C_{L_{max}}}$ for $x_p/c = 0.75$ and 1 at $K = 0.2$ as compared to $K = 0.1$.

The summary of drag coefficients (C_D) with respect to variations in $C_{D_{max}}$ and $\alpha_{C_{D_{max}}}$ is shown in figure 3.9. $C_{D_{max}}$ increases with increasing reduced pitch rate K for all pivot locations. $\alpha_{C_{D_{max}}}$ also shows an overall increasing trend with K with $\alpha_{C_{D_{max}}}$ higher for $x_p/c = 0$ as compared to $x_p/c = 1$. Trailing edge pivot location ($x_p/c = 1$) shows a unique behavior at $K = 0.2$, with $\alpha_{C_{D_{max}}}$ occurring at $90°$ pitch angle. This deviation in trend can be attributed to the sharp non-circulatory spike during the pitch stopping transient which causes the $C_{D_{max}}$ to occur at the end of pitch motion.
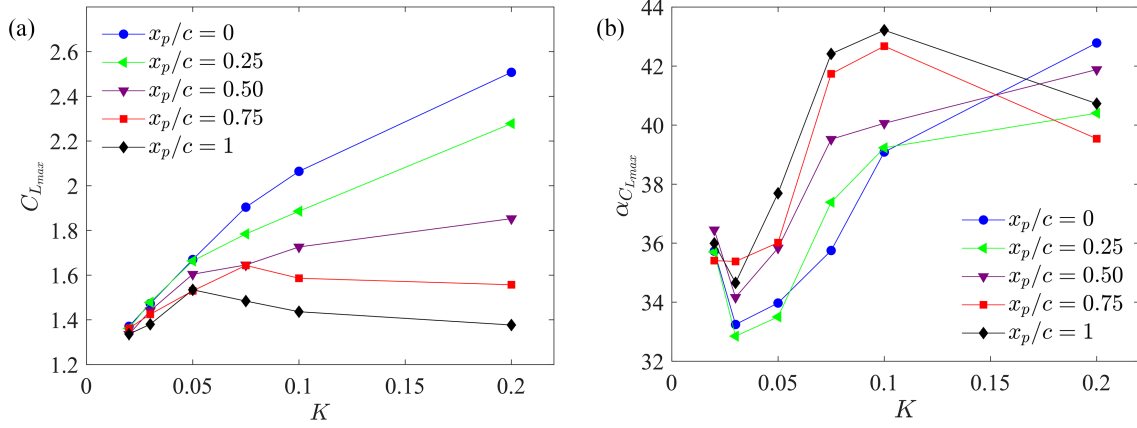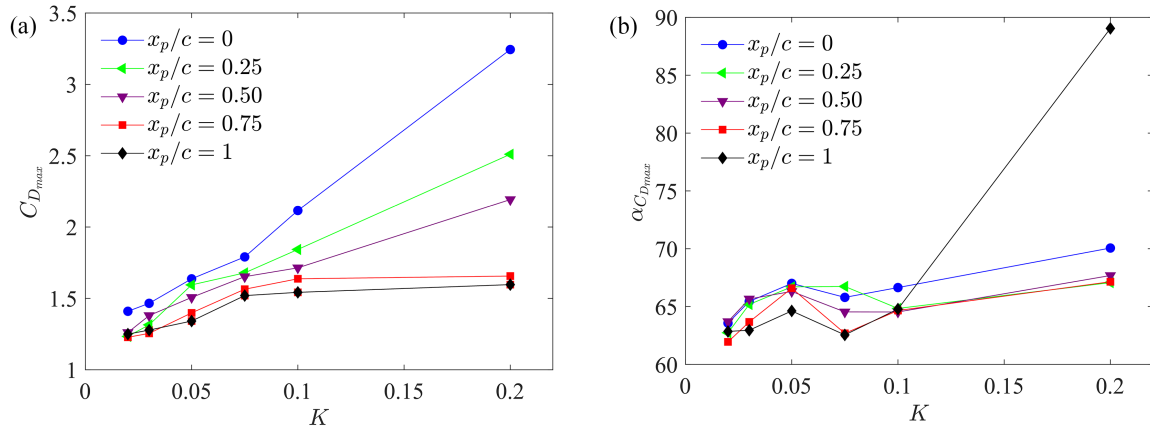
Figure 3.9: Trends of maximum drag coefficients (a), and associated pitch angles (b) with changing reduced pitch rates for different pivot locations $x_p/c = 0, 0.25, 0.50, 0.75, 1$

The pivot location effect on the moment coefficient is also an important parameter of interest in the aircraft design. In figure 3.10, a comprehensive analysis of the moment coefficient (C_M) for five distinct pivot axis locations (x_p/c) has been presented, while maintaining a constant reduced pitch rate of $K = 0.2$. Notably, each pivot point location yields a unique and discernible behavior. When the pivot location is at the leading edge ($x_p/c = 0$), C_M initially decreases from 0 at $\alpha = 0°$ to reach a minimum of -1.83 at $\alpha = 60°$, and then starts showing an upward trajectory as the pitch angle further increases till $90°$. Shifting the pivot location rearward to $x_p/c = 0.25$, causes C_M to monotonically decrease from 0 at $\alpha = 0°$ to -0.72 at $65°$, followed by a subsequent increase to -0.4 between $65°$ and $90°$. A notable change occurs when the pivot is at $x_p/c = 0.50$, as C_M changes to positive values. Initially, it increases with the pitch angle, eventually settling close to zero during the pitch motion from $0°$ to $90°$. At $x_p/c = 0.75$, we observe a consistent positive trend in C_M as the pitch angle increases. Remarkably, at $x_p/c = 1$, there is a distinctive negative drop in C_M at low pitch angle. This dip is attributed to a non-circulatory spike induced by the angular acceleration at the onset of pitch motion. Subsequently, C_M shows an upward trend, reaching a peak value of 0.78 at $\alpha = 56°$. It is worth noting that the data also reveal that the chord wise position of the center of normal force aligns closely with the mid-chord of the flat plate. That is why we don't observe a dynamic change in C_M with changing pitch angle at $x_p/c = 0.50$.
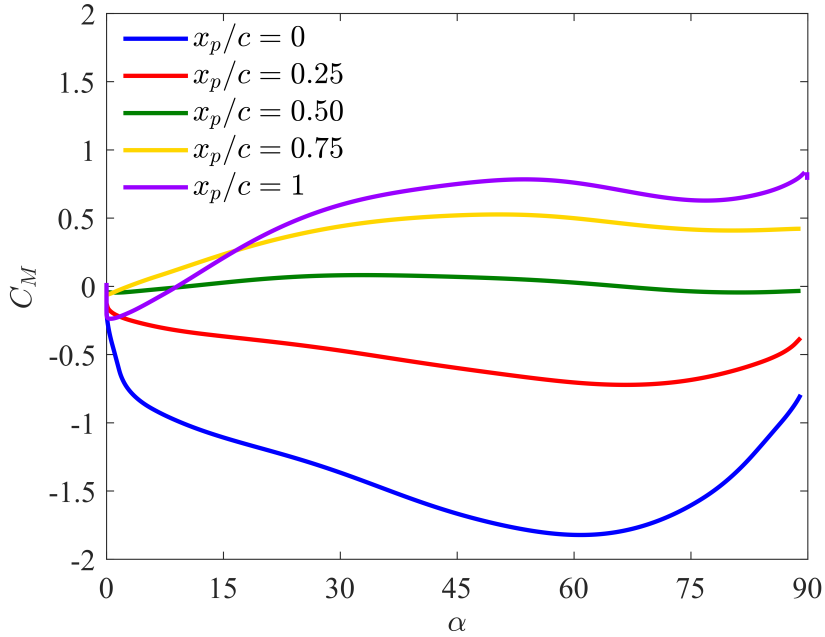
Figure 3.10: Moment coefficients comparing pitch pivot locations $x_p/c = 0$, 0.25, 0.50, 0.75, 1 at a constant reduced pitch rate $K = 0.2$

3.2.2 Flow field analysis

Figure 3.11 shows the vorticity plots for varying pitch pivot locations ($x_p/c = 0$, 0.25, 0.50, 0.75, 1) at pitch angles of $30°$, $45°$, $60°$ and $75°$, while maintaining a constant reduced pitch rate ($K = 0.2$). Each pitch pivot location exhibits distinctive flow field characteristics. Notably, the LEV in leading edge pitch pivot location has the highest amount of vorticity associated with it. Even at a $30°$ pitch angle, a well defined shear layer is formed at the leading edge, followed by vorticity roll-up into a leading-edge vortex, which subsequently entrains vorticity from the feeding shear layer. At higher pitch angles of $60°$ and $75°$, the LEV remains attached to the shear layer and progressively increases in size and strength. On the contrary, the aft pitch pivot locations show a consistent delay in pitch angle for the formation of LEV, which is accompanied with a gradual reduction in the amount of vorticity within the LEV and decrease in its size. For the trailing edge pivot location, a small LEV is barely noticeable at the leading edge, and at $75°$, its size is considerably smaller compared to the leading-edge pivot location. Although the pitching speed is constant across all pivot locations, variations in pitch pivot

location bring about substantial alterations in flow evolution with respect to the pitch angle for LEV formation, as well as its size and strength.
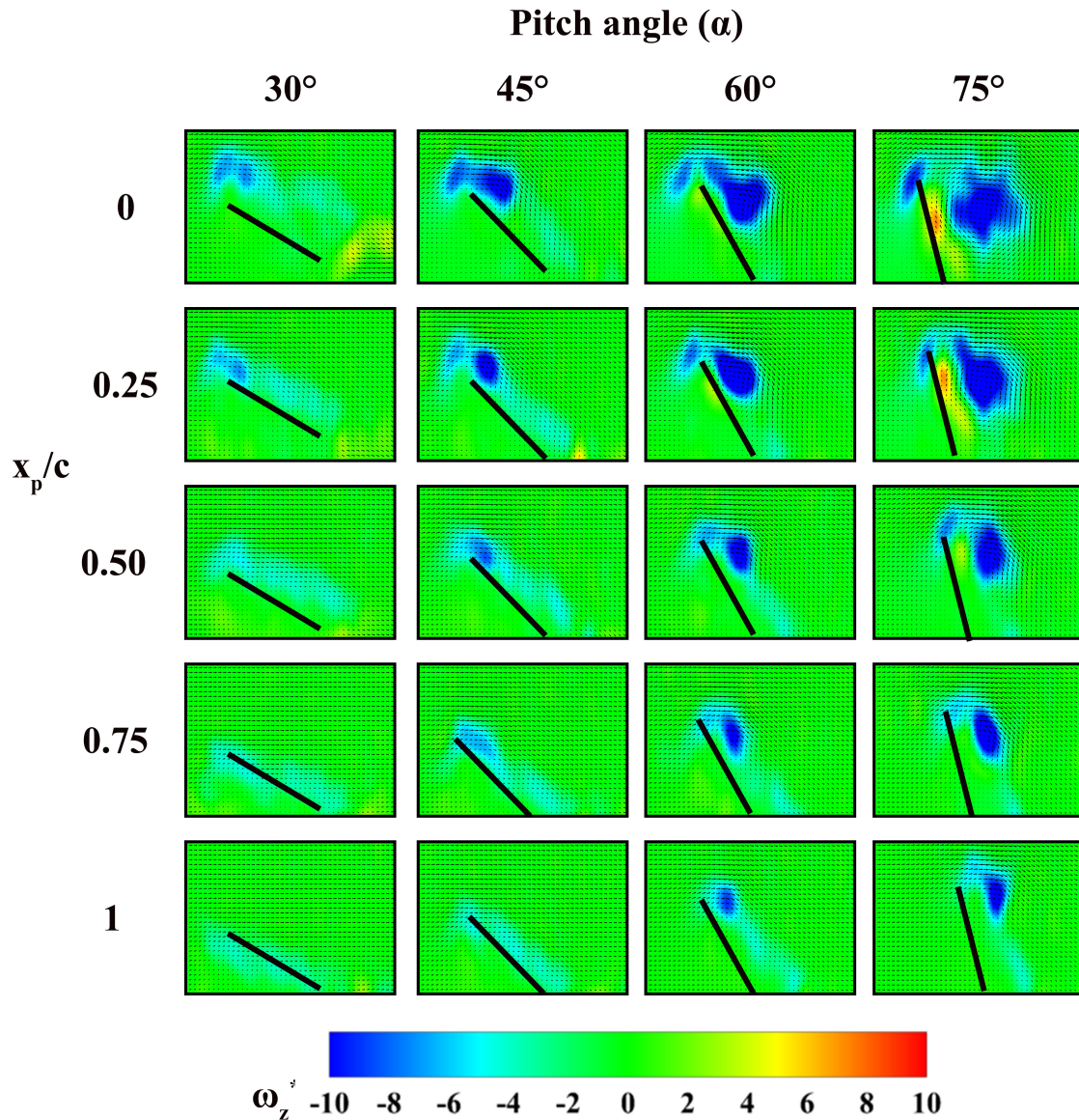
Figure 3.11: Vorticity plots comparing pitch pivot locations $x_p/c = 0$, 0.25, 0.50, 0.75, 1 at pitch angles of 30°, 45°, 60° and 75°, while maintaining a constant reduced pitch rate $K = 0.2$

The quantitative comparison of LEV circulation for $x_p/c = 0$, 0.25, 0.50, 0.75, 1 at a constant reduced pitch rate ($K = 0.2$) is shown in figure 3.12. In line with the vorticity plots shown in figure 3.11, we can clearly see a delay in LEV formation as the the pitch angle α for vortex detection keeps on getting higher as we progress from $x_p/c = 0$ to 1. At a specific α, the Γ_z^* for $x_p/c = 0$ is much higher than any of the aft pivot locations. Notably, LEV for $x_p/c = 1$

42

case is detected at much higher α and its Γ_z^* is lowest across all x_p/c cases considered. This also indicates that increasing K and shifting x_p/c towards the TE can effectively delay shear layer separation and LEV development. Based on the available data, no definitive comments regarding $\Gamma_{z_{max}}^*$ can be made as LEV is still attached to the shear layer at $90°$ pitch angle and Γ_z^* is still increasing in the negative direction for all the x_p/c cases considered.
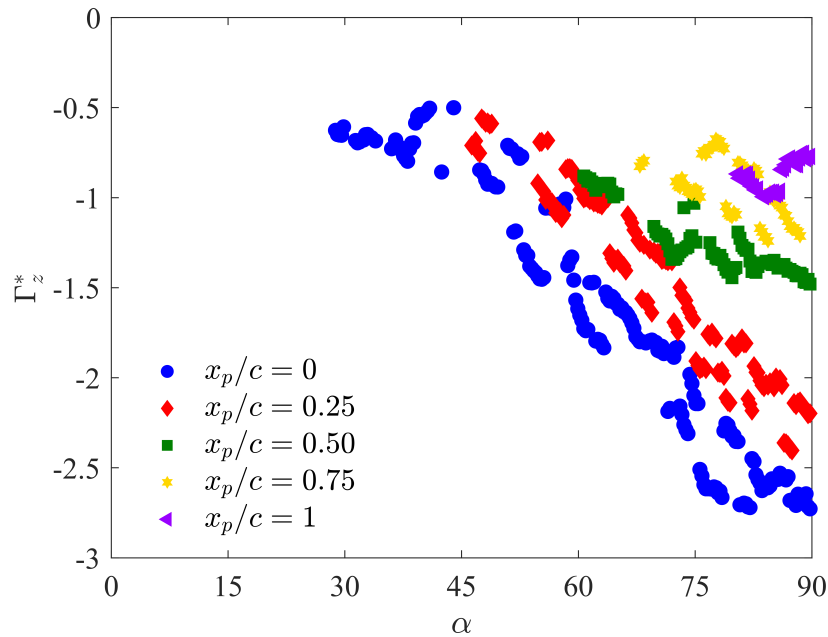
Figure 3.12: LEV circulation comparing pitch pivot locations $x_p/c = 0, 0.25, 0.50, 0.75, 1$ at a constant reduced pitch rate $K = 0.2$

3.3 Scaling analysis of C_L and C_D coefficients

3.3.1 Induced camber and trailing edge velocity based scaling

In the context of pitching motion, the relative motion of the trailing edge and leading edge generates a perturbation velocity distribution normal to the airfoil's chord line, resulting in the generation of a vortex sheet strength (γ_b) to maintain chord tangency. A pitch rate exerted about an axis induces a linear variation in normal perturbation velocity, resulting in a parabolic arc camber. Thus, pitching motion introduces a geometric rotation into the fluid, generating additional bound circulation, commonly described as the Magnus force [68], flow curvature effects

43

[72], or induced camber effect [67]. Such dynamics contribute significantly to the overall lift or drag force generated on the surface on wing.

For the attached flow conditions, where the chord line represents a streamline of the flow, fluid particles follow the path of induced camber. The curvature of the induced camber, specifically aft of the pitch pivot, directly relates to the trailing edge velocity (u_{TE}). The trailing edge velocity governs the direction and velocity of fluid particles departing the the chord line, while satisfying the Kutta condition and maintaining flow tangency. The magnitude of trailing edge velocity in turn depends on the magnitude of reduced pitch rate K and the distance of pitch pivot location from the trailing edge.

In the case of pitch-up motion and leading-edge pitch pivot location, the flow will be accelerated and deflected downward while leaving the chord due to pitch induced camber. Therefore, the fluid particle will experience a force in the downward direction. An equal and opposite force will be experienced by the airfoil in the upward direction which manifests itself as an additional lift due to pitching motion of airfoil and its magnitude is proportional to the trailing edge velocity of the airfoil. In the case of mid-chord pivot location, the flow will again be deflected downward while leaving the chord. However, as the trailing edge velocity is lower as compared to the leading-edge pitch pivot case, we would expect less additional lift due to induced camber effect. For the trailing-edge pivot location, the flow will not be deflected downward as the trailing edge velocity is zero. The flow would leave tangent to the chord line and we should not observe additional lift due to pitching motion. This phenomenon can be explained satisfactorily by the control volume analysis performed for three pivot locations as shown in figure 3.13.

Applying the momentum equation to the Control Volume containing the virtual cambered airfoil:

$$\frac{d}{dt} \iiint_{\text{cv}} \rho \mathbf{u} \, dV + \iint_{\text{cs}} \mathbf{u}(\rho \mathbf{u} \cdot \mathbf{n}) \, dA = \sum \mathbf{F} \tag{3.3}$$

Neglecting unsteady effects ($d/dt \to 0$)

$$\iint_{\text{cs}} \mathbf{u} \cdot (\rho \mathbf{u} \cdot \mathbf{n}) \, dA = \sum \mathbf{F} \tag{3.4}$$

As there is no mass flux through control surface 2 and 4. Also, $A_1 = A_3 = A$. Therefore,
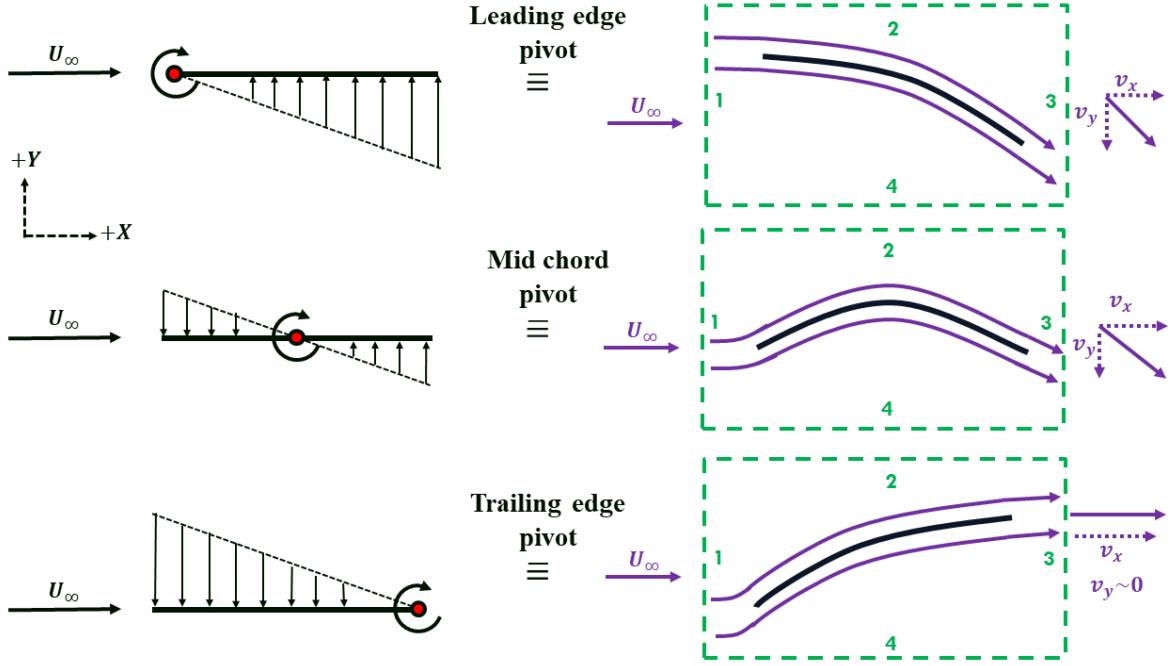
Figure 3.13: Control volume analysis for different pitch pivot locations

$$F_y = -\rho A v_y v_x \qquad\qquad F_x = -\rho A(U_\infty^2 - v_x^2) \qquad (3.5)$$

F_x and F_y are the forces experienced by the fluid particle. Therefore, an equal and opposite force will be experienced by the airfoil in terms of lift and drag, respectively.

$$L = \rho A v_y v_x \qquad\qquad D = \rho A(U_\infty^2 - v_x^2) \qquad (3.6)$$

From the control volume analysis, we know that the magnitude of additional lift or drag due to camber would depend on the components v_x and v_y of the resultant flow due to induced camber which in turn depends on the trailing edge velocity, u_{TE}. For the present scaling analysis, to normalize for any curvature effects due to pitching motion, we add the trailing-edge velocity to the freestream velocity to define a characteristic velocity (U^*) and use that in the non-dimensionalization of the lift and drag forces.

$$U^* = U_\infty + u_{TE} \qquad (3.7)$$

$$C_L^* = \frac{2L}{\rho U^{*2} A} \qquad\qquad C_D^* = \frac{2D}{\rho U^{*2} A} \qquad (3.8)$$

45

We can now define a kinematic relation to write the velocity at the trailing edge of the airfoil in terms of K and x_p/c as:

$$u_{TE} = x_p \cdot \dot{\alpha} = \frac{2U_\infty K(c - x_p)}{c} \tag{3.9}$$

For leading-edge pivot location, $u_{TE} = 2U_\infty K$, for mid-chord pivot, $u_{TE} = U_\infty K$ and for trailing edge, $u_{TE} = 0$. Therefore, we can say that additional lift and drag due to induced camber for the leading edge pivot location is the highest and it diminishes to zero once we start moving toward the trailing edge pivot location. Figures 3.14 and 3.15 show the lift and drag coefficient plot for five different pitch pivot locations and varying reduced pitch rates when we use the characteristic velocity for non-dimensionalization of lift and drag forces. In contrast to figures 3.6 and 3.7, we observe a good collapse in both scaled lift and drag curves for all pivot location cases at a constant reduced pitch rate. This data collapse confirms that u_{TE} is the driving variable that determines the unsteady response.

The above explanation for the collapse of the data on the y-axis for all pitch rates and pivot locations is based on the assumption of an attached flow condition. However, this justification approximates reasonably well for the separated flows as well in which there is an evolving LEV at the leading edge of the airfoil. The rotational region created by the LEV effectively pulls the fluid back onto the chord, and the fluid leaves the airfoil along chord line. In the case of separated flow, since the bound circulation is minimal, we would expect the LEV strength to increase proportional to u_{TE} as it would result in faster flow speeds and increased vorticity brought about by the rapid rotation.

In our study, we also explored the possibility of using the maximum value of $\left| \overline{U_\infty} + \overline{u_{TE}} \right|$ as a characteristic velocity for non-dimensionalizing the forces. However, we observed that this choice did not lead to a satisfactory collapse of the aerodynamic loads data across various pitch rates. We also examined scaling relations involving velocities at the leading edge (u_{LE}), mid-chord (u_{MC}), and other pivot locations to assess data collapse, but none yielded the desired result. These findings imply that the hydrodynamic forces acting on the plate arise from the interaction between the free stream velocity and the trailing edge velocity while undergoing pitching motion.
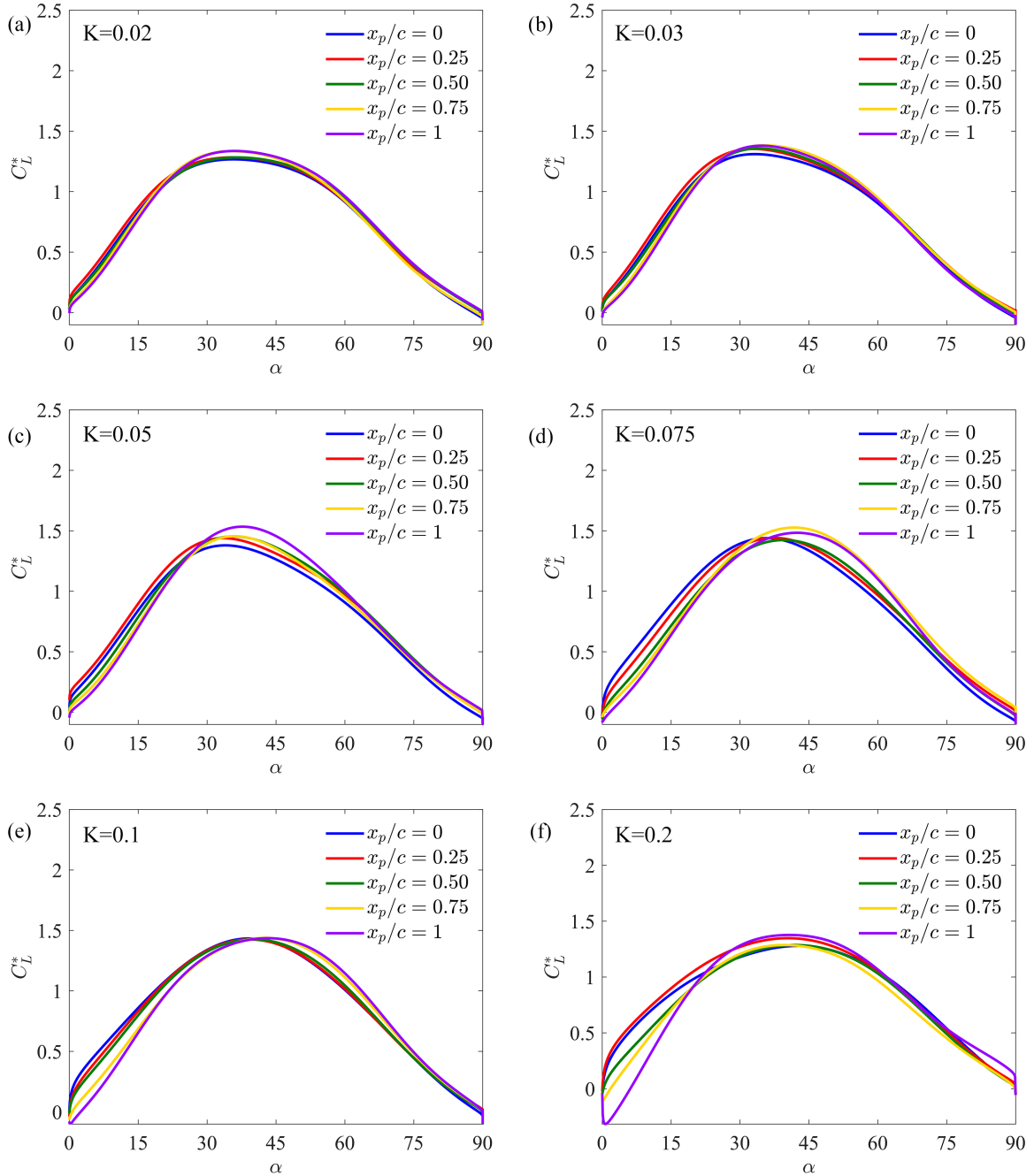
Figure 3.14: Modified lift coefficients comparing pivot locations $x_p/c = 0, 0.25, 0.50, 0.75, 1$ at a constant reduced pitch rate $K = 0.02$ (a), 0.03 (b), 0.05 (c), 0.075 (d), 0.1 (e) and 0.2 (f)

Figure 3.15: Modified drag coefficients comparing pivot locations $x_p/c = 0$, 0.25, 0.50, 0.75, 1 at a constant reduced pitch rate $K = 0.02$ (a), 0.03 (b), 0.05 (c), 0.075 (d), 0.1 (e) and 0.2 (f)
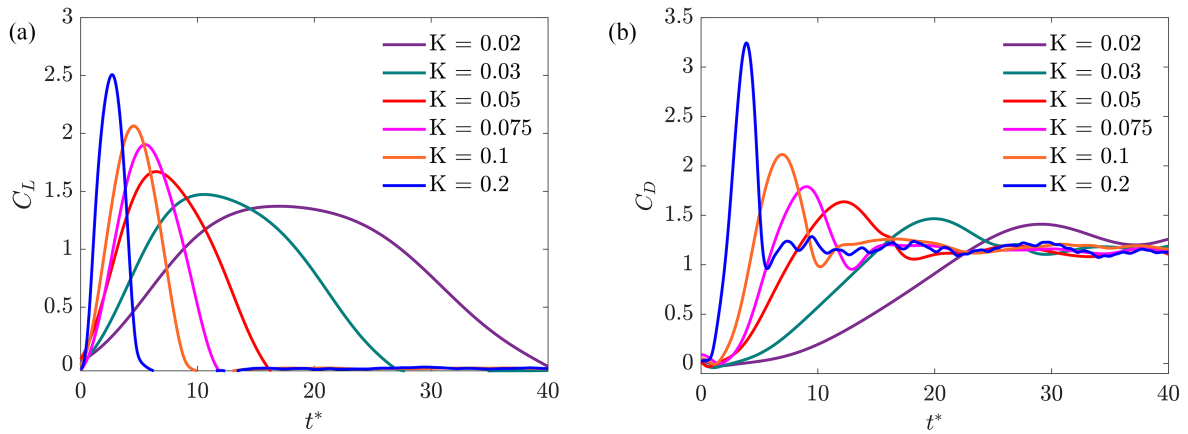
Figure 3.16: Lift (a) and drag (b) coefficients comparing reduced pitch rates $K = 0.02, 0.03,$ 0.05, 0.075, 0.1, 0.2 at a constant pitch pivot location $x_p/c = 0$, and plotted against the non-dimensional convective time t^*

3.3.2 Dynamic convective time shift based scaling

It is also possible to analyze the aerodynamic loads data for different pitch rates and pitch pivot location in terms of non-dimensional convective time which is referred to the number of chord lengths traversed by the free stream while reaching a specified plate incidence angle, $t^* = tU_{tip}/c$. This would help us to investigate the forces at a constant rotation angle / convective time for different cases as the rotation speed is constant for a specific Reynolds number. The effect of changing the reduced pitch rates ($K = 0.02$–0.2) for a fixed pivot location ($x_p/c = 0$) on aerodynamic force coefficients C_L and C_D is shown in figure 3.16. Here, C_L and C_D are plotted against the convective time 't^*' for different reduced pitch rates. It can be clearly seen from the plots that by changing reduced pitch rate from 0.02 - 0.2, the peak values of C_L and C_D are higher for higher K and $C_{L_{max}}$ and $C_{D_{max}}$ shift towards at an earlier t^* due to higher pitching speeds associated with higher reduced pitch rates. This gives us an idea regarding the magnitude of pitching speed relative to the rotation rate and also compliments the different reduced pitch rate regimes as discussed in previous section.

In contrast, the plots of aerodynamic forces in terms of C_L and C_D for a constant reduced pitch rate ($K = 0.075$) and changing pivot locations from leading edge towards trailing edge has been shown is figure 3.17. As a general trend, we can observe that by changing pivot
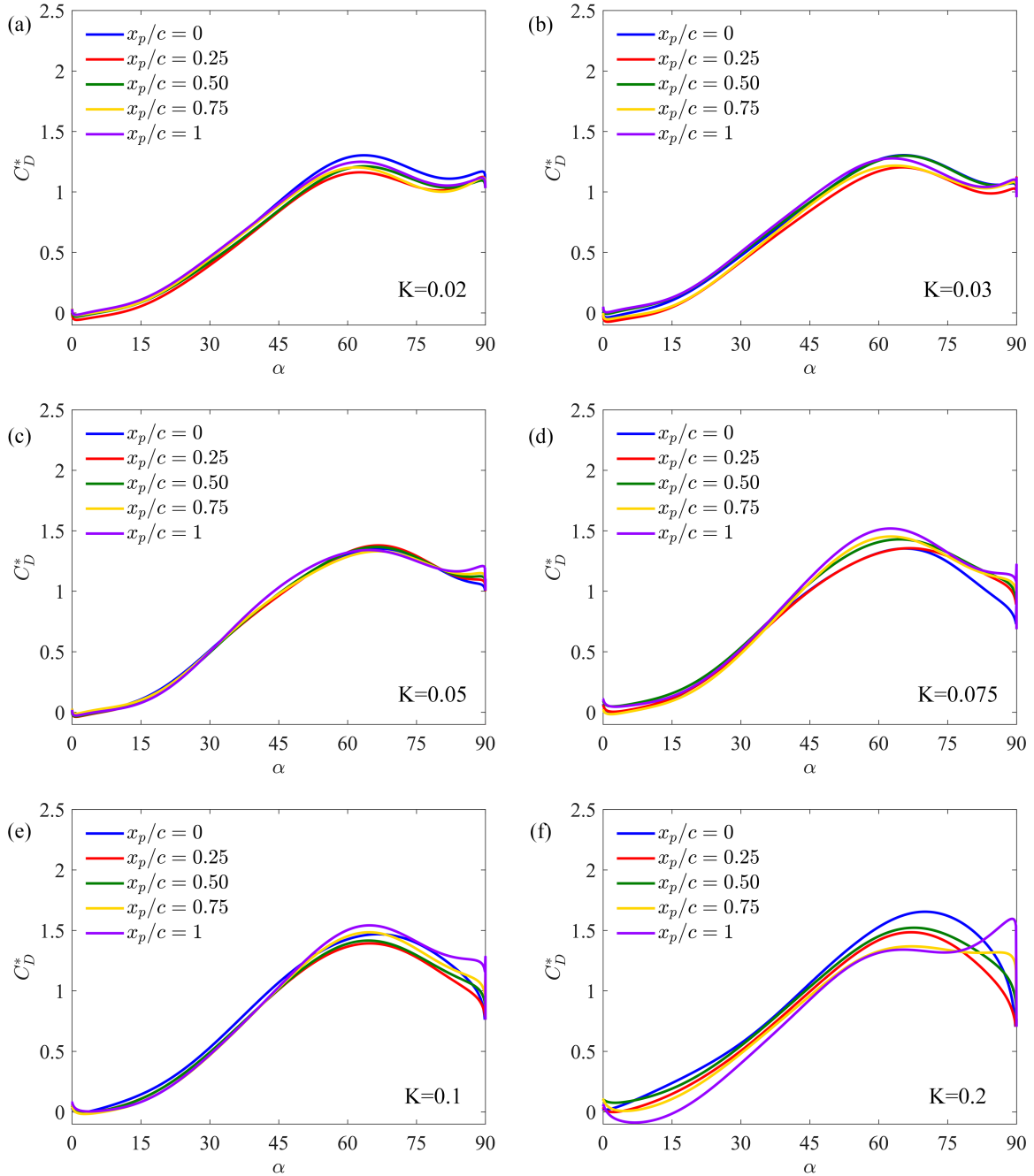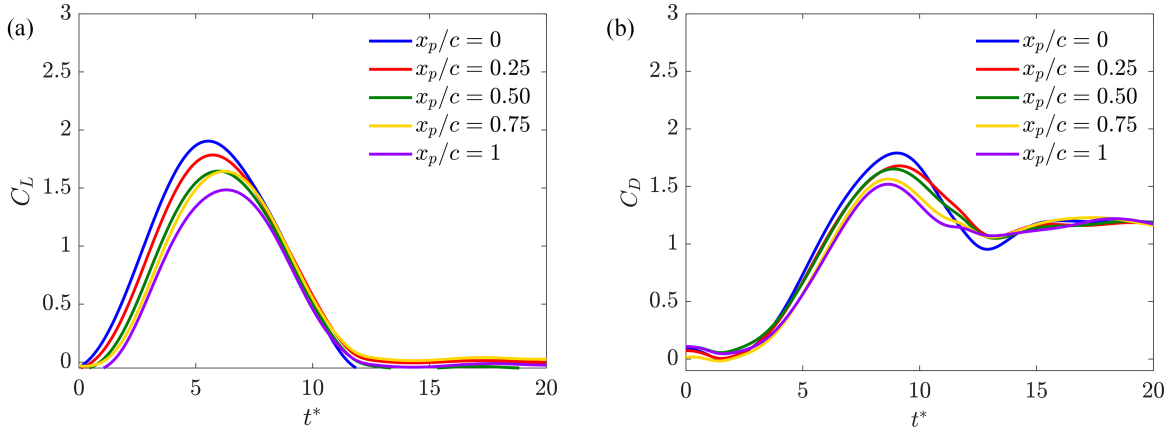
Figure 3.17: Lift (a) and drag (b) coefficients comparing pitch pivot locations $x_p/c = 0$, 0.25, 0.50, 0.75, 1 at a constant reduced pitch rate $K = 0.075$, and plotted against the non-dimensional convective time t^*

locations $x_p/c = 0 - 1$; peak values of C_L and C_D for aft pivot locations occur at later t^* and their corresponding peaks are lower as we move from leading edge to trailing edge pivot location. This means that there is a delay in convective time associated with different pivot locations that shifts the $C_{L_{max}}$ values to a later t^* for aft pivot locations.

The summary non-dimensional convective time t^* at which the maximum lift and drag coefficients are attained is plotted in figure 3.18. The effect of changing reduced pitch rate ($K = 0.02$–0.2) for five pivot locations ($x_p/c = 0$, 0.25, 0.50, 0.75 and 1) results in $C_{L_{max}}$ values occurring at an earlier t^* for higher reduced pitch rates. For the lowest reduced pitch rate ($K = 0.02$) considered in this study, t^* for $C_{L_{max}}$ is 16 which means that wing rotates almost 16 chord lengths during its dynamic pitch motion to reach the maximum C_L and rotational motion has the dominance in this low reduced pitch rate regime. Whereas, for $K = 0.2$, $t^*_{C_{L_{max}}} = 2$ for all pivot locations which gives an idea that pitching speed is higher and it has a significant contribution in determining the overall unsteady aerodynamic response of the system. Figure 3.18 also shows that there are slight variations in $t^*_{C_{L_{max}}}$ among different pivot locations at a constant reduced pitch rate K. As a general trend, we can see that for a constant reduced pitch rate K, $t^*_{C_{L_{max}}}$ is lower for $x_p/c = 0$ as compared to $x_p/c = 1$. This difference in t^* can be attributed to the convective time shift for different pivot locations. $K = 0.2$ does not conform to this trend and $C_{L_{max}}$ for all pivot locations occur at the same non-dimensional convective time

50
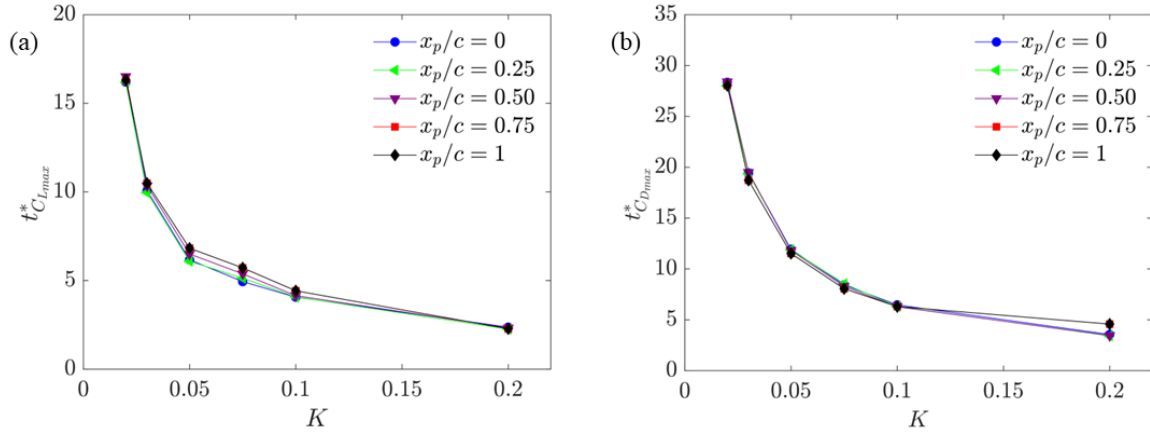
Figure 3.18: Trends of non-dimensional convective time t^* for maximum lift (a) and drag (b) coefficients with changing reduced pitch rates for different pitch pivot locations $x_p/c = 0, 0.25, 0.50, 0.75, 1$

t^* in this case. Trends for $t^*_{C_{D_{max}}}$ are the same as that for $t^*_{C_{L_{max}}}$ except that the t^* value for $C_{D_{max}}$ are much higher as compared to $C_{L_{max}}$. This because of the fact the maximum value of drag coefficient occurs late in the pitching cycle when the plate normal force starts contributing more towards the drag direction.

Previously, Granlund et al. [24] proposed a convective time shift strategy for translating pitching flat plates. That methodology was based on the pitch pivot location to cater for time shift of lift and drag trends. For example, for $x_p/c = 0.50$, a constant time shift of $0.5t^*$ was applied to the x-axis with respect to the $x_p/c = 0$ case. Similarly, for $x_p/c = 1$, convective time shift of $1t^*$ was implemented. However, it only considered the effect of pitch pivot location x_p/c and t^* shift was held constant for a specific pivot location during the pitching motion. Here, we propose a new methodology that takes into account both the effect of reduced pitch rate K as well as pitch pivot location x_p/c. Furthermore, the convective time shift is also constantly varying during the dynamic pitch motion from $0 \rightarrow 90°$. This methodology is based on the induced flow at the leading edge of flat plate. Pitching motion of the flat plate results in an induced velocity (v_p) at the leading edge, the magnitude of which depends on the pitching speed and the distance between the leading edge and the pitch pivot location ($v_p = x_p \cdot \dot{\alpha}$). This locally induced flow (v_p) will act perpendicular to the wing surface and will result in an induced angle α_{ind} between the local relative flow and the direction of freestream velocity U_∞.
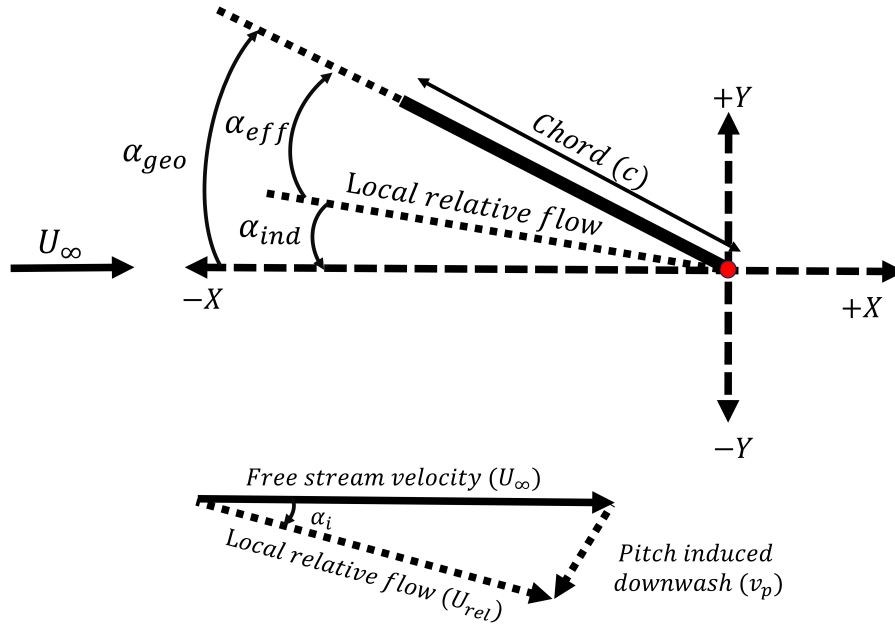
Figure 3.19: Effective angle of attack (α_{eff}) at the plate leading edge

Therefore, with the superposition of additional local speed v_p and freestream U_∞, the effective of attack α_{eff} is reduced for the flat plate as compared to geometric angle of attack α_{geo}; which in this case, will be the angle between the chord line and the direction of the local relative flow as shown in figure 3.19. The magnitude of α_{eff} can be found by equations given below:-

$$\alpha_{eff}(t) = \alpha_{geo}(t) + \alpha_{ind}(t) \tag{3.10}$$

where,

$$\alpha_{ind}(t) = \tan^{-1}\left(\frac{v_{p_y}(t)}{v_{p_x}(t) + U_\infty}\right) \tag{3.11}$$

The induced velocity v_p at the leading edge can be written in terms of reduced pitch rate K and pitch pivot location x_p/c as:

$$v_p = 2U_\infty K x_p/c \tag{3.12}$$

From figure 3.20, we can see that vertical component of velocity v_{p_y} is $v_p \cdot \cos\alpha$ and horizontal velocity component can be written as $v_{p_x} = v_p \cdot \sin\alpha$. Based on these results, the effective angle of attack α_{eff} will change constantly during the pitching motion from $0 - 90°$
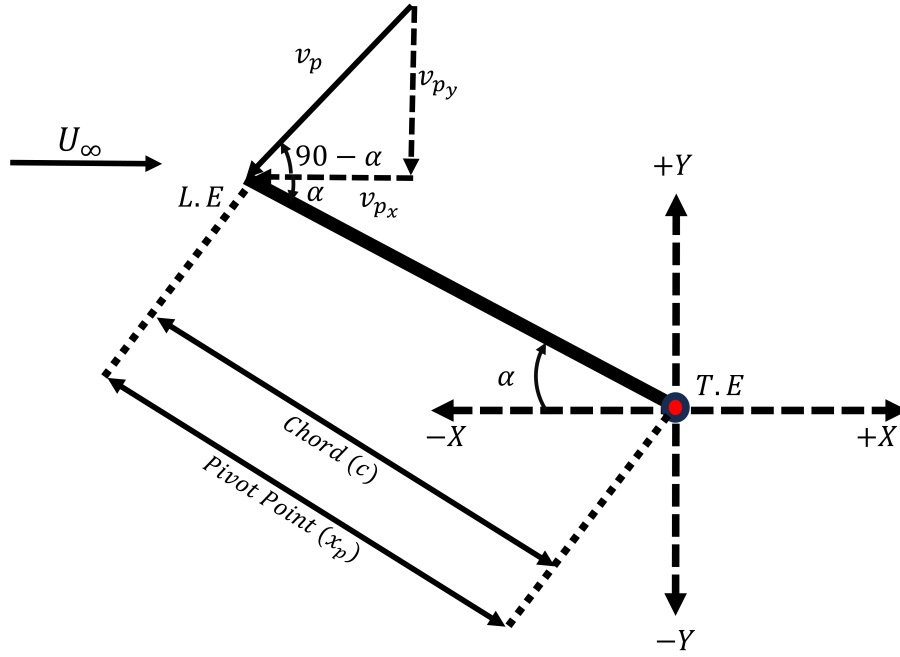
Figure 3.20: Horizontal (v_{p_x}) and vertical (v_{p_y}) velocity components of the induced flow (v_p) at the plate leading edge

and its magnitude will depend on the instantaneous α_{geo}, K and x_p/c. Now the final expression for α_{eff} can be written as:

$$\alpha_{eff}(t) = \alpha_{geo}(t) + \tan^{-1}\left[\frac{(2U_\infty K x_p/c) \cdot \cos\alpha(t)}{(2U_\infty K x_p/c) \cdot \sin\alpha(t) + U_\infty}\right] \tag{3.13}$$

Conventionally, convective time (t_c) is defined as the number of chord lengths (distance from leading edge towards the trailing edge) travelled by a fluid particle while travelling at a speed of U_∞. Now, as a result of the induced angle of attack α_{ind}, the fluid particle will move at an angle of α_{eff} instead of α_{geo} (which is the direction of the chord); and its effective displacement along the chord will be reduced. Knowing the pitch speed ($\dot{\alpha}$) and α_{ind} at that instant in time, we can compute the induced time (t_{ind}) for the particle to cover the remaining distance $(c - x)$ along the chord while still travelling at a speed of U_∞.

$$t_{ind} = \frac{c - x}{U_\infty} = \frac{\alpha_{ind}}{\dot{\alpha}} \tag{3.14}$$

Finally, the effective time (t_{eff}) for the actual particle displacement along the chord can be defined as a function of conventional time (t_c) and induced time (t_{ind}) as follows:

$$t_{eff} = t_c + t_{ind} \tag{3.15}$$

The non-dimensional effective convective time t^*_{eff} for the particle displacement at any instant (t) can be written as:

$$t^*_{eff}(t) = t^*(t) + t^*_{ind}(t) \tag{3.16}$$

Simplifying for $t^*_{ind}(t)$ gives:

$$t^*_{ind}(t) = \frac{t_{ind}U_\infty}{c} = \frac{\alpha_{ind}(t)}{2K} \tag{3.17}$$

The final equation for t^*_{eff} that includes all the combined effects is as follows:

$$t^*_{eff}(t) = t^*(t) + \frac{1}{2K}\tan^{-1}\left[\frac{(2U_\infty K x_p/c)\cdot\cos\alpha(t)}{(2U_\infty K x_p/c)\cdot\sin\alpha(t) + U_\infty}\right] \tag{3.18}$$

The lift and drag curves for the three pitch pivot locations ($x_p/c = 0, 0.50, 1$) and $K = 0.02 - 0.2$ are plotted in figure 3.21, which shows the results for C_L and C_D when plotted against the conventional convective time t^* (figure 3.21 (a),(d)), after applying a constant convective time shift based on pitch pivot location (figure 3.21 (b),(e)) and after applying dynamic convective time shift (figure 3.21 (c),(f)). As the convective time shift is applied, the peak values of lift (C_L) and drag (C_D) coefficients are shifted towards left and occur at an earlier t^* for aft pivot locations for both the convective time shift methodologies. Furthermore, the C_L and C_D curves for different pivot locations at a constant K collapse during the start of motion but we start seeing a diversion in trends during later part of pitching motion. For the convective time shift based on pivot location (figure 3.21 (b),(e)), the t^* shifting results in collapse during the start of motion but it causes a significant mismatch between different curves during the later part. However, for the dynamic convective time shift case, t^*_{ind} will be maximum during the start of motion at $0°$ and it will continuously decrease during the pitching cycle. At $90°$, α_{ind} will be zero and subsequently t^*_{ind} will also reduce to zero as the wing approaches $90°$. Henceforth, t^*_{eff} will approach to convectional t^* at the end of pitching cycle. That's why the curves in figure 3.21 (c) and (f) are collapsed better during most part of pitching motion as compared to figure 3.21 (b) and (e). The initial rise in C_L and C_D is coincident for all the cases after applying dynamic convective time shift and for $K = 0.02, 0.03, 0.05$ and 0.075, C_L peaks also occur essentially at the same t^*_{eff}. For $K = 0.1, 0.2$; the initial rise is same for all pivot locations but the difference in C_L peaks is much greater and also the drop in C_L starts occurring

54
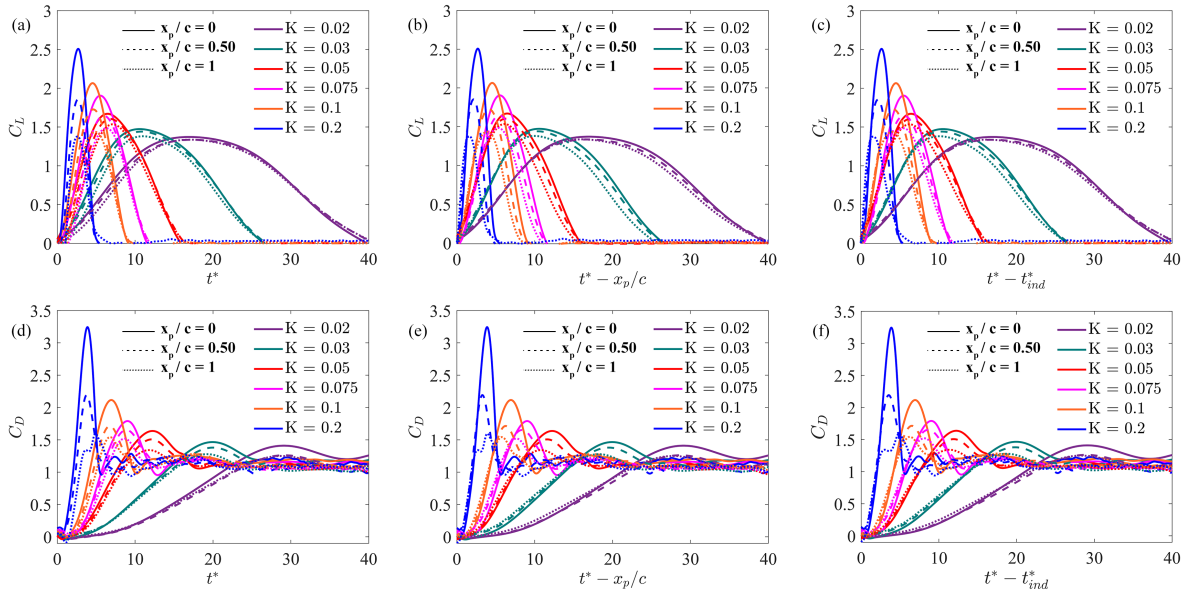
Figure 3.21: Lift and drag coefficients comparing reduced pitch rates $K = 0.02, 0.03, 0.05,$ 0.075, 0.1, 0.2 for different pitch pivot locations ($x_p/c = 0, 0.50, 1$), and plotted against the conventional convective time ((a),(d)), convective time shift based on pitch pivot location ((b),(e)) and dynamic convective time ((c),(f))

at an earlier t^* as we start moving from $x_p/c = 0.50 \rightarrow 1$ with respect to the $x_p/c = 0$ case. Same trends can be observed in C_D curves as well. The deviation in trends for $K = 0.1 - 0.2$ may be attributed to significant variations in flow field for higher reduced pitch rates K such that convective time shifting based on induced flow at the leading edge is successful only during initial phase of pitching motion and the peak C_L and C_D values and their corresponding convective times t^* do not collapse on both the x and y-axis.

3.4   Effect of Reynolds number

Although previous research pertaining to the effect of Reynolds number on pitching wings primarily focused on the LEV separation mechanisms and establishing key parameters for predicting LEV initiation; the influence of Reynolds number on force generation and LEV development has yielded inconsistent findings. Notably, various studies [31, 32, 39, 37, 38, 34] have suggested an insensitivity in both aerodynamic loading and flow structure with respect to changes in Reynolds number. In contrast, some other investigations [33, 35, 36] indicated that an increase in the Reynolds number corresponds to an increase in aerodynamic loads and

noticeable changes in flow structures. Here, we address similar questions in the specific context of a rotating and pitching flat plate, aiming to provide reasonable justifications for the observed trends in aerodynamic loads and LEV dynamics.

3.4.1 Aerodynamic loads analysis

The comparison of lift and drag coefficients at Reynolds numbers of 5,000 and 10,000 for two distinct reduced pitch rates K of 0.02 and 0.2 is shown in Figure 3.22 (a) and (b), while the pitch pivot location has been fixed at the leading edge ($x_p/c = 0$) of the flat plate. Notably, the lower Reynolds number consistently yields higher lift and drag coefficients across various pitch angles. Although the trends in the curves for both Reynolds numbers share similarities, the slopes of C_L and C_D are significantly lower for $Re = 10,000$ compared to $Re = 5,000$. At $K = 0.2$, the maximum lift coefficient ($C_{L_{max}}$) is 2.5 for $Re = 5,000$ and 1.87 for $Re = 10,000$, while at $K = 0.02$, it is 1.37 for $Re = 5,000$ and 0.94 for $Re = 10,000$. Similarly, the maximum drag coefficient ($C_{D_{max}}$) at $K = 0.2$ shows a decrease from 3.23 at $Re = 5,000$ to 2.54 at $Re = 10,000$, while at $K = 0.02$, the values change from 1.41 to 1.28 for the respective Reynolds numbers. Slight variations can also be observed in terms of the pitch angles corresponding to the maximum C_L and C_D values. Additionally, the non-circulatory spike is less pronounced at $K = 0.2$ in the case of $Re = 10,000$ due to the maximum acceleration limit of servo motor, which results in a reduced acceleration for this reduced pitch rate, a lower σ value in hyperbolic cosine function and subsequently a smoother pitch profile.

At the Reynolds numbers of the present investigation, it can be safely assumed that the predominant aerodynamic force acting on the wing comes from the pressure differential between the upper and lower surfaces of the flat plate. Upon non-dimensionalizing the aerodynamic lift and drag forces, the normalization is achieved with respect to the free stream dynamic pressure, area and chord length. Changing Reynolds number from $Re = 5,000$ to 10,000 results in a doubling of the tip velocity, leading to a four-fold increase in dynamic pressure. However, for equivalent or higher aerodynamic loads at the higher Reynolds number, the pressure difference between the top and bottom surfaces of the flat plate must increase by a proportionate amount. The observed lower values of C_L and C_D at higher Reynolds numbers can be attributed to
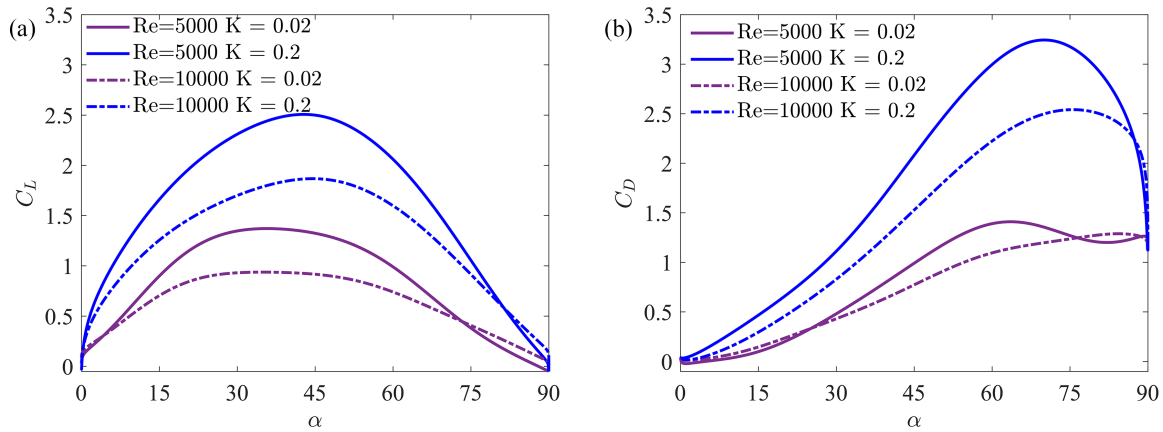
Figure 3.22: Comparison of lift (a) and drag (b) coefficients at $Re = 5,000$ and $10,000$ for $K = 0.02$ and 0.2, while keeping the pitch pivot location fixed at $x_p/c = 0$

the fact that, despite the substantial increase in dynamic pressure for $Re = 10,000$, the static pressure difference between the top and bottom surfaces of the flat plate does not increase by the same magnitude. Consequently, the difference in pressure difference is responsible for the lower C_L and C_D values at $Re = 10,000$ compared to $Re = 5,000$.

We can also analyze the aerodynamic force coefficients at $Re = 5,000$ and $10,000$ while maintaining a constant reduced pitch rate ($K = 0.075$) and varying the pitch pivot location from $x_p/c = 0$ to 1. This comparison is illustrated in figure 3.23 (a) and (b). Similar to 3.22, changing Reynolds number from $Re = 5,000$ to $10,000$ results in a noticeable reduction in both aerodynamic lift and drag coefficients. At $x_p/c = 0$, $C_{L_{max}}$ decreases from 1.9 for $Re = 5,000$ to 1.46 for $Re = 10,000$, and at $x_p/c = 1$, it declines from 1.48 to 1.06 for the respective Reynolds numbers. Similarly, $C_{D_{max}}$ at $x_p/c = 0$ decreases from 1.79 at $Re = 5,000$ to 1.48 at $Re = 10,000$, and at $x_p/c = 1$, the values shift from 1.52 to 1.06 for the corresponding Reynolds numbers. Consistent trends observed in the aerodynamic force coefficients underscore the profound impact of Reynolds number on the aerodynamic performance of the system. This noticeable trend stands in contrast to previous studies that suggested insensitivity in aerodynamic loads while changing the Reynolds number. These observations emphasize the
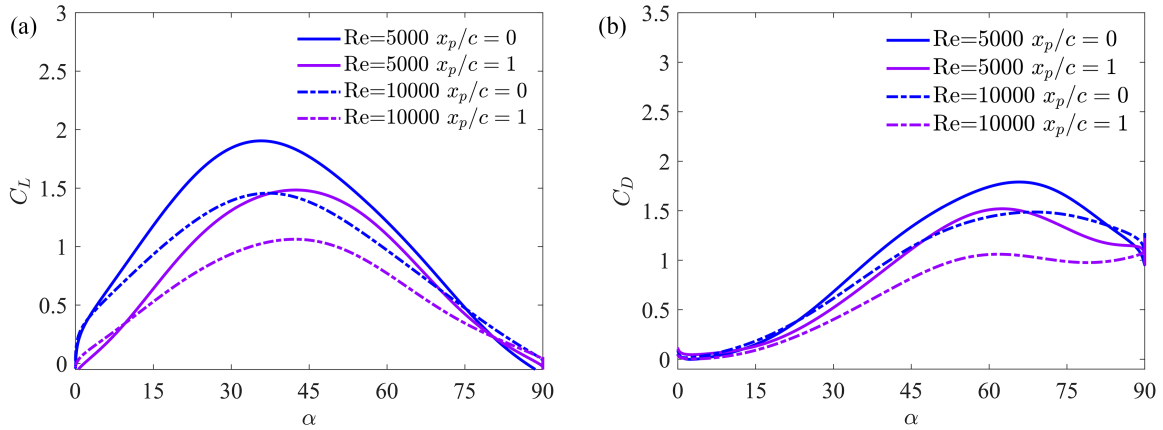
Figure 3.23: Comparison of lift (a) and drag (b) coefficients at $Re = 5,000$ and $10,000$ for $x_p/c = 0$ and 1, while maintaining a constant reduced pitch rate $K = 0.075$

need to further explore the intricate interplay between Reynolds number and flow characteristics to get better insights into the underlying mechanisms responsible for the lower aerodynamic performance of the system at the higher Reynolds number considered.

3.4.2   Flow field analysis

The vorticity plots depicted in figure 3.24 show the flow field comparison between Reynolds numbers of 5,000 and 10,000, for leading-edge pivot location ($x_p/c = 0$) and maintaining a constant reduced pitch rate ($K = 0.075$). Notably, the LEV size is considerably smaller for $Re = 10,000$ in comparison to $Re = 5,000$. This discrepancy in size can be associated to a lower influx of vorticity being fed into the LEV for the $Re = 10,000$ case. Consequently, the smaller vortex size and strength leads to a reduced suction pressure on the top surface of flat plate. The consequence of this phenomenon can be directly correlated to the aerodynamic loads in terms of C_L and C_D as well. Specifically, the smaller and lower vorticity laden LEV at $Re = 10,000$ results in lower values of lift coefficient (C_L) and drag coefficient (C_D) compared to the $Re = 5,000$ case. This intricate interplay between vortex dynamics, suction pressure, and aerodynamic loads provide valuable insights for analysing the influence of changing Reynolds number on the aerodynamic performance of the system.
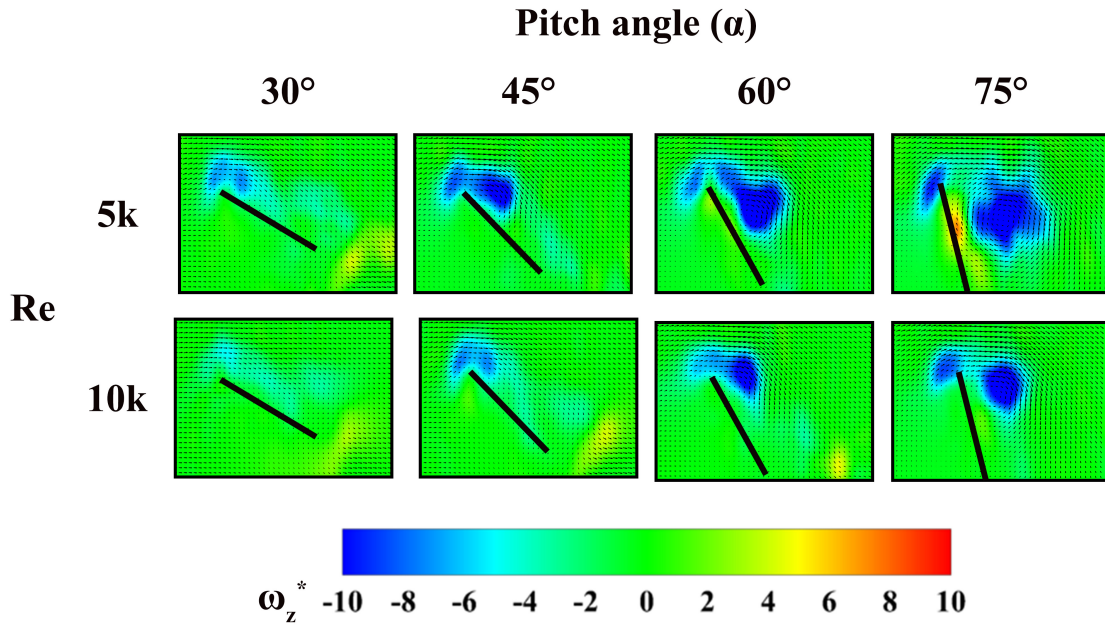
Pitch angle (α)

Figure 3.24: Comparison of vorticity plots for $Re = 5,000$ and $10,000$ at pitch angles of $30°$, $45°$, $60°$ and $75°$ for $x_p/c = 0$ and $K = 0.2$

The comparative analysis of LEV circulation at Reynolds numbers of 5,000 and 10,000, for $x_p/c = 0$ and $K = 0.075$, is shown in figure 3.25. Remarkably, the pitch angle for LEV formation remains consistent across the two Reynolds numbers. The similarity in pitch angles suggests that the fundamental mechanisms driving LEV formation remain consistent across the two Reynolds numbers. However, a notable disparity arises in the growth rate of LEV circulation for both cases. Specifically, $Re = 10000$, shows a consistent trend of lower LEV circulation growth rate with increasing pitch angles. This observed discrepancy has profound implications, suggesting a reduction in the vorticity influx and consequently, a decrease in the suction pressure developing on the top of the flat plate. This attenuation of suction pressure can be directly related to the aerodynamic loads experienced by the flat plate as the coefficients of lift (C_L) and drag (C_D) at $Re = 10,000$ are substantially lower than those observed at $Re = 5,000$. This detailed analysis underscores the importance of Reynolds number in shaping the aerodynamic characteristics of the flow, shedding light on the complex interplay between fluid dynamics and the resulting forces acting on the flat plate.
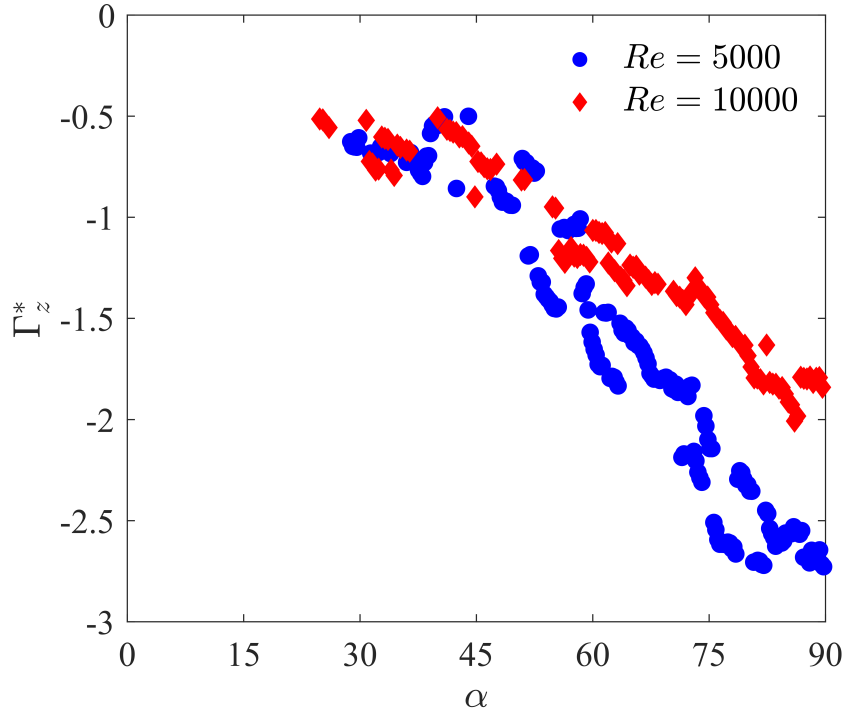
Figure 3.25: Comparison of LEV circulation for $Re = 5{,}000$ and $10{,}000$ at $x_p/c = 0$ and $K = 0.2$

The influence of Reynolds number on LEV growth is influenced by viscous and inviscid effects. Xu and Nitsche [73] predicted LEV growth with inviscid solutions [74, 75, 76], but later, the second-order dependence of viscosity on the development of LEVs [65] added additional complexity in terms of shear layer thickness, leading edge geometry, and characteristic length scales. In light of these complexities and conflicting arguments, the holistic understanding of the influence of the Reynolds number on LEV development is still not fully understood. The reduced vorticity growth at $Re = 10{,}000$ as compared to $Re = 5{,}000$ prompts exploration of plausible hypotheses to understand the underlying mechanisms such as:

1. Parameters influencing vortex growth on pitching airfoils in terms of varying leading-edge geometries, shear layer thickness and characteristic length scales have been invesitgated by various reserachers [77, 78, 79, 80, 65]. These studies signify the importance of the Reynolds number based on the leading shape or thickness ($Re = \frac{UL_{LE}}{\nu}$), which would impact the thickness of feeding shear layer. The thickness of the shear layer (δ_{SL}) near the leading edge of an airfoil, can be estimated using the Falkner–Skan solution
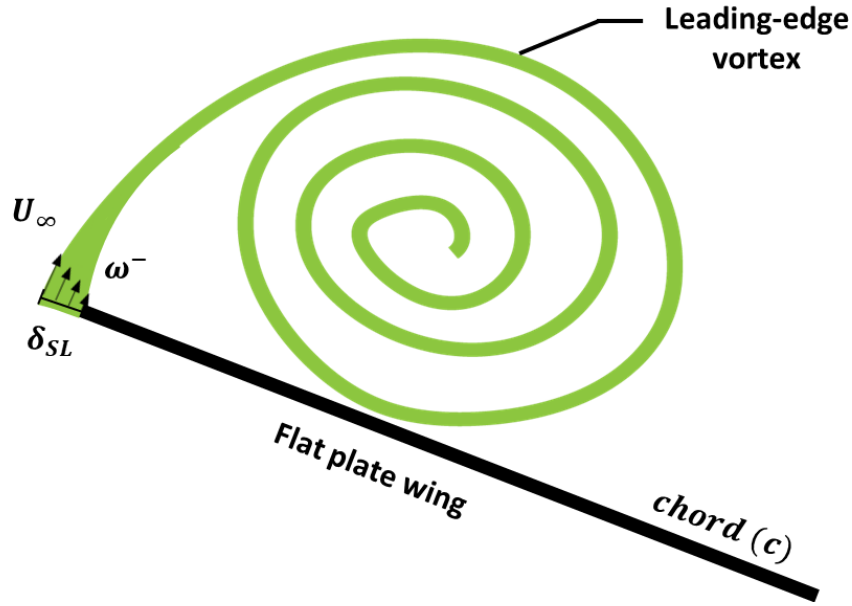
Figure 3.26: Schematic representation (not to scale) of mass flux from the shear layer into the LEV

[81] as $\delta_{SL} \approx \frac{2.4}{\sqrt{\nu/a}}$, where ν is the kinematic viscosity and a represents the local flow field near the stagnation point. Figure 3.26 shows the schematic representation of the mass flux from the shear layer into the LEV. Since $a \propto U_\infty^{-0.5}$, the shear layer thickness is inversely proportional to the square root of the Reynolds number (Re), expressed as $\delta_{SL} \propto Re^{-0.5}$. Furthermore, Kaden [76] gave the analytical expression for the mass flux into the LEV as $\dot{m} \approx \frac{1}{2}\rho U_\infty \delta_{SL}$. This means that the higher Reynolds number will have a lower non-dimensional vorticity growth rate inside the LEV because of lower mass flux associated with it. Reduced vorticity growth at higher Reynolds number can be directly associated with reduced LEV strength at $Re = 10,000$ as compared to $Re = 5,000$.

2. According to previous research [66], the main contributor to LEV growth is the vorticity in the shear layer, while the secondary vorticity in the boundary layer beneath the vortex slows its growth by vorticity annihilation. The vorticity transport equation in the rotating frame of reference of the wing as given by Buchholz et al. [66] can be written as:

$$\underbrace{\frac{d\mathbf{\Gamma}}{dt}}_{\text{Rate of change of circulation}} = \underbrace{-\int_A \mathbf{u}_z \frac{\partial \boldsymbol{\omega}_z}{\partial z} \, dA}_{\text{Spanwise convection of vorticity}} + \underbrace{\int_A (\boldsymbol{\omega}_x \frac{\partial \mathbf{u}_z}{\partial x} + \boldsymbol{\omega}_y \frac{\partial \mathbf{u}_z}{\partial y}) \, dA}_{\text{Local vorticity tilting}}$$

$$\underbrace{-\oint_{\delta A} (\mathbf{u} \cdot \mathbf{n}_{\delta A}) \boldsymbol{\omega}_z \, ds}_{\text{In-plane convective flux of vorticity}} \underbrace{-\nu \int_{\text{boundary 4}} \frac{\partial \boldsymbol{\omega}_z}{\partial y} \, dx}_{\text{Diffusive flux of vorticity}} \quad (3.19)$$

$$\underbrace{+ \iint_A (2\mathbf{\Omega_x} \frac{\partial \mathbf{u}_z}{\partial x} + 2\mathbf{\Omega_y} \frac{\partial \mathbf{u}_z}{\partial y}) \, dA}_{\text{Contributions due to the rotational accelerations}}$$

Analysis of this equation reveals that the fourth term on the right hand side of this equation i.e $\nu \int_{\text{boundary 4}} \frac{\partial \boldsymbol{\omega}_z}{\partial y} \, dx$ is responsible for slowing the vorticity growth by vorticity diffusion. If we non-dimensionalize the vorticity transport equation, then $\nu \int_{\text{boundary 4}} \frac{\partial \boldsymbol{\omega}_z}{\partial y} \, dx$ term scales with $\frac{1}{Re}$, which means that a higher Reynolds number will lead to a lower production of secondary vorticity. Therefore, the vorticity in the LEV is expected to be more pronounced in the case of higher Reynolds numbers. This phenomenon is also seen in the vorticity plots presented in figure 3.24, where positive sign vorticity is observed near the plate surface at higher pitch angles for $Re = 5,000$, whereas it is absent for $Re = 10,000$. This means that vorticity diffusion is not responsible for the lower vorticity growth at a higher Reynolds number.

3. Previous studies [82, 77, 63, 78, 83, 29] have identified two vortex detachment mechanisms by which LEV growth can be terminated on a pitching flat plate. The first mechanism involves flow reversal at the trailing edge, which is similar to bluff body detachment. If the LEV grows sufficiently, it forms a full saddle in the wake, causing flow reversal at the trailing edge. This entrains opposite-signed vorticity beneath the LEV and inhibits its growth through the attached shear layer. The second mechanism to inhibit LEV growth involves the viscous/inviscid interaction of the primary LEV with the boundary layer. This mechanism leads to the separation of the boundary layer as a response to the pressure gradient applied by the LEV. This viscous/inviscid interaction highlights the role of secondary vortical structures, and a lower Reynolds number is normally suggested

to enhance the influence of this mechanism on the detachment process. The literature lacks a precise Reynolds number threshold for the transition between these two LEV detachment mechanisms. In our current investigation, varying the Reynolds number from 5,000 to 10,000 could signify a transition between these LEV detachment mechanisms, which would also affect the LEV growth rate. This potential shift could be a key factor contributing to the lower vorticity growth at the higher Reynolds number.

As the scope of the current investigation does not specifically investigate the mechanisms responsible for the reduced vorticity growth at higher Reynolds numbers. The proposed hypotheses serve as plausible explanations, emphasizing the need for further investigation and analysis to pinpoint the exact cause of this decrease in vorticity growth at higher Reynolds numbers.

Chapter 4

Conclusions

Based on the results from this study and the data available in the literature, it is evident that the scope of previous investigations was limited to isolated analyses in terms of the effects of K, x_p/c or Re on the aerodynamic loads and flow field. Consequently, there was a lack of a comprehensive understanding of the interrelated effects of these parameters. This study has shed light on this crucial aspect, revealing a significant gap in understanding the comprehensive impact of these parameters on the aerodynamic loads and flow field. The findings of this research can have potential implications in various engineering applications, such as MAV design, helicopter rotor blades, and turbines. It can significantly improve design methodologies, making aerodynamic systems more efficient and responsive in different real-world situations. The main conclusions drawn from this investigation are as follows:

Effect of reduced pitch rate and pivot location

1. The present investigation demonstrates that the increase in aerodynamic loads with increasing K is also intricately related to the pitch pivot location x_p/c. The increase in aerodynamic loads with increasing K is maximum at $x_p/c = 0$. The relative magnitude begins to decrease for aft pivot locations and completely diminishes for the trailing edge pivot location, at which the aerodynamic loads become insensitive to increasing K values.

2. Changing x_p/c for a range of K values from 0.02 to 0.2 revealed that there is a decrease in aerodynamic loads as the pitch pivot location moved from $x_p/c = 0$ to 1, but the relative decrease for different pivot locations depends on the magnitude of K. For the

lowest reduced pitch rate ($K = 0.02$) considered in this study, the effect of changing x_p/c is insignificant, but the unsteady effects become increasingly dominant with pitch rate increase.

3. Analysis of the relative magnitude of pitching and rotation speeds highlights a clear demarcation within the experimental test matrix considered in this study. Specifically, when $K < 0.05$, the pitching speed lags behind the rotation speed, whereas for $K \geq 0.05$, the pitching speed becomes equal to or greater than the rotation speed. Based on the range of K tested in this study, this distinction prompts the establishment of a cut off threshold at $K = 0.05$, signifying a transition between two separate regimes of aerodynamic loads as follows:

   (a) **Low reduced pitch rate regime ($K < 0.05$).** This regime is primarily characterized by a delay in the pitch angle of stall and exhibits insignificant variations across various x_p/c.

   (b) **High reduced pitch rate regime ($K \geq 0.05$).** In this regime, the unsteady effects become increasingly dominant as K increases and are most pronounced at $x_p/c = 0$ and eventually become nonexistent at $x_p/c = 1$.

4. Consistent with the previous studies, we observed that a higher K or aft x_p/c delays the pitch angle for LEV formation. However, this investigation delves deeper by quantifying LEV circulation across various scenarios. Comparison of the vortex circulation across different cases showed that the LEV circulation increases by increasing K or moving x_p/c towards the leading edge.

Scaling analysis of aerodynamic loads

5. From the control volume analysis for changing x_p/c it was observed that the unsteady aerodynamic loads are due to the pitch induced camber effect which in turn depends on the magnitude of trailing edge velocity u_{TE}. Non-dimensionalizing the lift and drag forces by adding u_{TE} to U_∞ collapses the C_L and C_D data across all the K and x_p/c

cases. Although the underlying physics of this phenomenon remains unclear, the proposed scaling analysis remains a unique and significant contribution of this research. It has the potential to allow us to isolate the root cause of unsteady aerodynamic loads solely on the basis of the trailing edge velocity, provided that we achieve a comprehensive understanding of its flow physics.

6. Consistent with the previous research, changing x_p/c at a constant K introduces a delay in the evolution of the force with respect to t^* for aft x_p/c. However, the present investigation offers additional information on the physical mechanisms that the delay in aerodynamic loads for aft x_p/c is due to the induced flow at the leading edge that decreases the effective angle of attack of the flat plate. If we non-dimensionalize time with respect to the effective convective time t_{eff}, we are able to collapse the time evolution of force histories for varying x_p/c at a constant K.

Effect of Reynolds number

7. Current investigation revealed that changing Reynolds number from $Re = 5,000$ to 10,000 results in a lower C_L and C_D. These results contradict previous studies, which showed that aerodynamic loads and flow characteristics are either insensitive to changes in Reynolds number or cause an increase in aerodynamic loads. Flow field analysis revealed that $Re = 10,000$ was associated with a lower vorticity growth rate compared to $Re = 5,000$. Lower vorticity growth and subsequently lower circulation of LEV at $Re = 10,000$ can be attributed to reduced suction pressure and, subsequently, lower aerodynamic loads at $Re = 10,000$. The exact cause of lower vorticity growth at higher Re is unknown and requires further investigation and analysis.

Chapter 5

Future work

1. The current study revealed that changing K, x_p/c or Re leads to significant variations in the dynamics of LEV including shear layer formation, peak vorticity buildup in LEV and eventual shedding from the attached shear layer. Future investigations can be conducted to explore the physical mechanisms driving LEV growth and exploring the correlation of K and x_p/c with LEV peak circulation and separation. Additionally, a study focusing on predicting flow separation at the leading edge and LEV formation may offer better control over the flow field dynamics while optimizing MAV performance.

2. Current experiments employed a wing with aspect ratio 6 and Rossby number 7.2, which differs from the lower aspect ratios and smaller Rossby numbers typical in actual insect wings. Previous research indicates that lower Rossby numbers induce significant three-dimensional variations in the LEV dynamics for rotating wings. To address this, future research is suggested to explore the aerodynamic effects of varying the Rossby number, ranging from infinity (translating wings) to very low values around 2.5, where pronounced three-dimensional effects are observed. This approach will enable us to compare the effect of Rossby number on aerodynamic loads and flow characteristics across different regimes of pitching wings.

3. The current investigation used a rectangular flat plate for experimentation, but it is known that actual insect wings vary widely in geometry and shapes along with differences in strength and surface texture. Examples include membranous wings in dragonflies, leathery elytra in beetles, halters in flies for balance, and sawtooth-patterned wings in some wasps. Recognizing this diversity, future studies can be done to explore different wing

geometries, shapes, and textures to better understand the effects on aerodynamic loads and vortex dynamics in pitching wings.

4. In the study of insect wing dynamics, researchers have found that the flapping motion involves both upstroke and downstroke cycles, leading to changes in aerodynamic loads. While most studies focus on fixed-pivot cases, recent research on mosquitoes revealed a movable pivot mechanism. The mosquito's wings shift the pivot location from LE to TE during the transition from upstroke to downstroke, thus ensuring positive lift during most of pitching cycle. This concept of movable pivot combined with the dynamics of the flapping wing can be investigated in future research to optimize the lift performance of MAVs.

References

[1] Richard J Bomphrey, Nicholas J Lawson, Graham K Taylor, and Adrian L R Thomas. Application of digital particle image velocimetry to insect aerodynamics: measurement of the leading-edge vortex and near wake of a Hawkmoth. *Experiments in Fluids*, 40:546–554, 2006.

[2] Charles Porter Ellington. The aerodynamics of hovering insect flight. IV. Aerodynamic mechanisms. *Philosophical Transactions of the Royal Society of London. B, Biological Sciences*, 305(1122):79–113, 1984.

[3] J M Zanker and K G Götz. The wing beat of Drosophila melanogaster. II. Dynamics. *Philosophical Transactions of the Royal Society of London. B, Biological Sciences*, 327(1238):19–44, 1990.

[4] Adrian L R Thomas, Graham K Taylor, Robert B Srygley, Robert L Nudds, and Richard J Bomphrey. Dragonfly flight: free-flight and tethered flow visualizations reveal a diverse array of unsteady lift-generating mechanisms, controlled primarily via angle of attack. *Journal of Experimental Biology*, 207(24):4299–4323, 2004.

[5] Alexander P Willmott and Charles P Ellington. The mechanics of flight in the hawkmoth Manduca sexta. II. Aerodynamic consequences of kinematic and morphological variation. *The Journal of experimental biology*, 200(21):2723–2745, 1997.

[6] Hao Liu, Sridhar Ravi, Dmitry Kolomenskiy, and Hiroto Tanaka. Biomechanics and biomimetics in insect-inspired flight systems. *Philosophical Transactions of the Royal Society B: Biological Sciences*, 371(1704):20150390, 2016.

[7] Kirill V Rozhdestvensky and Vladimir A Ryzhov. Aerohydrodynamics of flapping-wing propulsors. *Progress in Aerospace Sciences*, 39(8):585–633, 2003.

[8] S A Ansari, R Żbikowski, and Kevin Knowles. Aerodynamic modelling of insect-like flapping flight for micro air vehicles. *Progress in Aerospace Sciences*, 42(2):129–172, 2006.

[9] Steven Ho, Hany Nassef, Nick Pornsinsirirak, Yu-Chong Tai, and Chih-Ming Ho. Unsteady aerodynamics and flow control for flapping wing flyers. *Progress in Aerospace Sciences*, 39(8):635–681, 2003.

[10] Wei Shyy, Mats Berg, and Daniel Ljungqvist. Flapping and flexible wings for biological and micro air vehicles. *Progress in Aerospace Sciences*, 35(5):455–505, 1999.

[11] Wei Shyy, Yongsheng Lian, Jian Tang, Dragos Viieru, and Hao Liu. *Aerodynamics of low Reynolds number flyers*. 2008.

[12] Dae-Kwan Kim and Jae-Hung Han. Smart flapping wing using macrofiber composite actuators. In *Smart structures and materials 2006: smart structures and integrated systems*, volume 6173, pages 133–141. SPIE, 2006.

[13] Thomas J Mueller. *Fixed and flapping wing aerodynamics for micro air vehicle applications*. AIAA, 2001.

[14] Max F Platzer, Kevin D Jones, John Young, and Joseph C S Lai. Flapping wing aerodynamics: progress and challenges. *AIAA Journal*, 46(9):2136–2149, 2008.

[15] Sanjay P Sane. The aerodynamics of insect flight. *Journal of experimental biology*, 206(23):4191–4208, 2003.

[16] Fritz-Olaf Lehmann and Michael H Dickinson. The control of wing kinematics and flight forces in fruit flies (Drosophila spp.). *The Journal of experimental biology*, 201(3):385–401, 1998.

[17] Wei Shyy, Hikaru Aono, Satish Kumar Chimakurthi, Pat Trizila, C-K Kang, Carlos E S Cesnik, and Hao Liu. Recent progress in flapping wing aerodynamics and aeroelasticity. *Progress in Aerospace Sciences*, 46(7):284–327, 2010.

[18] Charles P Ellington. The novel aerodynamics of insect flight: applications to micro-air vehicles. *Journal of experimental biology*, 202(23):3439–3448, 1999.

[19] Charles P Ellington, Coen Van Den Berg, Alexander P Willmott, and Adrian L R Thomas. Leading-edge vortices in insect flight. *Nature*, 384(6610):626–630, 1996.

[20] Zhi Ern Teoh and Robert J Wood. A flapping-wing microrobot with a differential angle-of-attack mechanism. In *2013 IEEE International Conference on Robotics and Automation*, pages 1381–1388. IEEE, 2013.

[21] William J McCroskey. Unsteady airfoils. *Annual review of fluid mechanics*, 14(1):285–311, 1982.

[22] John A Ekaterinaris and Max F Platzer. Computational prediction of airfoil dynamic stall. *Progress in Aerospace Sciences*, 33(11-12):759–846, 1998.

[23] Huai-Te Yu and Luis P Bernal. Effects of pivot location and reduced pitch rate on pitching rectangular flat plates. *AIAA Journal*, 55(3):702–718, 2017.

[24] Kenneth O Granlund, Michael V Ol, and Luis P Bernal. Unsteady pitching flat plates. *Journal of Fluid Mechanics*, 733:R5, 2013.

[25] Yuelong Yu, Xavier Amandolese, Chengwei Fan, and Yingzheng Liu. Experimental study and modelling of unsteady aerodynamic forces and moment on flat plate in high amplitude pitch ramp motion. *Journal of Fluid Mechanics*, 846:82–120, 2018.

[26] Miguel R Visbal and J S Shang. Investigation of the flow structure around a rapidly pitching airfoil. *AIAA Journal*, 27(8):1044–1051, 1989.

[27] Pradeep Kumar Seshadri, Akhil Aravind, and Ashoke De. Leading edge vortex dynamics in airfoils: Effect of pitching motion at large amplitudes. *Journal of Fluids and Structures*, 116:103796, 2023.

[28] Xiao Li, Li-Hao Feng, and Zhen-Yao Li. Flow mechanism for the effect of pivot point on the aerodynamic characteristics of a pitching airfoil and its manipulation. *Physics of Fluids*, 31(8):87108, 2019.

[29] Alexander Widmann and Cameron Tropea. Reynolds number influence on the formation of vortical structures on a pitching flat plate. *Interface focus*, 7(1):20160079, 2017.

[30] Kiran Ramesh, Kenneth Granlund, Michael V Ol, Ashok Gopalarathnam, and Jack R Edwards. Leading-edge flow criticality as a governing factor in leading-edge vortex initiation in unsteady airfoil flows. *Theoretical and Computational Fluid Dynamics*, 32:109–136, 2018.

[31] Jeff Eldredge, Chengjie Wang, and Michael Ol. A computational study of a canonical pitch-up, pitch-down wing maneuver. In *39th AIAA fluid dynamics conference*, page 3687, 2009.

[32] Michael Ol, Aaron Altman, Jeff Eldredge, Daniel Garmann, and Yongsheng Lian. Resume of the AIAA FDTC low Reynolds number discussion group's canonical cases. In *48th AIAA Aerospace Sciences Meeting Including the New Horizons Forum and Aerospace Exposition*, page 1085, 2010.

[33] Kyle Hord and Yongsheng Lian. Numerical Study of Finite Aspect Ratio Perching Wings. In *50th AIAA Aerospace Sciences Meeting including the New Horizons Forum and Aerospace Exposition*, page 1081, 2012.

[34] Daniel J Garmann and Miguel R Visbal. Numerical investigation of transitional flow over a rapidly pitching plate. *Physics of Fluids*, 23(9):94106, 2011.

[35] Miguel Visbal. Flow structure and unsteady loading over a pitching and perching low-aspect-ratio wing. In *42nd AIAA Fluid Dynamics Conference and Exhibit*, page 3279, 2012.

[36] Ryan T Jantzen, Kunihiko Taira, Kenneth O Granlund, and Michael V Ol. Vortex dynamics around pitching plates. *Physics of Fluids*, 26(5), 2014.

[37] Z Charlie Zheng, Ning Zhang, and Z Wei. Low Reynolds Number Simulation for Flow Over a Flapping Wing: Comparisons to Measurement Data. In *39th AIAA Fluid Dynamics Conference*, page 3691, 2009.

[38] Michael V Ol, Jeff D Eldredge, and Chengjie Wang. High-amplitude pitch of a flat plate: an abstraction of perching and flapping. *International Journal of Micro Air Vehicles*, 1(3):203–216, 2009.

[39] M Ol. High-frequency, high-amplitude pitch problem: airfoils, plates, and wings. In *39th AIAA Fluid Dynamics Conference*, page 3686, 2009.

[40] Michael H Dickinson, Fritz-Olaf Lehmann, and Sanjay P Sane. Wing rotation and the aerodynamic basis of insect flight. *Science*, 284(5422):1954–1960, 1999.

[41] J J Videler, E J Stamhuis, and G D E Povel. Leading-edge vortex lifts swifts. *Science*, 306(5703):1960–1962, 2004.

[42] Gregory Reich, Olek Wojnar, and Roberto Albertani. Aerodynamic performance of a notional perching MAV design. In *47th AIAA Aerospace Sciences Meeting including The New Horizons Forum and Aerospace Exposition*, page 63, 2009.

[43] MUSTAFA Percin and B W Van Oudheusden. Three-dimensional flow structures and unsteady forces on pitching and surging revolving flat plates. *Experiments in Fluids*, 56(2):1–19, 2015.

[44] C A Ozen and Donald Rockwell. Flow structure on a rotating plate. *Experiments in Fluids*, 52(1):207–223, 2012.

[45] M Bross and D Rockwell. Three-dimensional flow structure along simultaneously pitching and rotating wings: Effect of pitch rate. *Experiments in Fluids*, 56(4):1–14, 2015.

[46] Field Manar, Peter Mancini, David Mayo, and Anya R Jones. Comparison of rotating and translating wings: force production and vortex characteristics. *AIAA Journal*, 54(2):519–530, 2016.

[47] Sanjay P Sane and Michael H Dickinson. The aerodynamic effects of wing rotation and a revised quasi-steady model of flapping flight. *Journal of experimental biology*, 205(8):1087–1096, 2002.

[48] Abbishek Gururaj, Mahyar Moaven, Zu Puayen Tan, Brian Thurow, and Vrishank Raghav. Rotating three-dimensional velocimetry. *Experiments in Fluids*, 62(7):146, 2021.

[49] Field Manar, Albert Medina, and Anya R Jones. Tip vortex structure and aerodynamic loading on rotating wings in confined spaces. *Experiments in fluids*, 55:1–18, 2014.

[50] Manoochehr M Koochesfahani and Vanco Smiljanovski. Initial acceleration effects on flow evolution around airfoils pitching to high angles of attack. *AIAA journal*, 31(8):1529–1531, 1993.

[51] C P Gendrich, M M Koochesfahani, and M R Visbal. Effects of initial acceleration on the flow field development around rapidly pitching airfoils. *Journal of Fluids Engineering*, 1995.

[52] Markus Raffel, Christian E Willert, Fulvio Scarano, Christian J Kähler, Steve T Wereley, and Jürgen Kompenhans. *Particle image velocimetry: a practical guide*. Springer, 2018.

[53] Laurent Graftieaux, Marc Michard, and Nathalie Grosjean. Combining PIV, POD and vortex identification algorithms for the study of unsteady turbulent swirling flows. *Measurement Science and technology*, 12(9):1422, 2001.

[54] H Glauert. The Elements of Airfoil and Airscrew Theory, 1959. *Cambridge Univ*, page 93.

[55] John Anderson. *EBOOK: Fundamentals of Aerodynamics (SI units)*. McGraw hill, 2011.

[56] J H Strickland and G M Graham. Force coefficients for a NACA-0015 airfoil undergoing constant pitchrate motions. *AIAA Journal*, 25(4):622–624, 1987.

[57] J M Walker, H E Helin, and J H Strickland. An experimental investigation of an airfoil undergoing large-amplitude pitching motions. *AIAA Journal*, 23(8):1141–1142, 1985.

[58] Abel-John Buchner, Nicolas Buchmann, Kareem Kilany, Callum Atkinson, and Julio Soria. Stereoscopic and tomographic PIV of a pitching plate. *Experiments in fluids*, 52:299–314, 2012.

[59] E J Jumper, S J Schreck, and R L Dimmick. Lift-curve characteristics for an airfoil pitching at constant rate. *Journal of aircraft*, 24(10):680–687, 1987.

[60] Scott J Schreck, William E Faller, and Michael C Robinson. Unsteady separation processes and leading edge vortex precursors: pitch rate and Reynolds number influences. *Journal of aircraft*, 39(5):868–875, 2002.

[61] Mukund Acharya and Metwally H Metwally. Unsteady pressure field and vorticity production over a pitching airfoil. *AIAA journal*, 30(2):403–411, 1992.

[62] P Ghosh Choudhuri, D D Knight, and M R Visbal. Two-dimensional unsteady leading-edge separation on a pitching airfoil. *AIAA journal*, 32(4):673–681, 1994.

[63] T L Doligalski, C R Smith, and J D A Walker. Vortex interactions with walls. *Annual Review of Fluid Mechanics*, 26(1):573–616, 1994.

[64] Edward Charles Polhamus. A concept of the vortex lift of sharp-edge delta wings based on a leading-edge-suction analogy. Technical report, 1966.

[65] Jeff D Eldredge and Anya R Jones. Leading-edge vortices: mechanics and modeling. *Annual Review of Fluid Mechanics*, 51:75–104, 2019.

[66] Craig J Wojcik and James H J Buchholz. Vorticity transport in the leading-edge vortex on a rotating blade. *Journal of Fluid Mechanics*, 743:249–261, 2014.

[67] Gordon J Leishman. *Principles of helicopter aerodynamics with CD extra*. Cambridge university press, 2006.

[68] Holger Babinsky, Robbie J Stevens, Anya R Jones, Luis P Bernal, and Michael V Ol. Low order modelling of lift forces for unsteady pitching and surging wings. In *54th AIAA aerospace sciences meeting*, page 290, 2016.

[69] Yuan Cheng Fung. *An introduction to the theory of aeroelasticity*. Courier Dover Publications, 2008.

[70] W Sheng, R A McD Galbraith, and F N Coton. A new stall-onset criterion for low speed dynamic-stall. *Journal of Solar Energy Engineering*, 128(4):461–471, 2006.

[71] H Helin and J Walker. Interrelated effects of pitch rate and pivot point on airfoil dynamic stall. In *23rd Aerospace Sciences Meeting*, page 130, 1985.

[72] Carolyn M Reed, David A Coleman, and Moble Benedict. Force and flowfield measurements to understand unsteady aerodynamics of cycloidal rotors in hover at ultra-low Reynolds numbers. *International Journal of Micro Air Vehicles*, 11:1756829319833677, 2019.

[73] Ling Xu and Monika Nitsche. Scaling behaviour in impulsively started viscous flow past a finite flat plate. *Journal of fluid mechanics*, 756:689–715, 2014.

[74] D I Pullin. The large-scale structure of unsteady self-similar rolled-up vortex sheets. *Journal of Fluid Mechanics*, 88(3):401–430, 1978.

[75] D I Pullin and Z Jane Wang. Unsteady forces on an accelerating plate and application to hovering insect flight. *Journal of Fluid Mechanics*, 509:1–21, 2004.

[76] Heinrich Kaden. Aufwicklung einer unstabilen Unstetigkeitsfläche. *Ingenieur-Archiv*, 2(2):140–168, 1931.

[77] David E Rival, Jochen Kriegseis, Pascal Schaub, Alexander Widmann, and Cameron Tropea. Characteristic length scales for vortex detachment on plunging profiles with varying leading-edge geometry. *Experiments in fluids*, 55:1–8, 2014.

[78] A Widmann and C Tropea. Parameters influencing vortex growth and detachment on unsteady aerodynamic profiles. *Journal of Fluid Mechanics*, 773:432–459, 2015.

[79] R R Leknys, M Arjomandi, R M Kelso, and C H Birzer. Leading-edge vortex development on a pitching flat plate with multiple leading edge geometries. *Experimental Thermal and Fluid Science*, 96:406–418, 2018.

[80] David Rival, Tim Prangemeier, and Cameron Tropea. The influence of airfoil kinematics on the formation of leading-edge vortices in bio-inspired flight. *Animal Locomotion*, pages 261–271, 2010.

[81] Hermann Schlichting and Klaus Gersten. *Boundary-layer theory*. springer, 2016.

[82] David Rival, Tim Prangemeier, and Cameron Tropea. The influence of airfoil kinematics on the formation of leading-edge vortices in bio-inspired flight. *Animal Locomotion*, pages 261–271, 2010.

[83] J H Gerrard. The mechanics of the formation region of vortices behind bluff bodies. *Journal of fluid mechanics*, 25(2):401–413, 1966.

Appendix A

Pitching speed calibration of servo motor

In this study, a custom LabVIEW code was employed to program the motion profile of a servo motor controlling the pitch of a plate. The pitching speed of the servo motor was systematically varied across a range from 0.5 rad/s to 6 rad/s. To assess the accuracy and effectiveness of the servo motor's response, a high-speed Phantom VEO 4K 990L camera with a rapid acquisition rate of 900 Hz was utilized to capture the complete motion profile. The acquired images were subsequently processed using ImageJ software to measure the pitch angle at various instances of time. This approach enabled a comprehensive comparison between the commanded motion profile generated by the LabVIEW program and the actual motion profile captured through high-speed image acquisition. The synthesis of LabVIEW programming, high-speed imaging, and precise angle measurements provided valuable insights into the servo motor's kinematic performance in response to varying commanded speeds.

In the study of unsteady aerodynamics during airfoil pitch ramp motion, practical limitations in experiments arise from finite acceleration and deceleration imposed by the driving system. Previous research [50, 24, 51] has shown that smoothing out pitch ramp motion minimally affects the dynamics of unsteady stall processes. Aerodynamic loads briefly depend on initial acceleration but subsequently depend primarily on the pitch angle for a given pitch rate. This finding allowed the selection of convenient acceleration profiles in our experiments without significantly impacting unsteady stall dynamics. The present study utilized the hyperbolic-cosine function [32, 24] to match the acceleration profile of pitching servo motion across different pitch rates. The motion profile is given as:

$$\alpha(t) = \frac{2\alpha_{\max}(1-\sigma)}{\pi^2} \ln \left[\frac{\cosh\left(\frac{\pi^2 K}{4\alpha_{\max}(1-\sigma)}\left(t^* - t_1^*\right)\right)}{\cosh\left(\frac{\pi^2 K}{4\alpha_{\max}(1-\sigma)}\left(t^* - t_1^* - \frac{\alpha_{\max}}{K}\right)\right)} \right] + \frac{\alpha_{\max}}{2} \tag{A.1}$$

This function is based on various parameters such as the maximum pitch angle (α_{max}), non-dimensional time (t^*), the starting point of the sharp ramp corner (t_1^*), the ideal constant-pitch-rate period (α_{max}/K), and a smoothing parameter (σ). The servo motor had a operating voltage range of $8.4 - 12.6\ volts$ and was capable of no load pitching speeds of $13\ rad/s$ and the maximum torque range was $3.24 - 4.9\ Nm$. Based on these parameters, calibration of the acceleration and pitch speed of the servo motor was carried out by varying the smoothing parameter σ to match the measured profile. A comparison of measured pitch ramp motion with the revised hyperbolic-cosine function for various pitch rates $\dot{\alpha}$ ranging from 0.5 rad/s till 6 rad/s, $\alpha_{max} = 90°$ has been shown in figure A.1.

The sigma (σ) values corresponding to different $\dot{\alpha}$ cases were plotted, and a polynomial curve was fitted through the data points. The resulting equation was uses as a calibration equation to calibrate the motion profile of a servo motor across various K cases. This process ensured accurate profile to the servo motor's motion based on the specific values of K. Same has been shown in figure A.2.
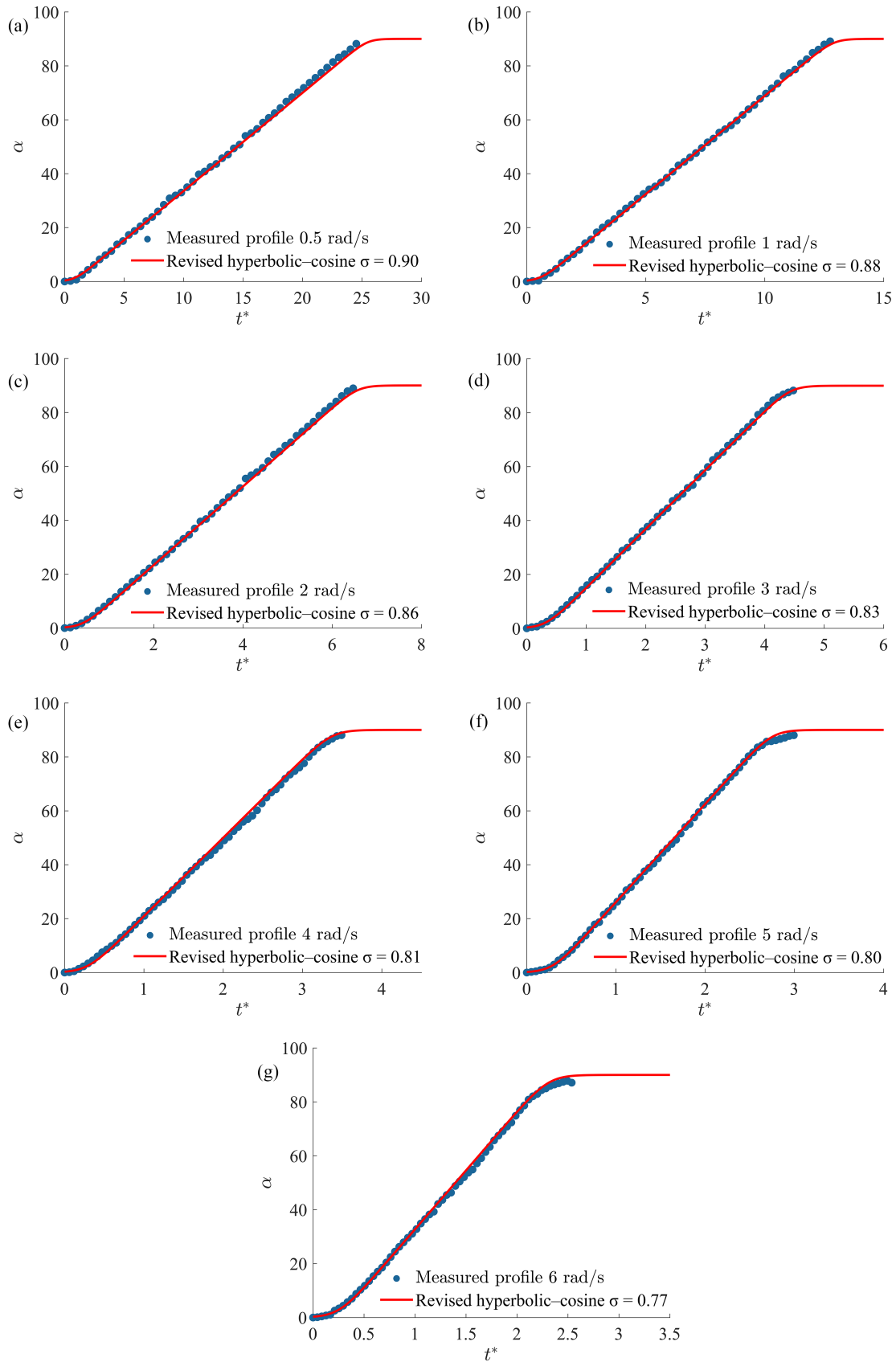
Figure A.1: Comparison of revised hyperbolic cosine function with pitching profile of servo motor at 0.5 rad/s (a), 1 rad/s (b), 2 rad/s (c), 3 rad/s (d), 4 rad/s (e), 5 rad/s (f), 6 rad/s (g)
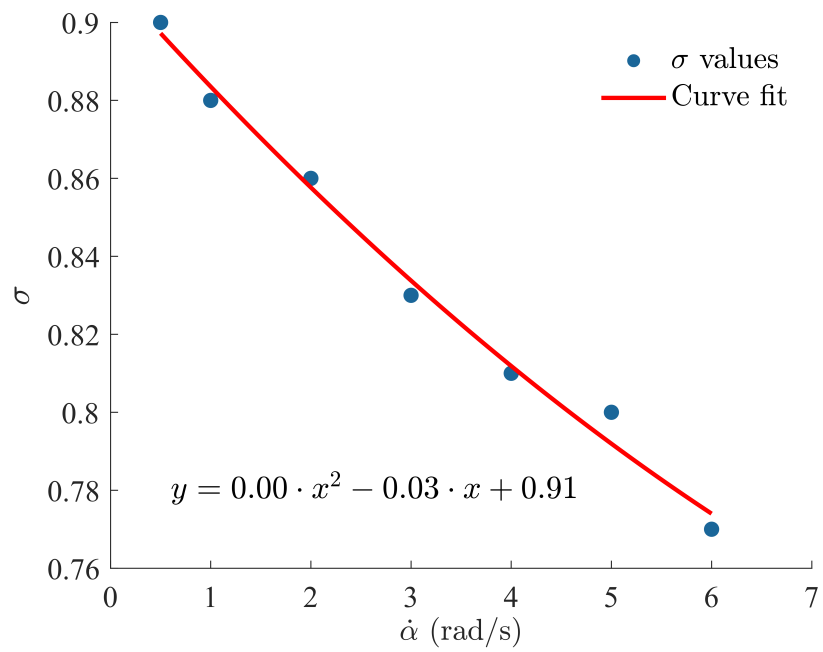
Figure A.2: Pitch profile calibration of servo motor